C

CHARACTERISTIC EARTHQUAKES AND SEISMIC GAPS

David D. Jackson, Yan Y. Kagan
Department of Earth and Space Sciences, University of California Los Angeles, Los Angeles, CA, USA

Definitions

Fault slip. Relative motion, either steady or sudden as in earthquakes, between rock units on either side of a fault.
Rupture. Sudden fault slip in an earthquake.
Elastic rebound. Sudden release, as by an earthquake, of slowly accumulated strain energy.
Segment. A section of a fault or plate interface bounded by features thought to serve as strong barriers to earthquake rupture. Features postulated to form such barriers include changes in fault orientation or in rock type across parts of the fault, and intersections with other faults.
Characteristic earthquake. An earthquake rupturing an entire fault segment. Alternately, one of a sequence of earthquakes rupturing the same area of fault.
Recurrence interval. The time between characteristic earthquakes on a given segment or fault area.
Quasiperiodic. Occurring at approximately equal recurrence intervals.
Seismic cycle. A sequence of events on a segment starting with a large earthquake, followed by aftershocks, then by steady stress accumulation, and culminating with another large earthquake. The term "cycle" is sometimes but not always meant to imply quasiperiodic recurrence.
Seismic gap. A segment for which the time since the previous characteristic earthquake approaches or exceeds the average recurrence interval.

Introduction

The seismic gap hypothesis holds that most long-term geologic slip on faults or plate boundaries is accomplished by characteristic earthquakes on segments. Such quakes are presumed to reduce the stress substantially, necessitating a substantial recurrence time for elastic stress to recover before the next characteristic earthquake. The dates and rupture extent of past earthquakes may be determined by modern seismic networks; by historic reports of faulting, damage, or strong shaking; or by paleoseismic investigation of trenches across faults. The average recurrence time may be determined either from a sequence of dates of past characteristic earthquakes, or by the time required for steady slip on a fault to accumulate the slip experienced in a characteristic earthquake (Working Group on California Earthquake Probabilities, 1988, 1990).

History

Well before plate tectonics became accepted in the 1960s, Gilbert (1884) argued that large earthquakes should be separated by substantial time intervals. Reid (1910, 1911) proposed that faults slowly accumulate energy later released suddenly by earthquakes ("elastic rebound"), and that the time to a future earthquake could be estimated by surveying the strain released by a previous one. Fedotov (1965) noticed that most of the Kamchataka–Kurile trench in the northwest Pacific had been ruptured by earthquakes in the early twentieth century, with the exception of one zone southeast of Hokkaido. He concluded that a future earthquake was likely in that area, a forecast realized in 1973 when the Nemuro-oki earthquake struck with magnitude about 7.5 (Kasahara, 1981, 182).

Plate tectonics now provides a compelling, steady source of the strain energy driving elastic rebound, and

Harsh K. Gupta (ed.), *Encyclopedia of Solid Earth Geophysics*, DOI 10.1007/978-90-481-8702-7,

that fact led many to conclude that occurrence of large earthquakes must be separated by enough time to allow recharge. Scholz (1990, 260) remarked that "A tenet of plate tectonics is that the rates of plate motion must be steady over geologic time periods and must be continuous along plate boundaries. If it is assumed further that a significant portion of this motion must be released seismically, then it follows that segments of plate boundaries that have not ruptured for the longest time are those most likely to rupture in the near future. These places are called seismic gaps." The seismic gap hypothesis was celebrated when Nishenko, 1989 published a list of 13 earthquakes that fit, at least approximately, the descriptions of previously expected earthquakes.

The seismic gap model has been applied to long-term forecasting of earthquakes in many regions (Sykes, 1971; Kelleher, 1972; Kelleher et al., 1973; McCann et al., 1979; Working Group on California Earthquake Probabilities, 1988, Nishenko, 1991). The model and its definition have evolved along with the quality and quantity of data that go into it. Fedotov (1965) defined the Nemuro-oki gap as the last remaining unbroken segment. McCann et al. (1979) used elapsed time and a color code to label segments around the Pacific Rim: more than 100 years had elapsed in red gaps, between 30 and 100 years in orange gaps, and less than 30 years in apparently safe green zones. In the most comprehensive forecast ever using the seismic gap model, Nishenko (1991) actually made testable probabilistic forecasts for about 125 plate boundary segments around the Pacific Rim. In that study he estimated the mean recurrence time and the elapsed time for each segment, and assumed that their ratio obeys a log-normal probability density function. With that information, he calculated the probability that each zone would be ruptured by a characteristic earthquake whose magnitude he also listed for each zone within 5-, 10-, and 30-year periods. A very similar model was used by the Working Group on California Earthquake Probabilities (1988) in its official earthquake probability estimates.

Assumptions

All the applications mentioned above share several important assumptions. First, their authors assume that faults and plate boundaries are segmented and that rupture does not cross segment boundaries. Second, they assume that each characteristic earthquake ruptures to both ends of its segment, reducing the stress to a uniform base level and beginning the process of stress recharge. Third, they assume that the time to the next characteristic earthquake depends almost entirely on the time of the previous one: not on other earthquakes, nonelastic stress redistribution, or other causes. To make useful forecasts, scientists must obviously be able to distinguish characteristic earthquakes from all others in order to know the elapsed time since the last one.

Small characteristic earthquakes

Recent studies in California (e.g., Nadeau and McEvilly, 1999), Japan (e.g., Igarashi et al., 2003; Okada et al., 2003), and elsewhere have identified sequences of small earthquakes fitting the alternative definition of "characteristic earthquake" above. In each sequence, the events are approximately the same size, and rupture approximately the same fault area. They recur at nearly equal time intervals or in some cases variable intervals consistent with variations in their size or in fault slip rate. In most cases, the slipped areas appear to be surrounded by areas where displacement occurs by steady slip rather than earthquakes. Because of that special circumstance, these small repeating earthquakes are not relevant to the discussion of seismic gaps.

Modified seismic gap hypothesis

As time, earthquake experience, and theoretical sophistication have accumulated, earth scientists have modified the seismic gap theory to rely less on the assumptions above. The Working Group on California Earthquake Probabilities (1990) allowed adjustments to account for stresses from earthquakes not on the relevant segment. The 1992 Landers, California earthquake (magnitude about 7) presented a particularly important observation. In that event, rupture jumped segment boundaries and even faults, making use of up to five faults mapped as separate before 1992. In a seismic hazard model produced by the Southern California Earthquake Center (Working Group on California Earthquake Probabilities, 1995), the seismic gap model was modified to allow rupture to jump segment boundaries with a modest probability. Later uses of the seismic gap model in California for official hazard estimates employ increasingly complex assumptions, especially about conditions under which rupture is likely to involve more than one segment (Working Group on California Earthquake Probability, 2002, 2008).

The more complex versions of the model raise interesting questions. What truly constitutes a segment? How effective are weak barriers in stopping rupture, and what controls their strength? Are the boundaries fixed in space, or can they move as stress conditions change? When rupture crosses a boundary, does it consistently continue to the next? If not, does it reset the stress and the clock on the partially ruptured segment? Do the elapsed times on adjacent segments control the probability that rupture will jump the barrier between them? If so, which segment is most important? Modelers must answer these questions, implicitly or explicitly, to forecast using the modified gap models. So far, there is no clear consensus on the answers.

Challenges to the seismic gap model

Despite some reported successes, the seismic gap hypothesis has often been questioned. Critics point to the difficulty of verifying the rather strong assumptions behind the hypothesis, and to its limited success in forecasting earthquakes.

The basic assumption that faults and plate boundaries are segmented has provoked significant debate. Even the few apparent successes (e.g., Loma Prieta, CA, 1989;

Parkfield, CA 2004; Chile, 2010), are equivocal at best. The rupture of the Loma Prieta earthquake was about the length of the nearest segment mapped by the Working Group on California Earthquake Probabilities (1988), but it shifted south and spilled over the southern segment boundary. Moreover, the event occurred near, but not actually on the San Andreas Fault for which the segment was defined. Before 2004, the Parkfield segment was defined in several different ways, so its location at Parkfield does not confirm the segmentation hypothesis (Jackson and Kagan, 2006). The 2010 Chile earthquake went well beyond the segment boundaries specified by Nishenko (1991). In addition, several events have clearly violated preassigned boundaries. The 1992 Landers quake was mentioned above, and the great Sumatra tsunami earthquake of 2004 breached several boundaries along its 1,300-km rupture zone (Nalbant et al., 2005).

The assumption that earthquakes rupture to both ends of segment boundaries also lacks verification. A basic problem is that the locations of segment boundaries are usually estimated inaccurately from the extent of past earthquake ruptures. For earthquakes identified by paleoseismic investigations, rupture can generally be pinpointed at only a few widely spaced locations. For historical earthquakes, rupture extent is typically estimated with great uncertainty from the extent of damage or reported shaking. Even for modern instrumentally recorded earthquakes, the extent of the aftershock zone or fault scarp may not accurately represent the rupture at depth where the elastic rebound occurs. In many cases, the extent of rupture for older earthquakes is assumed to be similar to that of the most recent event, a clear case of circular reasoning.

The connection between plate tectonics and earthquake recurrence referred to in the words of Scholz above depends on the assumption that characteristic earthquakes release most of the slowly accumulated fault slip. However, that assumption fails in many examples. For instance, the cumulative slip of the Parkfield, CA earthquakes since 1857, often regarded as an archetypical characteristic sequence, accounts for only a small fraction of expected slip at the long-term geological rate (Jackson and Kagan, 2006). In such cases, the alternative definition of characteristic earthquakes listed above, and the times of past events, may provide valuable information on the causes of some earthquakes but the direct link to plate tectonics is lost.

Proponents of the seismic gap theory cite many examples in which identified gaps have been filled by earthquakes. The positive examples are appealing but insufficient for two reasons. First, the definitions of gaps and forecasted earthquakes were quite general, making the target easier to hit at random. Second, they included only successes; a fair evaluation needs to consider failures as well.

Kagan and Jackson (1991, 1995), and Rong et al. (2003) applied statistical tests to the seismic gap theory as articulated by McCann et al. (1979) and Nishenko (1991). Earthquakes were actually more frequent in McCann's green zones than in the red ones, opposite to what the gap theory assumes. The 1991 gap model implied far more earthquakes, in different places, than actually occurred. Kagan and Jackson (1995) and Rong et al. (2003) also tested a simple alternative to the gap model, assuming that earthquakes occur randomly in time and near past earthquakes. The alternative model fits the total number and the locations of future earthquakes much better than the 1991 gap model.

These statistical tests necessarily applied to the earlier versions of the gap hypothesis, in which segments were assumed to be independent of one another. Since then, more complex versions of the model have been applied. Most of these applications involve one or a few purported gaps with estimated recurrence times of decades or centuries. Published models generally do not provide probabilities for multi-segment ruptures, and they cannot be effectively evaluated until several seismic cycles have elapsed. To be rigorously testable, such a model must forecast a few tens of well-defined earthquakes. Unfortunately, no systematic, well-specified version of the more complex seismic gap model has been applied broadly enough to be tested.

Conclusions

The intuitively appealing seismic gap model encompasses the virtually unassailable principle that earthquakes release strain energy accumulated over a long time. Although many large events have occurred in previously identified gaps, the same is true of locations outside them. Simple versions of the gap theory, in which characteristic earthquakes occur on independent segments, are no longer tenable. Modified versions of the gap theory have not yet been formulated in a rigorously testable way.

Bibliography

Fedotov, S. A., 1965. Regularities of the distribution of strong earthquakes in Kamchatka, the Kurile Islands and northeastern Japan. *Tr Inst Fiz Zemli, Akad. Nauk SSSR*, **36**(203), 66–93 (in Russian).

Gilbert, G. K., 1884. A theory of the earthquakes of the Great Basin, with a practical application. *American Journal of Science*, **27**(157), 49–54. Ser. 3.

Igarashi, T., Matsuzawa, T., and Hasegawa, A., 2003. Repeating earthquakes and interplate aseismic slip in the northeastern Japan subduction zone. *Journal of Geophysical Research*, **108**(B5), 2249, doi:doi:10.1029/2002JB001920.

Jackson, D. D., and Kagan, Y. Y., 2006. The 2004 parkfield earthquake, the 1985 prediction, and characteristic earthquakes: lessons for the future. *Bulletin. Seismological Society of America*, **96**, S397–S409.

Kagan, Y. Y., and Jackson, D. D., 1991. Seismic gap hypothesis: Ten years after. *Journal of Geophysical Research*, **96**(21), 21419–21431.

Kagan, Y. Y., and Jackson, D. D., 1995. New seismic gap hypothesis: Five years after. *Journal of Geophysical Research*, **100**(B3), 3943–3959.

Kasahara, K., 1981. *Earthquake Mechanics*. Cambridge: Cambridge University Press.

Kelleher, J. A., 1972. Rupture zones of large South American earthquakes and some predictions. *Journal of Geophysical Research*, **77**, 2087–2103.

Kelleher, J. A., Sykes, L. R., and Oliver, J., 1973. Possible criteria for predicting earthquake locations and their applications to

major plate boundaries of the Pacific and Caribbean. *Journal of Geophysical Research*, **78**, 2547–2585.
McCann, W. R., Nishenko, S. P., Sykes, L. R., and Krause, J., 1979. Seismic gaps and plate tectonics: Seismic potential for major boundaries, *Pure and Applied Geophysics*, **117**, 1082–1147.
Nadeau, R. M., and McEvilly, T. V., 1999. Fault slip rates at depth from recurrence intervals of repeating microearthquakes. *Science*, **285**, 718–721.
Nalbant, S., Steacy, S., Sieh, K., Natawidjaja, D., and McCloskey, J., 2005. Seismology: Earthquake risk on the Sunda trench. *Nature*, **435**(7043), 756–757.
Nishenko, S. P., 1989. Earthquakes: hazards and predictions. In James, D. E. (ed.), *The Encyclopedia of Solid Earth Geophysics*. New York: Van Nostrand Reinhold, pp. 260–268.
Nishenko, S. P., 1991. Circum-Pacific seismic potential – 1989–1999. *Pure and Applied Geophysics*, **135**, 169–259.
Okada, T., Matsuzawa, T., and Hasegawa, A., 2003. Comparison of source areas of M4.8 ± 0.1 repeating earthquakes off Kamaishi, NE Japan: Are asperities persistent features? *Earth and Planetary Science Letters*, **213**, 361–374.
Reid, H. F., 1910. *The California Earthquake of April 18, 1906*. Washington: Carnegie Institution of Washington. The Mechanics of the Earthquake, Vol. 2.
Reid, H. F., 1911. The elastic-rebound theory of earthquakes, *University of California Department of Geology Bulletin*, **6**, 413–444.
Rong, Y.-F., Jackson, D. D., and Kagan, Y.Y., 2003. Seismic gaps and earthquakes, Journal of Geophysical Research, 108(B10), 2471, ESE-6, 1–14.
Scholz, C., 1990. *The Mechanics of Earthquakes and Faulting*. Cambridge: Cambridge U. Press.
Sykes, L. R., 1971. Aftershock zones of great earthquakes, seismicity gaps, and earthquake prediction for Alaska and the Aleutians. *Journal of Geophysical Research*, **76**, 8021–8041.
Working Group on California Earthquake Probabilities, 1988. Probabilities of large earthquakes occurring in California, on the San Andreas Fault. U.S. Geol. Surv., Open File Rep., 88–398, 62 ~ pp.
Working Group on California Earthquake Probabilities, 1990. Probabilities of Large Earthquakes in the San Francisco Bay Region, California, USGS Circular 1053.
Working Group on California Earthquake Probabilities, 1995. Seismic hazards in southern California: probable earthquakes, 1994–2024. *Bulletin Seismological Society of America*, **85**, 379–439.
Working Group on California Earthquake Probabilities, 2002. Earthquake probabilities in the San Francisco Bay region: 2002 to 2031, USGS Circular 1189.
Working Group on California Earthquake Probabilities, 2008. The Uniform California Earthquake Rupture Forecast, Version 2 (UCERF 2): U.S. Geological Survey Open-File Report 2007–1437 and California Geological Survey Special Report 203 [http://pubs.usgs.gov/of/2007/1437/].

Cross-references

Earthquake Precursors and Prediction
Earthquake Rupture: Inverse Problem
Earthquakes and Crustal Deformation
Earthquakes, Energy
Earthquake, Location Techniques
GPS, Tectonic Geodesy
Great Earthquakes
Paleoseismology
Seismic Hazard
Seismicity, Subduction Zone
Seismology, Global Earthquake Model
Statistical Seismology

CONTINENTAL DRIFT

Alan G. Smith
Department of Earth Sciences, University of Cambridge, Sedgwick Museum, Cambridge, UK

Definition

Continental drift. The name given to the relative movement between continents.

Introduction

Apparently, continental drift was first postulated by Abraham Ortelius, who made one of the first atlases, in the third edition of his *Thesaurus Geographicus* (Ortelius, 1596) to account for the similarity between the coastlines of western Africa, western Europe, and the eastern Americas. During the next three centuries or so, several other thinkers used this morphological similarity to come to the same conclusion.

Alfred Wegener

Although Ortelius speculated that earthquakes and floods had torn the continents apart, Alfred Wegener, an Austrian meteorologist, was the first to systematically gather the geological evidence for continental drift in his synthesis (Wegener, 1929a), also translated into English (Wegener, 1929b), parts of which had been published as early as 1912 (Wegener, 1912).

Wegener was puzzled in particular by the present-day distribution of former ice-age deposits, or tillites, of Permo-Carboniferous age, now known to be about 300 million years old that are found today in South America, Africa, Antarctica, India, and Australia. Wegener's meteorological background led him to assume that the present-day climatic zones, with cold polar regions and a hot tropical belt, was a fundamental property of the Earth's atmosphere that had been established before these glacial deposits had formed and had persisted to the present-day. He realized that if all the southern continents had been joined together to form a supercontinent lying near the south geographic pole, then the *present-day* distribution of all the Permo-Carboniferous tillites would have a logical explanation. This supercontinent is known as Gondwana. But Wegener went further and postulated that the northern continents had also been joined to form a northern supercontinent known as Laurasia, which, with Gondwana, formed a huge continental area incorporating all the major continents, known as Pangea.

Wegener's solution to the tillite distribution had a compelling elegance about it, partly because it also placed the Carboniferous forests of Europe and North America, (whose compressed remains gave the name to the Carboniferous period) in what would have been the tropical region of that time. However, elegance is not a scientific proof, and Wegener's ideas were rejected by most geophysicists and many geologists, principally

because there were no physical measurements that demonstrated drift and there was also no known *physical* mechanism that could move continents independently of one another [e.g., Jeffreys (1929)].

Wegener (1929a) made the reassembly by positioning the continents at where he presumed the edges of the continents lay, that is, somewhat beyond the present-day coastlines, but his maps were rather schematic. A more convincing Gondwana map, supported by much geological evidence, was made by Du Toit (1937), but the best precomputer map showing the excellence of the fit between the continental edges of South America and Africa was made by Carey (1958). Jeffreys (1964) denied that there was a fit, and it was his denial that in part led Bullard and others to examine how well the continental edges fitted together (Bullard et al., 1965; Everett and Smith, 2008). These ideas were supported by the changes in the Earth's magnetic field preserved in rocks (see *Paleomagnetism, Principles*) determined by workers such as Irving (1964), but the results were *not fully accepted by the geoscience community* until after the plate tectonic revolution.

Conclusions

It is now established that the Earth's lithosphere is divided into a number of rigid *Plate Tectonics, Precambrian* in relative motion. Tracing these motions back in time shows that Gondwana, Laurasia, and Pangea did exist in the past, *vindicating Wegener's idea completely.*

Bibliography

Bullard, E., Everett, J. E., and Smith, A. G., 1965. The fit of the continents around the Atlantic. *Philosophical Transactions of the Royal Society of London*, **A258**, 41–51.

Carey, S. W., 1955. The orocline concept in geotectonics – Part I, Publication No. 28. The Papers and Proceedings of the Royal Society of Tasmania, 89, pp. 255–288.

Carey, S. W., 1958. A tectonic approach to continental drift. In Carey, S. W. (ed.), *Continental Drift: A Symposium*. Hobart: University of Tasmania, pp. 177–355.

Du Toit, A. L., 1937. *Our wandering continents*. Edinburgh: Oliver & Boyd.

Everett, J. E., 1965. The Fit of the Continents around the Atlantic. Ph. D., thesis, Cambridge.

Everett, J. E., and Smith, A. G., 2008. Genesis of a geophysical icon: the Bullard, Everett and Smith reconstruction of the circum-Atlantic continents. *Earth Sciences History*, **27**(1), 1–11. http://pubs.usgs.gov/gip/dynamic/historical.html

Irving, E., 1964. *Palaeomagnetism and its application to geological and geophysical problems*. Wiley: New York, 399 pp.

Jeffreys, H., 1929. *The Earth*. Cambridge: Cambridge University Press.

Jeffreys, H., 1964. How soft is the Earth? *Quarterly Journal of the Royal Astronomical Society*, **5**, 10–22.

Ortelius, A., 1596. Thesaurus geographicus, recognitus et auctus. Antwerp, Ex Officina Plantiniana.

Ortelius, A., 1603. Theatrum orbis terrarum. Abridged edition printed by James Shawe, London.

Smith, A. G., and Hallam, A., 1970. The fit of the southern continents. *Nature*, **225**, 139–144.

Wegener, A. L., 1912. Die Entestehung der kontinente (The origin of continents). *Geologische Rundschau*, **3**, 276–292.

Wegener, A. L., 1929a. Die Entestehung der kontinente und Ozeane. (The origin of continents and oceans). Brunswick, Vieeweg.

Wegener, A. L., 1929b. *The Origin of Continents and Oceans (English translation)*. London: Methuen.

Cross-references

Lithosphere, Continental
Lithosphere, Continental: Thermal Structure
Lithosphere, Mechanical Properties
Lithosphere, Oceanic
Paleomagnetism, Principles
Plate Driving Forces
Plate Motions in Time: Inferences on Driving and Resisting Forces
Plate Tectonics, Precambrian

CONTINENTAL RIFTS

A. M. Celâl Şengör
Eurasia Earth Science Institute, Istanbul Technical University, Istanbul, Turkey

Synonyms

Graben; Taphrogen

Definition

A continental rift (Gregory, 1894; Quennell, 1982, 1985) is a fault-bounded elongate trough under or near which the entire thickness of the lithosphere (see *Lithosphere, Continental*; *Lithosphere, Mechanical Properties*) has been reduced in extension during its formation. Just as old mountain ranges may no longer have any topographic expression because of tectonic and/or erosional events, some, especially old, rifts may no longer appear as troughs for the same reasons, but their original trough shape is recognized by their stratigraphically younger fills, or metamorphically lower grade of their down-dropped central blocks (see *Sedimentary Basins*).

Introduction

Rifts form one of the three main categories of lithospheric-scale structures resulting from differential motion of parts of the lithosphere. Lithospheric shortening creates orogens, simple shear creates keirogens, and stretching creates taphrogens that are collections of rifts (Figure 1). However, at present, only 20.5% of the active plate boundaries show normal convergence and 21% normal divergence. Some 8% show pure dextral strike-slip and some 6% pure sinistral strike-slip. The remaining 58.5% display some deviation from the three end-members, with relative motion vector angles to bountary strikes varying between 0° and 67° (Woodcock, 1986). Plate boundaries must have shown a similar behavior in the past, so only about half of all the rifts a geologist may encounter is likely to show normal extension

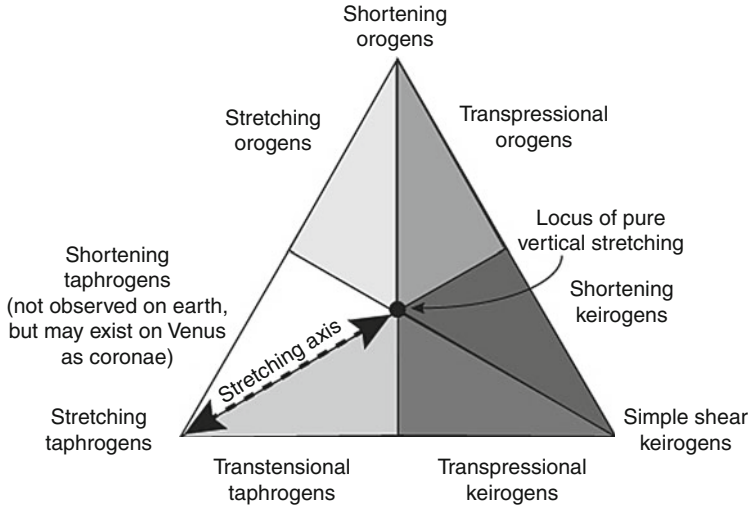

Continental Rifts, Figure 1 A ternary diagram of strain showing the three lithospheric megastructure categories resulting from various strains.

(see *Plate Motions in Time: Inferences on Driving and Resisting Forces*; *Plates and Paleoreconstructions*).

Rifts are important structures from the viewpoints of our understanding of the behavior of our planet and our exploitation of its resources. They record evidence of continental fragmentation in diverse tectonic settings, including all three types of plate boundaries and in plate interiors (see *Plate Motions in Time: Inferences on Driving and Resisting Forces*; *Plates and Paleoreconstructions*). Also, at different stages of their evolution, they present opportunities of studying the continental crust (and in extreme cases even the upper mantle) from its surficial sedimentary rocks down to the crust-mantle interface (see *Lithosphere, Continental*). Especially the lacustrine sedimentary sections of rifts are useful for studies on the past climates (e.g., Olson and Kent, 1999; Kravchinsky et al., 2003; Felton et al., 2007) and they have enabled geologists to refine stratigraphic correlations down to thousands of years, as far back as in the early Mesozoic (e.g., Olsen and Kent, 1999).

Rifts house important economic reserves such as hydrocarbons (the Sirt rift in Libya being the most productive with about 45 billion barrels of oil and 33 trillion cubic feet of gas; for the hydrocarbon potential of rifts, see Harding, 1983; MacKenzie and McKenzie, 1983: a classic on hydrocarbon genesis in rifts; Ziegler, 1994a; Lambiase, 1995), hydrothermal and stratiform copper, copper-nickel, molybdenum, giant lead-zinc, and even uranium deposits (for metallogenesis in rifts, see Sawkins, 1990). Most of the geothermal areas in the world are located in active rifts (e.g., Jaffé, 1971; figure 1) (see *Geothermal Heat Pumps*). At present, one fifth of the entire fresh-water reserve of the earth resides in a rift basin, namely Lake Baykal. Rifts are thus significant not only for increasing our geological knowledge, but also for contributing to our well-being. It is perhaps of some interest in this context to remember that our genus and species were born in a rift, namely in the East African.

For good overviews of rifts and rifting, see Burke and Dewey (1973), Burke and Wilson (1976), Coward et al. (1987), McKenzie (1978) (a "must" read for understanding the evolution of rifts), Manspeizer (1988), Ziegler (1992, 1994b), Landon (1994), Şengör (1995), Şengör and Natal in (2001) (a detailed catalog of the world's rifts with tabulated summaries of origin and history and references) and Ring and Wernicke (2009). For the geology of some of the classic rift regions of the world, with increasing age, see Africa as a whole: Kampunzu and Lubala (1991), Burke (1996), and Burke and Gunnell (2008). East Africa: Frostick et al. (1986), Frostick (1997) (a good introduction for beginner), Schlüter (1997) (this book has a bibliography of some 1,300 items), Morley (1999) (has an excellent collection of seismic sections). Basin-and-Range: Wernicke (1990), Beratan (1996), Faulds and Stewart (1998), Snow and Wernicke (2000), Dickinson (2002) (best introduction for an outsider) and McQuarrie and Wernicke (2005) (best kinematic reconstruction of any rift I know). Rio Grande rift, USA: Ingersoll (2001). The Upper Rhine rift: see the special issue on it in the *International Journal of Earth Sciences (Geologische Rundschau)*, vol. 94 (2005); also: Hüttner (1991), Schumacher (2002), Rotstein et al. (2006). The Lake Baykal rift: Crane et al. (1991), Kuz'min et al. (2001), ten Brink and Taylor (2002), Kravchinsky et al. (2003). The West Siberian Basin: Surkov et al. (1994). The North Sea Basin with the North German (Lower Saxony) Basin: Blundell and Gibbs (1990), Evans et al. (2003) (this lavishly illustrated and richly documented mammoth book makes all earlier publications on the subject either obsolete or redundant; also available as a two CD-ROM set), Wilson et al. (2004), Littke et al. (2008). The Mediterranean region: Durand

et al. (1999), Corti et al. (2006) (an excellent paper about a little-known rift cluster).

Rift, graben, and taphrogen

"Rift" and "graben" are two words used interchangeably in the international literature designating elongate troughs bounded by normal faults. However, not all such troughs are parts of structures that rupture, or even thin by rock creep, the entire lithosphere. Some normal-fault-bounded troughs result from sliding and stretching of surficial rocks over lubricating sedimentary horizons such as evaporites or shales. The normal-fault-bounded basinets that formed during a landslide associated with the March 27, 1964, Prince William Sound earthquake in Alaska or the similar troughs in the Canyonlands National Park in Utah formed by sliding and stretching the sedimentary section above the Upper Carboniferous evaporites are examples. Such structures have nothing to do with lithospheric stretching and thus they do not fit the definition of rift given above. Şengör (1995) therefore suggested that the word rift be confined to those structures that actually disrupt or otherwise (by creep) thin the lithosphere and graben be reserved for those that do not. His usage is what is recommended and followed in this entry. In rifts, when the extension factor β, the ratio of extended width to unextended width (McKenzie, 1978), goes beyond 3 the continental lithosphere generally ruptures completely, and ocean generation begins by seafloor spreading (Le Pichon and Sibuet, 1981) (see *Seafloor Spreading*) either by dyke injection or by cold extrusion of subcontinental mantle in the form of ultramafic "core complexes" as seen in such places as along the boundary between the Upper Penninic and the Lower Austroalpine units of the Alps (Bernoulli et al., 2003 and the references therein) or along the South Galicia Bank (Boillot et al., 1987). For obvious reasons, this cannot happen to grabens, however much they may be extended.

Large regions of localized extension exist on our planet where many rifts and grabens occur together. It is inappropriate to call such regions simply rifts. It would be like calling whole orogens simply "thrust wedges." These large regions of extension are the extensional counterparts of orogens (Figures 1 and 9) and therefore it is appropriate to use for them the term "taphrogen," derived from Krenkel's term "taphrogeny."

General properties of rifts

Structure of rifts

Figure 2 is an idealized and highly simplified block diagram of a rift. Rifts have two fundamental structural entities: a main hanging wall block and one or two footwall blocks depending on whether the rift is symmetric (as in Figure 2) or asymmetric (see Figure 3). In symmetric rifts, the extension represented by the rift is almost entirely localized between two master bounding normal (or oblique extensional) fault systems, and it is these two systems that take up much of the extension, although the hanging wall block delimited by them is also intensely broken up by smaller normal faults with strikes largely parallel with those of the major bounding fault families (Figure 4). The hanging wall is commonly dropped down because of crustal thinning affecting it and in the basin thus formed sediments accumulate whose thicknesses can be in excess of 15 km in large rifts such as the Dneper-Donetz rift in the Ukraine (Ulmishek et al., 1994), which is very close to the maximum possible

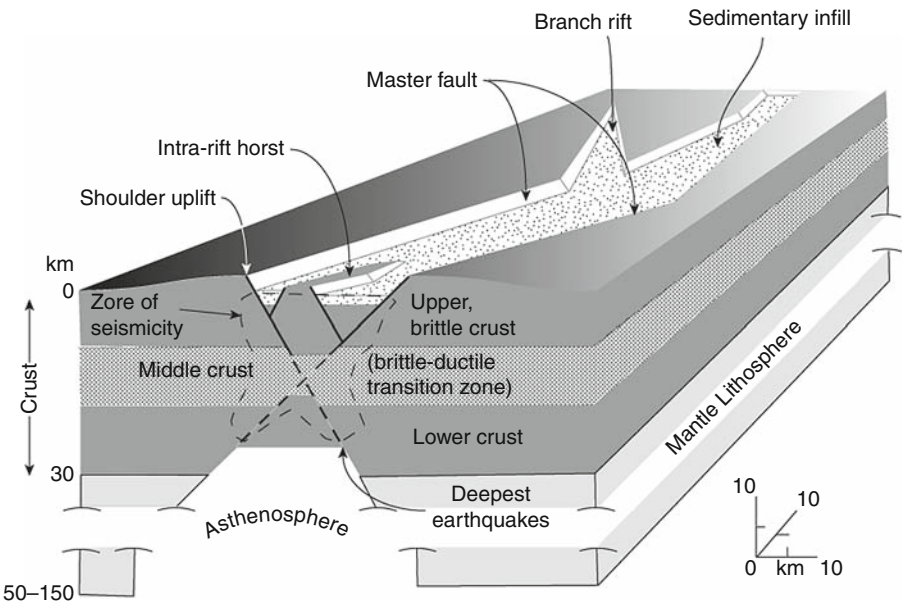

Continental Rifts, Figure 2 A highly schematic block diagram of an "ideal" rift drawn to emphasize the main architectural elements of rifts. The straight marginal faults, e.g., do not mean that all rifts must have straight faults or that they are single faults instead of fault families.

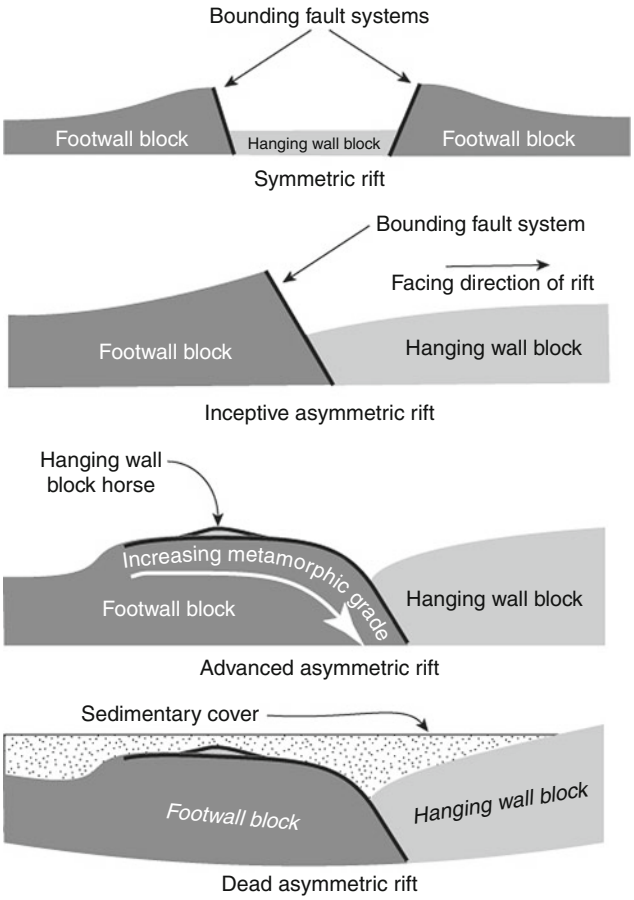

Continental Rifts, Figure 3 Some properties of symmetric and asymmetric rifts.

thickness (17 km) of sediment accumulation on continental crust (Dewey, 1982) Most rifts of average size, however, have sediment thicknesses ranging from 2 to 5 km. Individual rift lengths vary from about 1,000 to 100 km and widths from about 150 to 10 km. Rift size is a function not only of the amount of extension, but also the thickness of the lithosphere it disrupts. The thicker the lithosphere, the wider the rift. On Figure 5, the distribution of continental rifts on earth is shown. In areas of thick lithosphere (e.g., in the North American craton, eastern Europe, and Siberian craton), the rifts are very wide, whereas in areas of thin lithosphere such as the western USA or in the Aegean they are very narrow, in places less than 10 km wide.

The bounding faults of the rifts have long been thought to be listric (shovel-shaped), i.e., flattening with depth, although studies on earthquakes have not supported this. Wherever precise hypocenter location is possible and where the earthquake has caused a surface rupture (see *Earthquake, Focal Mechanism*; *Earthquakes and Crustal Deformation*; *Earthquake, Location Techniques*), it is seen that the associated fault is planar down to depths of 8–10 km. Eyidoğan and Jackson (1985) documented that the March 28, 1969, Demirci earthquake in western Turkey consists of two discrete sub-events: one along a northerly-dipping planar normal fault and another one on a horizontal surface north of, but at the same depth as, the hypocenter of the first one. The horizontal rupture is believed to be located in a region that deforms ductiley under long-term strain rates, but ruptures when that rate is suddenly increased as in an earthquake (Figure 2). This suggests a kinked cross-section for the master fault. Such "kinked" faulting events may be the explanation of why hanging wall blocks in some rifts are so much more disrupted than the rift shoulders. In areas of thicker lithosphere, however, hypocenters along the master faults of rifts may be as deep as 30 km as exemplified by the March 10, 1989, Malawi earthquake in east Africa (Figure 2; Jackson and Belkinsop, 1993) (see *Seismicity, Intraplate*).

The straight fault hypothesis is difficult to generalize, especially where the master fault families bounding rifts are strongly curved in map view such as those that created the Lake Tanganyika rift system (Burgess et al., 1988). It is possible that individual segments of large faults rupture as straight fractures, but eventually the entire fault acquires a listric geometry. This seems supported by the fact that in Lake Tanganyika, where the rift floor has deeply subsided, faulting within the hanging wall block is less intense (Burgess et al., 1988). This is incompatible with a major kink of the master fault at depth. Wernicke and Burchfiel (1982) pointed out that where numerous, parallel-striking planar normal faults have rotated in unison around horizontal axes, one listric fault at the head of the series is a kinematic necessity to allow the others to rotate.

Asymmetric rifts are said to "face" in the direction of the dip of their master faults (Figure 3). Many major rifts are made up of half rifts that change their facing along the strike. In such cases, "transfer" or "accommodation zones" form along their boundaries that take the form of areas of complex oblique faulting and crustal block rotations (see especially the excellent discussions on transfer and accommodation zones in Faulds and Stewart, 1998; also Derer et al., 2005). Smaller and shallower transfer faults, essentially tear faults disrupting the hanging wall block with complicated displacement histories, form where the hanging wall is differentially stretched along the strike of the rift (cf. Şengör, 1987).

Rift shoulders are commonly uplifted. In symmetric rifts, both shoulders go up because of isostatic adjustment of the crustal wedges that are formed by the master faults dipping towards the rift (see *Isostasy*). Such uplift not only rotates the land surface on the shoulders away from the rift thus guiding much of the regional drainage in the same direction, but it rotates also the bounding normal faults (Buck, 1988). Each increment of faulting further rotates the shoulder and further rotates the previously formed fault segment. In Figure 3, in the case of a young asymmetric rift, the fault is shown to be straight. As the rift age and extension advance, the fault surface curves away from the rift as a result of incremental rotations and finally its oldest parts acquire a flat position, possibly with "horses" of the hanging wall block stuck on it as

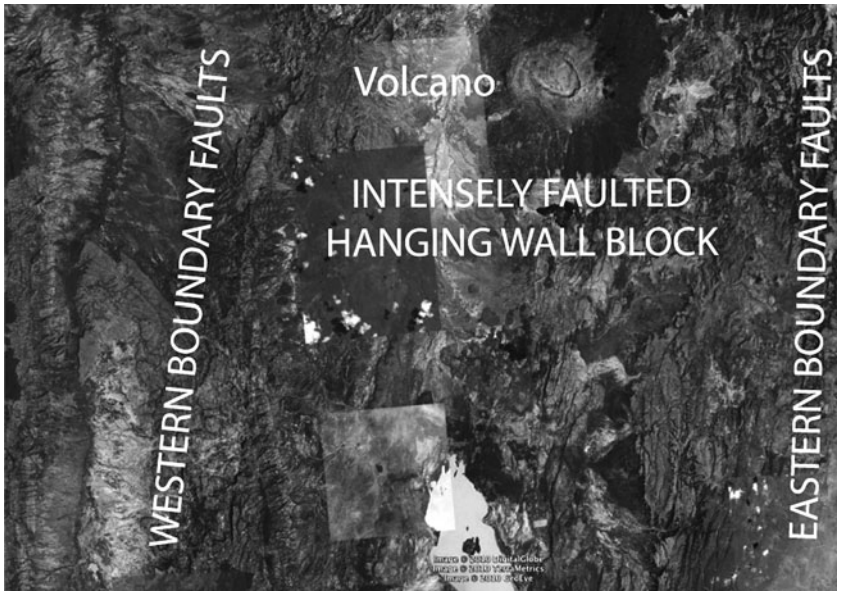

Continental Rifts, Figure 4 A part of the eastern ("Gregory") rift in Kenya showing the intense faulting of the down-dropped hanging wall block between the master fault families. (Google Earth image.)

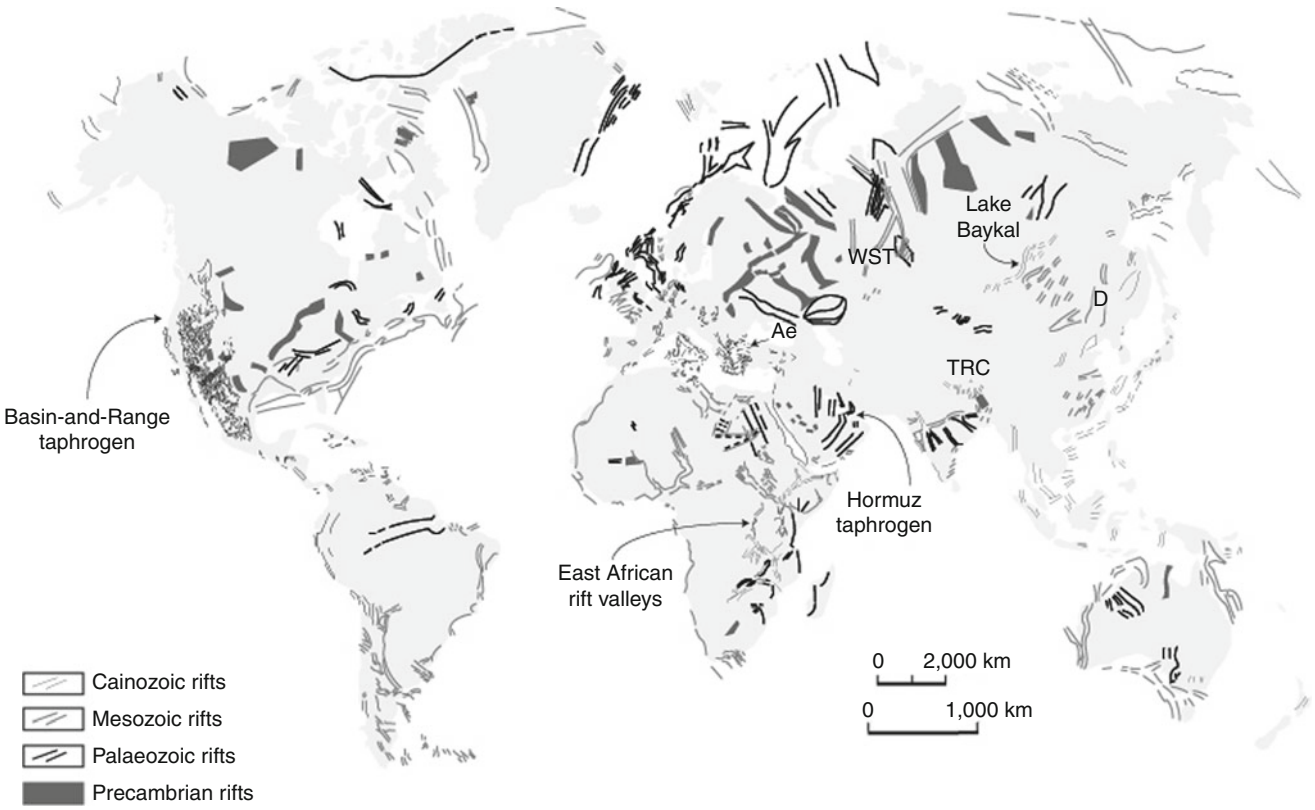

Continental Rifts, Figure 5 Distribution of continental rifts in the world. (Updated from Şengör and Natal'in, 2001.)

"extensional allochthons" (Figure 3). This seems to be the origin of many near-horizontal normal faults in areas of thin lithosphere and large amounts of extension such as the extensional metamorphic core complexes of the North American Cordillera (Armstrong, 1982), or those of the Tethysides (Verdel et al., 2007), although the existence of "primary" low-angle normal faults is also known both from detailed field studies (e.g., Miller and John, 1988) and from the seismicity (Eyidoğan and Jackson, 1985; Abers et al., 1997). The amount of extension in many rifts, especially those that are symmetric, do not go that far, however, and their bounding faults rarely dip less that 30°.

In places where intracontinental rifting along a narrow rift valley has advanced far, as, e.g., along the Wonji Fault Belt in Ethiopia, it has been noted that faulting is driven by dyke injection below the brittle upper carapace of about 10 km thickness and that segments with active deformation at the surface correlate with those of active magmatism (Kendall et al., 2005; Casey et al., 2006).

Cloos (1939) believed that the shoulder uplift in symmetric rifts resulted from the original doming that had led to keystone drop of the hanging wall block, but it was quickly realized that the observed angles of slope on crustal domes rarely exceed 1°, whereas to give rise to substantial rifts one needs about 10° dome slopes, which are excessive. Table 1 lists values of extension and shoulder uplift in some selected rifts. In none, except possibly in the Española Basin, is the shoulder uplift sufficient to cause the estimated amount of stretching.

Sedimentation in rifts

Because rifts form elongate basins they are ideal sediment receptacles. The type of sediment to be found in a rift varies according to the size and geometry of the rift, the climatic zone(s) in which it is located and its evolutionary history. Although most rifts are filled slowly by sedimentation in the sea, lakes, rivers and, in a subordinate degree, subaerially by wind, some are catastrophically invaded by the sea by breaching the barriers of sub-sea-level rift complexes (e.g., the Permian North Sea or the medial Cretaceous South Atlantic). In such cases, either vast evaporite deposits (as in the Aptian of the South Atlantic: Burke and Şengör, 1988) or thick shales (as in the late Permian of the North sea: Evans et al., 2003) are laid down in rift troughs.

Subaerial rifts are normally fed by rivers that locally create lakes within them because of endorheic conditions. Near the fault-bounded shoulders, stream valleys are commonly short (as the crest of the shoulder often is also the water-divide) but the streams in them are energetic because of the steep slopes. They thus carry clastic sediments of a variety of sizes that are horizontally sorted in large alluvial fans at the feet of the fault-escarpments. Along these escarpments, many alluvial fans form and coalesce and ongoing subsidence leads to the accumulation of large thicknesses of fanglomerates, sandstones, and shales near the faulted rift margin(s). Because of rotation towards the fault plane of the basin floors, the sedimentary thicknesses systematically decrease away from rift shoulders towards rift median lines. Steep slopes and catastrophic rain in both tropical and desert climates frequently lead to slope failures resulting in landslides complicating the sedimentary record. Permanent or ephemeral lakes may occupy the middle parts of rift floors. Ephemeral lakes commonly occur in dry climates in the form of playas and deposit evaporites and clays that may interfinger with marginal alluvial fan deposits. Permanent and deep lakes are important sediment repositories in rifts. They may accumulate very thick sedimentary sections in them, exhibiting complex facies dictated by the evolution of the geomorphology of the rift and its surrondings. Such lakes can be very deep (Lake Baykal in Sibearia: with 1,637 m, the world's deepest lake in addition to an 8 km rift sedimentary fill; Lake Tanganyika in

Continental Rifts, Table 1 The amount of stretching and shoulder uplift in some selected rifts (From Şengör, 2001)

Name of rift	Amount extended (km)	Uplift of shoulder area (km)
N Kenya	35–40	>1.4–1.7
Gregory	10	2
Malawi	7.5 (from transfer fault offset)	2.8 (strike-slip affected?)
Suez N	16.3	1.5
Central	17.7–32.6	1
S	29.3 (all from fault geometry)	~500 m
Upper Rhine	17 (from crustal configuration), 5–7 (from fault geometry)	2.2
Oslo	28–36 (from crustal configuration), 11–13 (from fault geometry)	1
Viking	100–130 (from crustal configuration), 30 (from fault geometry)	3
Central (North Sea)	100–105 (from crustal configuration), 15 from fault geometry)	1.5
Benue	100[a]	?
Baykal	15–20 (from crustal configuration), 10 (from fault geometry)	2–3
Española basin	5.5	1.5
Albuquerqe basin N	10 (from fault geometry)	~1
Albuquerqe basin S	16 (from fault geometry)	0.9

[a]Benkhelil et al. (1988) established at least 10 km of shortening during the following compression

East Africa: 1,457 m, but with half the sediment thickness of Lake Baykal). They are well-aerated in cold climates because the cold upper layers of the lake waters make convection and overturning possible (as in Lake Baykal), but they are stratifed with anoxic deeps in hot regions because hot surface waters cannot sink and thus inhibit overturning (as in Tanganyika). As the anoxic conditions in Lake Tanganyika exemplify, deep rift lakes in hot climates may generate good hydrocarbon source rocks in reducing environments. This is corroborated by ancient rift fills that formed under similar conditions such as the Permian oil-bearing sequences in the Junggar and Turfan rift basins in Central Asia (e.g., Graham et al., 1990; Miao et al., 2006) or the organic-rich (up to 8% organic C) Triassic-Jurassic lacustrine sediments of the Newark-type rifts of the eastern USA (Manspeizer and Olsen, 1981).

Rift valley floors are seldom level along the strike of the master bounding faults and this commonly induces longitudinal drainage in rifts. In fact, most of world's major rivers flow in two kinds of valleys: those that are located in rift troughs or in depressions inherited from them and those that are placed in fore- and hinterland basin troughs (cf. Audley-Charles et al., 1977). The Rhine in Europe, the Irrawady in Asia, flow along their almost entire lengths in active rift troughs. Along the western arm of the East African rift valleys, Lake Tanganyika receives (surface elevation at 773 m a.s.l.) the excess waters of Lake Kivu (at 1,460 m) by means of the south flowing river Ruzizi that came into being only 10,600 years ago and may have stopped flowing between 8 and 6,000 years ago (Felton et al., 2007), showing the sensitive dependence of rift sedimentation on the global climate. Farther north, just beyond Kivu, Lake Edward (at 912 m) is connected to Lake Albert (at 619 m) through the northerly flowing river Semliki. Lake Albert in turn feeds the Nile northwards via the river Albert Nile (White Nile or "Bahr al Jebel," i.e., "the river of the mountain").

In the sedimentary record, the rift facies is commonly characterized by thick (2–15 km) clastic sequences with rapid thickness and facies changes both laterally and vertically. If the rifts are underwater and far from clastic sources, they may house carbonate and even siliceous sedimentary sections as illustrated by the Alpine Triassic-early Jurassic facies. There, a continuous passage from late Triassic shallow water carbonates via a horizon of extensional-faulting-related neptunian dykes filled with progressively deepening facies and finally covered entirely by radiolarian cherts indicates a stretching basin floor as it deepened. That no shoulder uplift is indicated by any unconformities suggests that the Alpine rift was asymmetric with a major south-dipping detachment, and that the rocks on the hanging wall block never experinced normal-fault-related upheaval. If catastrophic marine invasion occurs, then sediments at once blanket the preexisting topography.

For good reviews of sedimentation in rifts, see Frostick et al. (1986), Lorenz (1988), Olsen and Schlische (1990), Leeder (1995), Şengör (1995), Beratan (1996), also the section entitled "Rift Basins" in Einsele (2000, pp. 543–560).

Magmatism in rifts

Rift magmatism is extremely variable because the tectonic environments in which rifts form are so diverse (see below). Rifts that form above mantle plumes (see *Mantle Plumes*) in plate interiors away from plate boundaries may begin their activity with restricted volumes of alkalic basalts indicating limited partial melting of mantle material at depth and may evolve towards abundant tholeiitic effusions as the temperature at depth increases and more and more mantle rock is melted, as, for example, illustrated by the evolution of the Afar plume in east Africa. Most geologists take alkalic to peralkalic magmatism as indication of extensional tectonics. The frequent association of nepheline syenites, kindred alkaline igneous rocks, and carbonatites (alkalic rocks and carbonatites [ARCs]) with intracontinental rifts has been taken by Burke et al. (2003, 2008) to argue that deformed rocks of the same compositions (deformed alkalic rocks and carbonatites [DARCs]) that have been shown to characterize suture zones in regions in Asia, Europe, Africa, and North America are nothing but ARC rocks that erupted into intracontinental rifts that became involved in a Wilson cycle of ocean opening and closing. This has been shown to form a powerful tool to map suture zones where other suture indicators such as ophiolites or subduction-related rocks may be missing. However, to think that rifts generate only alkalic magmatic rocks is clearly too simplistic. Those rifts that form along magmatic arc systems, for instance, inevitably have calc-alkalic magmas and those that form above recently thickened continental crust may generate vast quantities of calc-alkalic andesitic/rhyolitic melts. Rifts forming in back-arc regions, such as those in the Aegean, contain volcanic rocks showing evidence for a metasomatised mantle beneath them (e.g., the so-called Kulaites, i.e., hornblende basalts, in western Turkey: Richardson-Bunbury, 1996). Large amounts of silica-rich magmatic rocks may be generated if mantle plumes manage to melt large quantities of continental crust while ascending or if fractional crystallization is allowed to proceed undisturbed (e.g., the Cretaceous tin granites in Nigeria or the Cainozoic granites in Scotland; see Wiart and Oppenheimer, 2004 for an acitve example in Afar). Some rifts such as Tanganyika or Baykal are almost entirely devoid of magmatism, while others such as the late Palaeozoic Oslo Rift have floors made up entirely of magmatic rocks. Some Atlantic-type continental margins, which grew out of disrupted rifts, are called "volcanic," whereas others, "non-volcanic," because they descended from rifts with similar magmatic characteristics.

It is naive to think that lithospheric extension generates only certain kinds of magmatic rocks without considering the tectonic environments that gave rise to the extension and in which the extension proceeds. It is therefore

imperative to look at the diversity of the environments which generate rifts.

For good reviews of magmatism in rifts, see Kampunzu and Lubala (1991), Kinnaird (1998), Ulrych et al. (1999), Burke et al. (2003, 2008), Wilson et al. (2004), Yirgou et al. (2006); also the special section on magmatism and extension in *Journal of Geophysical Research*, vol. 100 (1995).

Metamorphism in rifts

Continental rifts are not commonly thought of as prime loci of metamorphic events, but four different kinds of metamorphic rocks do occur in them. In increasing importance: (1) contact metamorphic rocks around rift-related magmatic rocks, (2) hydrothermal metmorphism around vents, (3) burial metamorphism due to large sediment thicknesses, and (4) metamorphic rocks that form within the continental crust and are brought to surface by rifting.

There is little to say about the first kind of metamorphic rocks in rifts as they are no different from any other contact metamorphic rock. Hydrothermal metamorphism is important in many rifts because of the high heat flow and the continuous opening of extensional fractures allowing hot waters to circulate (e.g., Crane et al., 1991). Burial metamorphism is not common in rifts unless they accumulate very large thicknesses of sediment quickly, sufficient to raise the temperature and pressure conditions to initiate metamorphism. If we assume a normal geothermal gradient (~3°C/100 m; see *Heat Flow, Continental*), an accumulation of about 4 km of sediment would be sufficient to initiate metamorphism by raising the temperature beyond 120°C. Jackson (1987) argued, however, that because earthquake hypocenters in rifts are seldom deeper than 10 km, at least beyond that depth rocks must be metamorphic. But since there are earthquakes down to 30 km in the east African rifts system, it is questionable how sound an argument that is. It is true, however, that rift sediments are seldom metamorphosed beyond greenshist grade because they are seldom stretched enough and seldom accumulate sufficient thicknesses of sediment to heat the rocks beyond 320°C. Smith (1976) pointed out, for example, that at the bottom of the about 16 km-thick Gulf Coast sediment pile, the temperature may be just about 320°C under 4 kb pressure. But this ignores both the radioactive heating of the pile (see *Radiogenic Heat Production of Rocks*) and raising the geotherm by stretching. However, even when the crust is stretched, every particle in the stretched crust must cool, unless the rift trough is rapidly sedimented (Figure 6; McKenzie, 1978; Jackson, 1987). Although it has been suggested that some high-grade metamorphic rocks did form in a rift environment (Wickham and Oxburgh, 1985), it was a result of mistaking an orogenic environment for a taphrogenic one, although from elsewhere allegedly rift-related metamorphism creating high-grade gneisses has been reported on the basis of condensed metamorphic zones and absence of associated plutonism

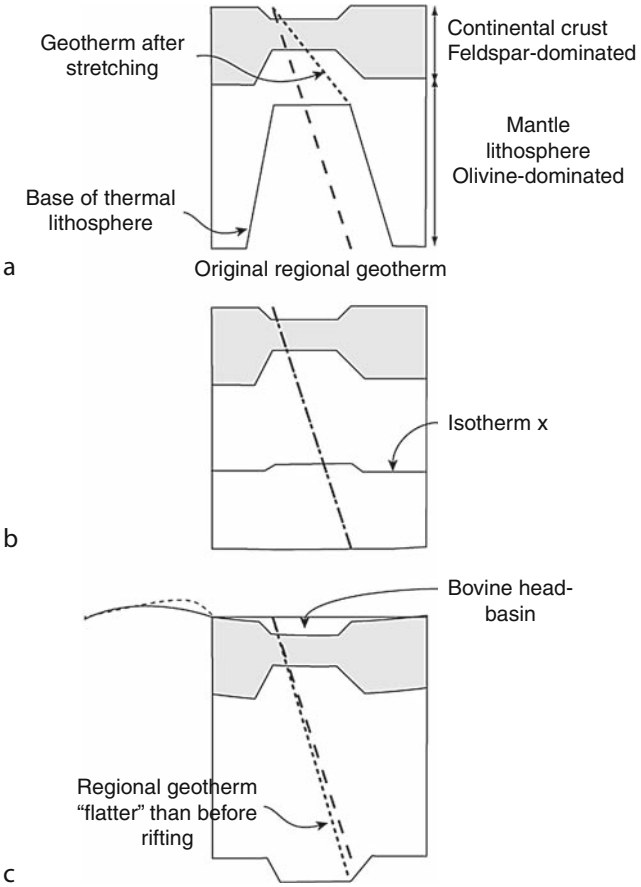

Continental Rifts, Figure 6 Thermal regime of rifts with a simple geotherm. (**a**) Immediately after the stretching, both the crust and the lithospheric mantle thin and isotherms become crowded under the rift increasing the heat flow in the rift. Although no particle in the rift basement will become any hotter. (**b**) After stretching ceases, isotherms begin to subside. (**c**) When the lithosphere "recovers," the rift will end up with more lithospheric mantle beneath it and will have a heavier substratum that will subside and pull its surroundings with it creating an "intracratonic basin" overlying the rift. This is called a "bovine head" cross-section because of its resemblance to a long horn ox. While the basin subsides, its margnis will be elastically uplifted (solid line above **c**), but may relax viscoelastically in time (dotted line above **c**). Here the margins are shown only on one side for graphic convenience, but naturally the events will take place all around the basin.

(e.g., St-Onge and King, 1987). However, I am unaware of any well-documented metamorphic terrane that formed as a consequence of rift burial.

By contrast, large normal faults of the kind shown for the advanced asymmetric rifts in Figure 3 may pull up rocks from the lower continental crust that may have been metamorphosed even up to granulite facies as shown by many extensional metamorphic core complexes. But in this case, the metamorphism is not *caused* by rifting, but it is *exposed* by rifting. In fact, as the rocks ascend

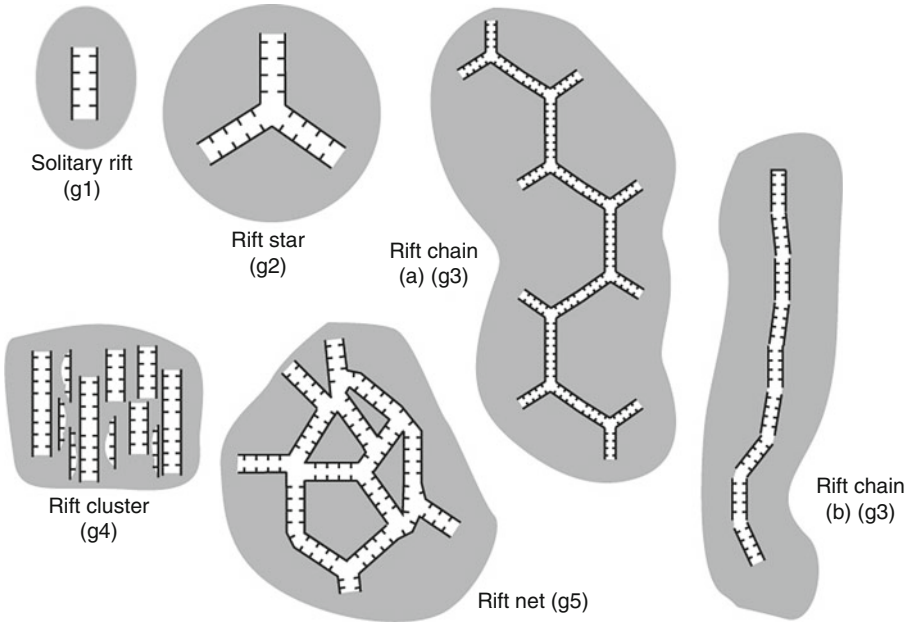

Continental Rifts, Figure 7 The geometric classification of taphrogens. (After Şengör, 1995.)

in the footwall, they get retrograded, which is directly caused by rifting.

For metamorphism in rifts, see Armstrong (1982), Jackson (1987), Lister and Davis (1989), Block and Royden (1990), Verdel et al. (2007).

Kinds of rifts

A classification of rifts must serve to answer the questions: how many different sorts of environments lead to lithospheric extension and what kinds of rifts form in these environments? In essence, one must specify where and how taphrogens commonly form. If taphrogeny stops before producing ocean, it causes subsidence and creates large basins (called "koilogens" by Spizaharsky and Borovikov, 1966, pp. 113ff.) overlying taphrogens (Figure 6; cf. McKenzie, 1978; Şengör, 1995). A comprehensive synthesis of various taphrogen types does not yet exist. Below is a restatement of Şengör's (Şengör, 1995; Şengör and Natal'in, 2001) classification of types of rifts that make up the main elements of taphrogens. That classification is hierarchical and goes from pure geometry to dynamics (Figure 8). Its hierarchical nature allows the environment and the path of formation of a given rift to be determined. For numerous examples of each of Şengör's categories, see Şengör and Natal'in (2001). In this section, references already given in Şengör (1995) and in Şengör and Natal'in (2001) are not repeated.

Şengör's classification has three different categories that do not completely overlap, namely *geometric*, *kinematic*, and *dynamic*. In the following, the three different categories are identified with their initials, i.e., *g*, *k*, and *d*, respectively.

Geometric classification of rifts

Rifts or groups of rifts forming individual taphrogenic units display five kinds of fundamental map patterns (see Figures 7 and 8). From simplest to more complex, these are:

g1 – Solitary rifts: Solitary rifts form small, fairly insignificant, and very rare taphrogens and are extremely difficult to ascertain in the geological record because it is commonly hard to tell whether a given rift fragment is isolated or part of a larger taphrogen (for a comparable difficulty in shortening structures, imagine a big solitary fold or a large thrust fault!).

g2 – Rift stars: Rift stars form when more than two rifts radiate away from a common center, building a roundish taphrogen. Rift stars are very common features of the structural repertoire of our planet today.

g3 – Rift chains: When several rifts are aligned end-to-end along linear/arcuate belts of rifting, they form *rift chains*. The East African Rift System constitutes the best-known active rift chain in the world. Solitary rifts or rift stars or combinations of these may be connected to form different kinds of rift chains (e.g., Figure 7 rift chains a or b).

g4 – Rift clusters: When several subparallel rifts occur in roughly equant areas, they are said to form a *rift cluster*. The two best-known active rift clusters in the world are the Basin-and-Range extensional area in North America and the Aegean Sea and the surrounding regions (see Figure 5).

g5 – Rift nets: Rift nets constitute a rare pattern, which comes about when rifts form a roughly checkered pattern as in the Proterozoic basement of the East European platform or in the late Mesozoic in central North Africa (cf. Şengör and Natal'in, 2001). They resemble

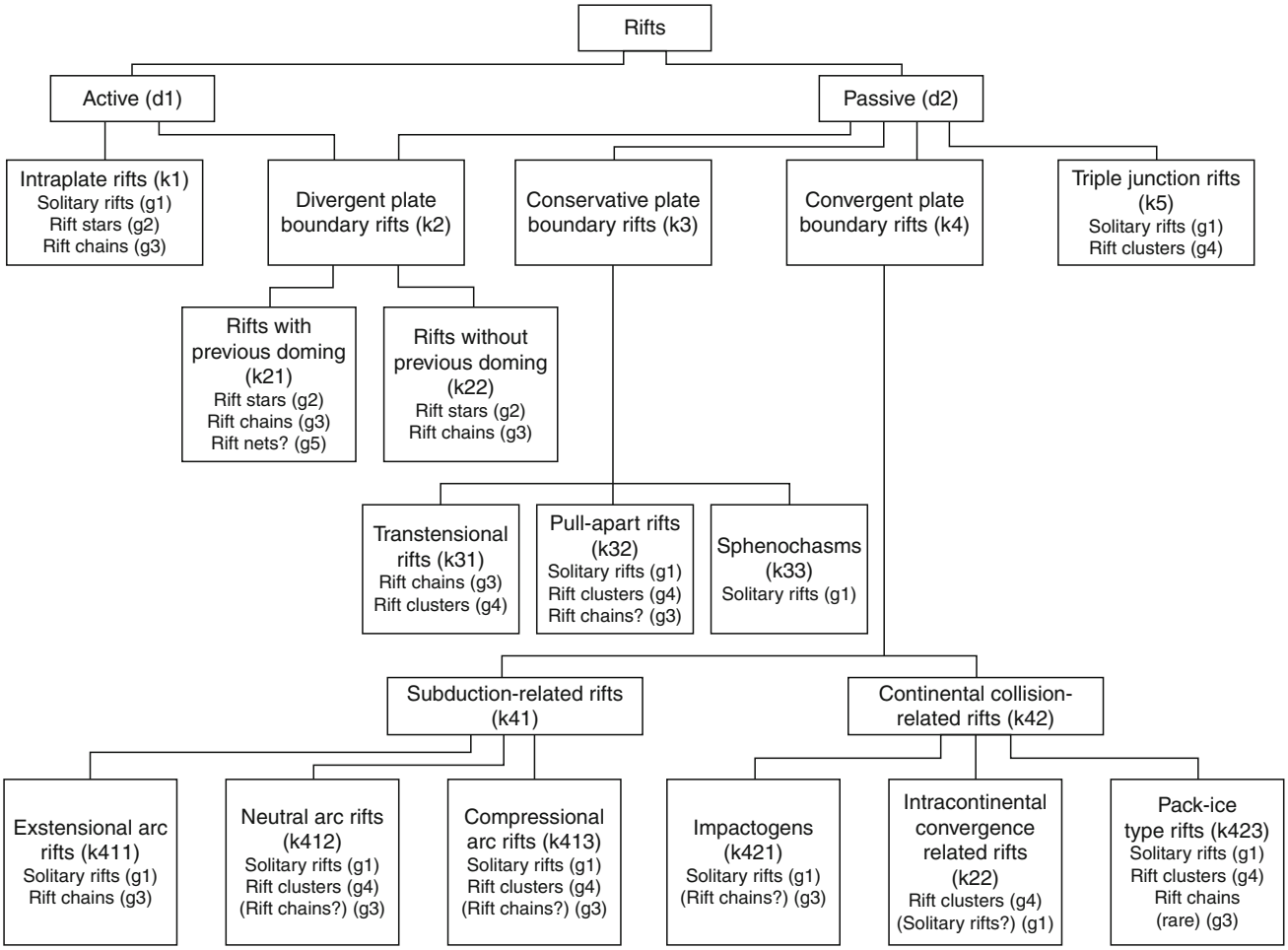

Continental Rifts, Figure 8 The kinematic classification of rifts and taphrogens. (After Şengör, 1995.)

chocolate-bar boudinage, as seen in the Proterozoic basement of eastern Europe (Figure 5), and may have a similar origin, but more commonly rift nets form in complex and rapidly shifting stress environments in which dominant extension directions change fast. Many rift nets in fact may represent two superimposed rift clusters.

Kinematic classification of rifts

Because rifts are ubiquitous in all stages of the Wilson Cycle of ocean opening and closing, the kinematic characteristics of the plate boundaries have been taken as a basis for classifying them according to the environment of the overall displacement and strain in which they form (see Figure 8). There are three types of plate boundaries plus the plate interiors, to which four types of rift families correspond. In addition, incompatibilities arise around some unstable intracontinental triple junctions leading to complex rifting that should be treated separately from the other four classes, thus creating a fifth kinematic class, called "triple-junction rifts."

k1 – Intraplate rifts: Rifts surrounded entirely by undeformed lithosphere occupy this category. Such rifts are usually solitary, small, and rare (the difficulty in forming them is analogous to that forming a solitary fold or a nappe surrounded by entirely undeformed terrain), and are not easy to identify in the geological history. The Lake George and Lake Champlain rifts in the northeastern USA are active examples (see *Seismicity, Intraplate*).

k2 – Rifts associated with divergent plate boundaries: These rifts result from plate separation along nascent extensional boundaries. All the Cainozoic rifts in east Africa belong here. This category of rifts may be further subdivided into two classes as follows:

k21 – Rifts that form following an episode of doming: the divergent boundary along which rifts form is in this case preceded by an episode of lithospheric doming. The East African Rift Valleys are the best-known examples of such rifting (see *Isostasy, Thermal*).

k22 – Rifts that form with no pre-rift doming: in this case, rifts form without a prelude of uplift, as is the case in the Salton Trough and the Gulf of California.

A good fossil example is the rifting of the Alpine Neo-Tethys in the earlier Mesozoic.

k3 – Rifts that form in association with conservative plate boundaries: conservative, i.e., transform fault, boundaries are those along which neither extension nor shortening is required by the regional slip vectors. However, various reasons conspire to induce both extension and shortening to occur along considerable stretches of these boundaries. Rifts along conservative plate boundaries form in three different settings:

k31 – Transtensional conservative boundaries: if a conservative boundary is opening up all along its length because of a component of extension, it is called *transtensional*. Many active rifts have a transtensional component, and fossil examples of such rifts may be recognized largely through the structures they contain as shown by Olsen and Schlische (1990). Dewey (2002) gave an exhaustive analysis of the strain that develops in such rifts.

k32 – Pull-apart basins along conservative boundaries: major strike-slip faults commonly have bends along them that either facilitate ("releasing bends") or obstruct ("restraining bends") slip along them. Extensional basins form along the releasing bends, in which the magnitude of extension equals the magnitude of cumulative strike-slip offset along the strike-slip fault since the formation of the releasing bend. Such basins are called "pull-apart basins." Crowell's (1974) fault-wedge basins are nothing more than special cases of pull-apart basins.

k33 – Sphenochasms: not all basins created by secondary extension associated with strike-slip faults are pull-apart basins. Some represent tears caused by either an asperity or differential drag along the strike-slip fault in one of the fault walls, in which the amount of extension changes from a maximum along the fault to zero at the pole of opening of the tear-basin. S. W. Carey called such wedge-shaped rifts that open towards a major strike-slip fault *sphenochasms*.

k4 – Rifts that form in association with convergent plate boundaries: a large family of rifts forms in association with convergent plate boundaries. In this group, a first-order subdivision is between rifts associated with subduction zones and rifts associated with continental collision, although this may artificially split some genetic groups, such as those rifts that presumably form because of the tension generated by excessive crustal thickening. The usefulness of the present grouping is that it enables a rapid overview of the presently active rift environments and comparison with ancient ones.

k41 – Rifts associated with subduction zones: environments of rifting associated with subduction zones correspond to three different types of arc behavior, namely, extensional, neutral, and compressional arcs.

k411 – Rifts associated with extensional arcs: an extensional arc generally splits along the magmatic axis (if such an axis is already in existence) forming a small rift chain. Such a situation is today known from both the Okinawa rift and the Izu-Bonin arc system. Such rifts commonly do not get preserved intact, both because of the complications of the tectonic evolution of arcs involving common changes of behavior and because of later collisions with other arcs or continents.

In extensional arcs, rifts also develop orthogonal to arc trend owing to the extension of the arc as it bows out in front of an expanding marginal basin (as, for instance, in Crete).

k412 – Rifts associated with neutral arcs: neutral arcs have neither shortening nor extension across them. Therefore, the only rifts that may form in neutral arcs are those associated with arc-parallel strike-slip faults, which may be classified in the same way as the rifts that form along conservative plate boundaries. More complex rift basins may originate along such arc-parallel strike-slip faults if the sliver plate in the forearc area and its various pieces rotate about vertical axes.

Pull-apart basins in arcs are difficult to recognize, but the Sumatra Fault has several well-developed examples along it.

Sphenochasms along strike-slip faults in arcs are rarer still. Davis et al. (1978) have discussed two possible examples: the more recent of which may have created the "Columbia Embayment" by motion along the Straight Creek fault in the latest Cretaceous and the earliest Cainozoic.

k413 – Rifts associated with compressional arcs: in compressional arcs crust commonly thickens and lithosphere thins, both by heating and by eventual delamination. The arc becomes shortened across and elongated along its trend. This elongation commonly generates rifts at high angles to the trend of the arc. Rifts on the Altiplano in the Andes are examples of such high-angle rifts.

k42 – Rifts associated with zones of continental collision: three different environments of rifting form associated with the collision of continents: (1) *Lines of extension* that radiate from points at which collision commences, (2) *Regions of extension* abutting against sutures, and (3) *Nodes of extension* in areas of complex deformation in fore- and hinterlands shattered by collisions. Impactogens (k421), rifts forming in intracontinental convergence belts (k422), and pack-ice-type rifts (k423) correspond with these three environments, respectively.

k5 – Triple-junction rifts: Triple-junction rifts form at or near unstable intracontinental triple junctions, at which plate evolution dictates the generation of "holes" because continental lithosphere cannot be continuously subducted.

Dynamic (genetic) classification of rifts

Rifts are also classified according to the origin of forces (see *Geodynamics*) that lead to rifting (see Figure 6).

Şengör and Burke (1978) proposed that stresses which cause rifting may be imposed on the lithosphere directly by the mantle beneath it (cf. Şengör, 2001) or they may result from two-dimensional plate evolution. Accordingly, they termed these two modes of rifting "active" and "passive." Gans (1987) tried to replace these terms with "open-system' and "closed-system" rifting, respectively, which, however, did not find general acceptance.

d1 – Active rifting: "Active rifting" is rifting caused by mantle upwelling (see *Earth, Density Distribution*; *Mantle Convection*) associated with plumes in the mantle (see *Mantle Plumes*). Two views have been advanced to explain the origin of the extension in domes rising above hot-spot jets: one ascribes the rifting to basal shear stresses induced by a spreading plume head beneath a dome. The other holds the potential energy of the rising dome responsible for driving the rifting. All of these factors probably do contribute to maintaining the active rifting process at its habitually slow pace of considerably less than 1 cm/a (see *Geoid*).

Plume-caused taprogens may be also termed deeply rooted rifts and would be the extensional counterparts of subduction-related orogens (Figure 9a, b). These can be contrasted to collisional orogens that have lost their subductive "anchors" and the passive rifts with no deep mantle connections (Figure 9c, d).

d2 – Passive rifting: in the passive rifting mode, extension is caused by the two-dimensional motions of the lithospheric plates and not by an autonomous interference from the mantle (Figure 9d). In this mode of rifting, there is no pre-rifting doming associated with a hot-spot (Şengör and Burke, 1978). Kinematic mechanisms reviewed above under the headings k22, k31, k32, k33, k411, k412, k413, k421, k422, k423, and k5 all may form rifts in a "passive rifting mode."

There is only one kind of rift this classification does not consider: rifts that form by propagating from an already existing rift. Since propagation may take many forms, it might be sufficient to indicate such rifts with the notation d2 to indicate their passive mode of opening. The regional geologist may use Figure 8 as a "flow chart" to follow the evolutionary histories of the various kinds of rift basins he encounters.

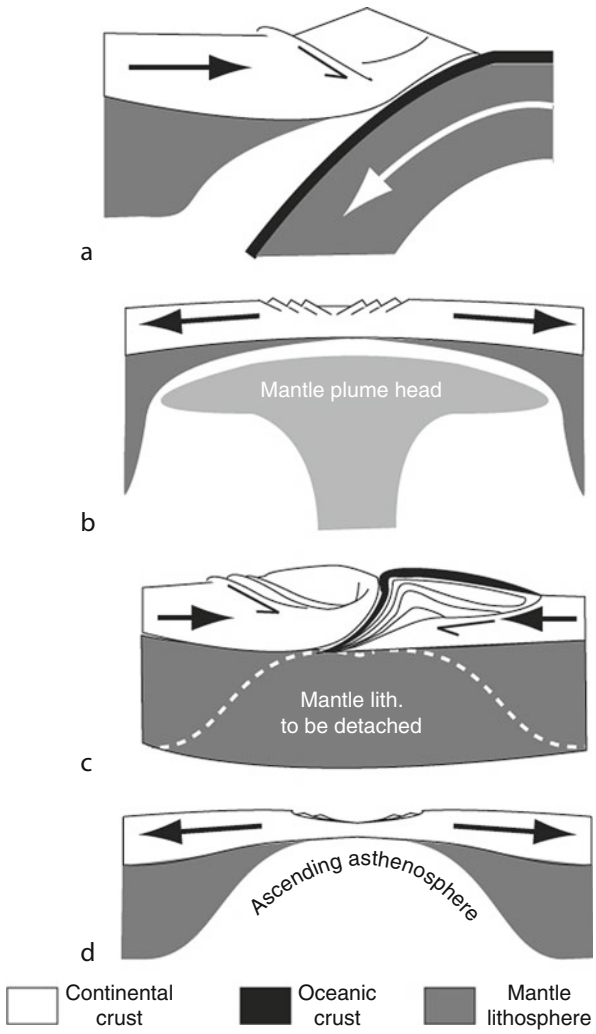

Continental Rifts, Figure 9 Deeply rooted megastructures. (**a**) Subduction-controlled orogens; (**b**) mantle-plume controlled, i.e., active rifts and rootless megastructures; (**c**) collisional orogens; (**d**) plate motion-controlled, i.e., passive rifts.

Conclusions

Although they constitute one of the three great continental structure types and have serious relevance to human well-being, rifts remain poorly known. This is largely because there are still important technological difficulties in studying them directly because of the large sediment thicknesses they contain and because their diversity is little appreciated. They are so ubiquitous in all tectonic environments that they tend to be overlooked in favor of other, rarer, structures that may appear more prominent. It is commonly not recognized that all kinds of structures, such as magmatic arcs, collisional orogens, keirogens, intracratonic basins all have associated rifts and, consequently, people wishing to know about rifts tend not to concern themselves with them. A stereotypic rift that commonly bedevils textbooks is one that disrupts a craton and has alkalic or peralkalic vulcanism with a thick, mainly nonmarine sedimentary fill, although there are many more rifts in the world than those with such characteristics. What is now needed in rift studies is a comprehensive synthesis that takes into account this diversity.

Bibliography

Abers, G. A., Mutter, C. Z., and Fang, J., 1997. Shallow dips of normal faults during rapid extension: earthquakes in the Woodlark-d'Entrecasteaux rift system, Papua New Guinea. *Journal of Geophysical Research*, **102**, 15,301–15,307.

Armstrong, R. L., 1982. Cordilleran metamorphic core complexes – from Arizona to Southern Canada. *Annual Review of Earth and Planetary Science Letters*, **10**, 129–154.

Audley-Charles, M. G., Curray, J. R., and Evans, G., 1977. Location of major deltas. *Geology*, **5**, 341–4.

Beratan, K. K. (ed.), 1996. Reconstructing the history of basin and range extension using sedimentology and stratigraphy. Geological Society of America special paper 303, vi + 212 pp. + 1 folded plate in pocket.

Bernoulli, D., Manatschal, G., Desmurs, L., and Müntener, O., 2003. Where did Gustav Steinmann see the trinity? Back to the roots of an Alpine ophiolite concept. In Dilek, Y., and Newcomb, S. (eds.), *Ophiolite Concept and the Evolution of Geological Thought*. Geological Society of America special paper 373, pp. 93–110.

Block, L., and Royden, L. H., 1990. Core complex geometries and regional scale flow in the lower crust. *Tectonics*, **9**, 557–567.

Blundell, D. J., and Gibbs, A. D. (eds.), 1990. *Tectonic Evolution of the North Sea Rifts*. Oxford: Clarendon.

Boillot, G., Recq, M., Winterer, E. L., Meyer, A. W., Applegate, J., Baltuck, M., Bergen, J. A., Comas, M. C., Davies, T. A., Dunham, K., Evans, C. A., Girardeau, J., Goldberg, G., Haggerty, J., Jansa, L. F., Johnson, J. A., Kasahara, J., Loreau, J. P., Luna-Sierra, E., Moullade, M., Ogg, J., Sarti, M., Thurow, J., and Williamson, M., 1987. Tectonic denudation of the upper mantle along passive margins: a model based on drilling results (ODP leg 103, western Galicia margin, Spain). *Tectonophysics*, **132**, 335–342.

Buck, R., 1988. Flexural rotation of normal faults. *Tectonics*, **7**, 959–973.

Burgess, C. F., Rosendahl, B. R., Sander, S., Burgess, C. A., Lambiase, J., Derksen, S., and Meader, N., 1988. The structural and stratigraphic evolution of Lake Tanganyika: a case study of continental rifting. In Manspeizer, W. (ed.), *Triassic-Jurassic Rifting – Continental Breakup and the Origin of the Atlantic Ocean and Passive Margins B*. Amsterdam: Elsevier, pp. 859–881.

Burke, K., 1996. The African plate. *South African Journal of Geology*, **99**, 339–409.

Burke, K., and Dewey, J., 1973. Plume-generated triple junctions: key indicators in applying plate tectonics to old rocks. *Journal of Geology*, **81**, 406–433.

Burke, K., and Gunnell, Y., 2008. The African erosion surface: a continental-scale synthesis of geomorphology, tectonics, and environmental change over the past 180 million years. Geological Society of America memoir 201, iv + 66 pp.

Burke, K., and Şengör, A. M. C., 1988. Ten metre global sea-level change associated with South Atlantic Aptian salt deposition. *Marine Geology*, **83**, 309–312.

Burke, K., and Wilson, J. T., 1976. Hot spots on the earth's surface. *Scientific American*, **235**, 46–57.

Burke, K., Ashwal, L. D., and Webb, S., 2003. New way to map old sutures using deformed alkaline rocks and carbonatites. *Geology*, **31**, 391–394.

Burke, K., Khan, S. D., and Mart, R. W., 2008. Grenville Province and Monteregian carbonatite and nepheline syenite distribution related to rifting, collision, and plume passage. *Geology*, **36**, 983–986.

Casey, M., Ebinger, C., Keir, D., Gloaguen, R., and Mohamed, F., 2006. Strain accommodation in transitional rifts: extension by magma intrusion and faulting in Ethiopian rift magmatic segments. In Yirgou, G., Ebinger, C. J., and Maguire, P. K. H. (eds.), *The Afar Volcanic Province Within the East African Rift System*. Geological Society special publication 259, pp. 143–163.

Cloos, H., 1939. Hebung-Spaltung-Vulkanismus – Elemente einer Geometrischen Analyse Irdischer Großformen. *Geologische Rundschau*, **30**(Zwischenheft 4A), 405–527.

Corti, G., Cuffaro, M., Doglioni, C., Innocenti, F., and Manetti, P., 2006. Coexisting geodynamic processes in the Sicily Channel. In Dilek, Y., and Pavlides, S. (eds.), *Postcollisional Tectonics and Magmatism in the Mediterranean Region and Asia*. Geological Society of America special paper 409, pp. 83–96.

Coward, M. P., Dewey, J. F., and Hancock, P. L. (eds.), 1987. Continental extensional tectonics. Geological Society special publication 321 (Albert M. Quennell volume), 637 pp.

Crane, K., Hecker, B., and Golubev, V., 1991. Heat flow and hydrothermal vents in Lake Baikal, U.S.S.R. *EOS Transactions of the American Geophysical Union*, **72**, 585–588.

Crowell, J. W., 1974. Sedimentation along the San Andreas Fault, California. In Dickinson, W. R. (ed.), *Plate Tectonics and Sedimentation*. Society of Economic Paleontologists and Mineralogists special publication 19, pp. 292–303.

Davis, G. A., Monger, J. W. H., and Burchfiel, B. C., 1978. Mesozoic construction of the Cordilleran "collage," central British Columbia to central California. In Howell, D. G., and McDougall, K. A. (eds.), *Mesozoic Paleogeography of the Western United States*. Los Angeles: Society of Economic Paleontologists and Mineralogists. Pacific Coast Paleogeography Symposium 2, Pacific Section, pp. 1–32.

Derer, C. E., Schumacher, M. E., and Schäfer, A., 2005. The Upper Rhine Graben: basin geometry and early syn-rift tectonosedimentary evolution. *International Journal of Earth Sciences (Geologische Rundschau)*, **94**, 640–656.

Dewey, J. F., 1982. Plate tectonics and the evolution of the British Isles. *Journal of the Geological Society of London*, **139**, 371–412.

Dewey, J. F., 2002. Transtension in arcs and orogens. *International Geology Review (George A. Thompson Symposium volume)*, **44**, 402–439.

Dickinson, W. R., 2002. The basin and range province as a composite extensional domain. *International Geology Review (George A. Thompson Symposium volume)*, **44**, 1–38.

Durand, L., Jolivet, F., Horváth, F., and Séranne, M. (eds.), 1999. *The Mediterranean basins: Tertiary extension within the Alpine Orogen*. Geological Society special publication 156, 570 pp.

Einsele, G., 2000. *Sedimentary Basins – Evolution, Facies and Sediment Budget*. Berlin: Springer, Vol. 2 (completely revised).

Evans, D., Graham, C., Armour, A., and Bathurst, P., 2003. *The Millenium Atlas: Petroleum Geology of the Central and Northern North Sea*. London: The Geological Society of London.

Eyidogan, H., and Jackson, J., 1985. Seismological study of normal faulting in the Demirci, Alasehir and Gediz earthquakes of 1969–70 in western Turkey: Implications for the nature and geometry of deformation in the continental crust. *Geophysical Journal of the Royal Astronomical Society*, **81**, 569–607.

Faulds, J. E., and Stewart, J. H. (eds.), 1998. *Accommodation zones and transfer zones: the regional segmentation of the Basin and Range Province*. Geological Society of America special paper 323, vii + 257 pp. + 1 folded plate in pocket.

Felton, A. A., Russell, J. M., Cohen, A. S., Baker, M. E., Chesley, J. T., Lezzar, K. E., McGlue, M. M., Pigati, J. S., Quade, J., Curt Stager, J., and Tiercelin, J. J., 2007. Paleolimnological evidence for the onset and termination of glacial aridity from Lake Tanganyika Tropical East Africa. *Palaeogeography Palaeoclimatology Palaeoecology*, **252**, 405–423, doi:10.1016/j.palaeo.2007.04.003.

Frostick, L. E., 1997. The East African rift basins. In Selley, R. C. (ed.), *African Basins*. Amsterdam: Elsevier, pp. 187–209.

Frostick, L. E., Renaut, R. W., Reid, I., and Tiercelin, J. J. (eds.), 1986. Sedimentation in the African rifts. Geological Society special publication 25, 382 pp.

Gans, P. B., 1987. An open-system, two-layer crustal stretching model for the eastern Great Basin. *Tectonics*, **6**, 1–12.

Graham, S. A., Brassell, S., Carroll, A. R., Xiao, X., Demaison, G., McKnight, C. L., Liang, Y., Chu, J., and Hendrix, M. S., 1990. Characteristics of selected petroleum source rocks Xianjiang Uygur autonomous region, Northwest China. *American Association of Petroleum Geologists Bulletin*, **74**, 493–512.

Gregory, J. W., 1894. Contributions to the physical geography of British East Africa. *The Geographical Journal*, **4**, 289–315.

Harding, T. P., 1983. Graben hydrocarbon plays and structural styles. *Geologie en Mijnbouw*, **62**, 3–23.
Hüttner, R., 1991. Bau und Entwicklung des Oberrheingrabens - Ein Überblick mit historischer Rückschau. *Geologisches Jahrbuch*, **E48**, 17–42.
Ingersoll, R. V., 2001. Structural and stratigraphic evolution of the Rio Grande Rift, northern New Mexico and southern Colorado. *International Geology Review*, **43**, 867–891.
Jackson, J. A., 1987. Active continental deformation and metamorphism. *Philosophical Transactions of the Royal Society of London*, **A321**, 47–66.
Jackson, J., and Belkinsop, T., 1993. The Malawi earthquake of 10 March 1989: deep faulting within the east African rift system. *Tectonics*, **12**(5), 1131–1139.
Jaffé, F. C., 1971. Geothermal energy: a review. *Bulletin der Vereinigung Schweizerischer Petroleum-Geologen und - Ingenieure*, **38**, 17–40.
Kampunzu, A. B., and Lubala, R. T. (eds.), 1991. *Magmatism in Extensional Structural Setting – The Phanerozoic African Plate*. Berlin: Springer.
Kendall, J.-M., Stuart, G. W., Ebinger, C. J., Bastow, I. D., and Keir, D., 2005. Magma-assisted rifting in Ethiopia. *Nature*, **433**, 146–148.
Kinnaird, J. A. (ed.), 1998. Aspects of tensional magmatism. *Journal of African Earth Sciences*, **26**, 1–150.
Kravchinsky, V. A., Krainov, M. A., Evans, M. E., Peck, J. A., King, J. W., Kuzmin, M. I., Sakai, H., Kawai, T., and Williams, D. F., 2003. Magnetic record of Lake Baikal sediments: chronological and paleoclimatic implication for the last 6.7 Myr. *Palaeogeography Palaeoclimatology Palaeoecology*, **195**, 281–293.
Kuz'min, M. I., Karabanov, E. B., Kawai, T., Williams, D., Bychinsky, V. A., Kerber, E. V., Kravchinsky, V. A., Bezrukova, E. V., Prokopenko, A. A., Geletii, V. F., Kalmychkov, G. V., Goreglyad, A. V., Antipin, V. S., Khomutova, M. Y., Soshina, N. M., Ivanov, E. V., Khrusevich, G. K., Tkachenko, L. L., Solotchina, E. P., Ioshida, N., and Gvozdkov, A. N., 2001. Deep drilling on Lake Baikal: main results. *Russian Geology and Geophysics*, **42**, 3–28.
Lambiase, J. J. (ed.), 1995. *Hydrocarbon habitat in rift basins*. Geological Society special publication 80, 381 pp.
Landon, S. M. (ed.), 1994. *Interior rift basins*. American Association of Petroleum Geologists memoir 59, 276 pp.
Le Pichon, X., and Sibuet, J. C., 1981. Passive margins: a model of formation. *Journal of Geophysical Research*, **86**, 3708–3720.
Leeder, M. R., 1995. Continental rifts and proto-oceanic rift troughs. In Busby, C. J., and Ingersoll, R. V. (eds.), *Tectonics of Sedimentary Basins*. Oxford: Blackwell, pp. 119–148.
Lister, G. S., and Davis, G. A., 1989. The origin of metamorphic core complexes and detachment faults formed during Tertiary continental extension in the northern Colorado River region. U.S.A. *Journal of Structural Geology*, **11**, 65–94.
Littke, R., Bayer, U., Gajewski, D., and Nelskamp, S., 2008. *Dynamics of Complex Intracontinental Basins – The Central European Basin System*. Berlin: Springer.
Lorenz, J. C., 1988. *Triassic-Jurassic Rift-Basin Sedimentology – History and Methods*. New York: Van Nostrand Reinhold.
MacKenzie, A. S., and McKenzie, D., 1983. Isomerization and aromatization of hydrocarbons in sedimentary basins formed by extension. *Geological Magazine*, **120**, 417–470.
Manspeizer, W. (ed.), 1988. *Triassic-Jurassic Rifting – Continental Breakup and the Origin of the Atlantic Ocean and Passive Margins*. Amsterdam: Elsevier, Vol. 2.
Manspeizer, W., and Olsen, P. E., 1981. Rift basins of the passive margin: tectonics, organic-rich lacustrine sediments, basin analysis. In Hobbs, G. W. (ed.), *Field Guide to the Geology of the Palaeozoic, Mesozoic, and Tertiary Rocks of New Jersey and the Central Hudson Valley*. New York: Petroleum Exploration Society of New York, pp. 25–103.
McKenzie, D., 1978. Some remarks on the development of sedimentary basins. *Earth and Planetary Sscience Letters*, **40**, 25–32.
McQuarrie, N., and Wernicke, B. P., 2005. An animated tectonic reconstruction of southwestern North America since 36 MA. *Geosphere*, **1**, 147–172, doi:10.1130/GES00016.1.
Miao, J. Y., Kou, H. S., Zhou, L. F., and Han, Z. Y., 2006. Sedimentary environments of organic matter from Middle Permian source rocks in northern Xinjiang China. *Chinese Journal of Geochemistry*, **25**, 258–265.
Miller, J. M. G., and John, B. E., 1988. Detached strata in a Tertiary low-angle normal fault terrane, southeastern California: a sedimentary record of unroofing, breaching, and continued slip. *Geology*, **16**, 645–648.
Morley, C. K., 1999. *Geoscience of Rift Systems – Evolution of East Africa*. AAPG studies in geology 44. Tulsa: The American Association of Petroleum Geologists, 242 pp. + 5 Appendices + 16 pp. Index.
Olsen, P. E., and Kent, D. V., 1999. Long-period Milankovich cycles from late Triassic and early Jurassic of eastern North America and their implications for the calibration of the early Mesozoic time-scale and the long-term behaviour of the planets. *Philosophical Transactions of the Royal Society of London*, **A357**, 1761–1786.
Olsen, P. E., and Schlische, R. W., 1990. Transtensional arm of the early Mesozoic Fundy rift basin: penecontemporaneous faulting and sedimentation. *Geology*, **18**, 695–698.
St Onge, M. R., and King, J. E., 1987. Evolution of regional metamorphism during back-arc stretching and subsequent crustal shortening in the 1.9. Ga Wopmay Orogen, Canada. *Philosophical Transactions of the Royal Society of London*, **A321**, 199–218.
Quennell, A. M. (ed.), 1985. *Continental Rifts*. New York: Van Nostrand Reinhold. Benchmark Papers in Gelogy Series.
Quennell, A. M. (ed.), 1982. *Rift Valleys Afro-Arabian*. Benchmark papers in geology 60. Stroudsburg: Hutchison Ross.
Richardson-Bunbury, J. M., 1996. The Kula volcanic field, western Turkey: the development of a Holocene alkali basalt province and the adjacent normal-faulting graben. *Geological Magazine*, **133**, 275–283.
Ring, U., and Wernicke, B. (eds.), 2009. *Extending a continent: architecture, rheology and heat budget*. Geological Society special publication 321, 272 pp.
Rotstein, Y., Edel, J.-B., Gabriel, G., Boulanger, D., Schaming, M., and Munschy, M., 2006. Insight into the structure of the Upper Rhine Graben and its basement from a new compilation of Bouguer Gravity. *Tectonophysics*, **425**, 55–70.
Sawkins, F. J., 1990. *Metal Deposits in Relation to Plate Tectonics*. Berlin: Springer.
Schlüter, T., 1997. *Geology of East Africa*, with contributions by Craig Hampton. Beiträge zur Regionalen Geologe der Erde 27. Berlin: Gebrüder Borntraeger.
Schumacher, M. E., 2002. Upper Rhine Graben: role of preexisting structures during rift evolution. *Tectonics*, **21**, 1006–1022, doi:10.1029/2001TC900022.
Şengör, A. M. C., 1995. Sedimentation and tectonics of fossil rifts. In Busby, C. J., and Ingersoll, R. V. (eds.), *Tectonics of Sedimentary Basins*. Oxford: Blackwell, pp. 53–117.
Şengör, A. M. C., 1987. Cross-faults and differential stretching of hangingwalls in regions of low-angle normal faulting: examples form western Turkey. In Coward, M. P., Dewey, J. F., and Hancock, P. L. (eds.), *Continental Extensional Tectonics*. Geological Society special publication 321 (Albert M. Quennell volume), pp. 575–589.
Şengör, A. M. C., 2001. Elevation as indicator of mantle plume activity. In Ernst, R., and Buchan, K. (eds.), Geological Society of America special paper 352, pp. 183–225.

Şengör, A. M. C., and Natal'in, B. A., 2001. Rifts of the world. In Ernst, R., and Buchan, K. (eds.), Geological Society of America special paper 352, pp. 389–482.
Şengör, A. M. C., and Burke, K., 1978. Relative timing of rifting and volcanism on Earth and its tectonic implications. *Geophysical Research Letters*, **5**, 419–421.
Smith, A. G., 1976. Orogeny: a review. *Tectonophysics*, **33**, 215–285.
Snow, J. K., and Wernicke, B., 2000. Cenozoic tectonism in the Central Basin and Range: magnitude, rate and distribution of upper crustal strain. *American Journal of Science*, **300**, 659–719.
Spizaharsky, T. N., and Borovikov, L. I., 1966. Tectonic map of the Soviet Union on a scale of 1: 2 500 00. In *Scientific Communications Read to the Commission for the Geological Map of the World*. 22nd International Geological Congress, Delhi, pp. 111–120
Surkov, V. S., Smirnov, L. V., and Zhero, O. G., 1994. Early Mesozoic rifting and evolution of the West Siberian Basin. In Roure, F., Elluz, N., Shein, V. S., and Skvortsov, I. (eds.), *Geodynamic Evolution of Sedimentary Basins*. International Symposium, Moscow, Paris, Éditions Technip, pp. 135–143.
ten Brink, U. S., and Taylor, M. H., 2002. Crustal structure of central Lake Baikal: insights into intracontinental rifting. *Journal of Geophysical Research*, **107**, ETG-2-1–ETG-2-15, doi:10.1029/2001JB000300.
Ulmishek, G. F., Bogino, V. A., Keller, M. B., and Poznyakevich, Z. L., 1994. Structure, stratigraphy, and petroleum geology of the Pripyat and Dnieper-Donets Basins, Byelarus and Ukraine. In Landon, S. M. (ed.), *Interior Rift Basins*. American Association of Petroleum Geologists memoir 59, pp. 125–156.
Ulrych, J., Cajz, V., and Adamovič, J. (eds.), 1999. Magmatism and rift basin evolution. *GeoLines*, **9**, 1–135.
Verdel, C., Wernicke, B. P., Ramezani, J., Hassanzadeh, Renne, P. R., and Spell, T. L., 2007. Geology and thermochronology of tertiary Cordilleran-style metamorphic core complexes in the Saghand region of central Iran. *Geological Society of America Bulletin*, **119**, 961–977.
Wernicke, B., 2009. The detachment era (1977–1982) and its role in revolutionizing continental tectonics. In Ring, U., and Wernicke, B. (eds.), Geological Society special publication 321, pp. 1–8.
Wernicke, B. (ed.), 1990. *Basin and range extensional tectonics near the latitude of Las Vegas, Nevada*. Geological Society of America memoir 176, xii + 511 pp. + numerous separate plates.
Wernicke, B., and Burchfiel, B. C., 1982. Modes of extensional tectonics. *Journal of Structural Geology*, **4**, 105–111.
Wiart, P., and Oppenheimer, C., 2004. Large magnitude silicic volcanism in north Afar: the Nabro volcanic range and Ma'alalta volcano. *Bulletin of Volcanology*, **67**, 99–115.
Wickham, S., and Oxburgh, E. R., 1985. Continental rifts as a setting for regional metamorphism. *Nature*, **318**, 330–333.
Wilson, M., Neumann, E.-R., Davies, G. R., Timmermann, M. J., Heremans, M., and Larsen, B. T. (eds.), 2004. *Permo-Carboniferous magmatism and rifting in Europe*. Geological Society special publication 223, 498 pp.
Woodcock, N. H., 1986. The role of strike-slip fault systems at plate boundaries. *Philosophical Transactions of the Royal Society of London*, **A317**, 13–29.
Yirgou, G., Ebinger, C. J., and Maguire, P. K. H. (eds.), 2006. *The Afar volcanic province within the East African rift system*. Geological Society special publication 259, 331 pp.
Ziegler, P. A. (ed.), 1992. *Geodynamics of Rifting*. Amsterdam: Elsevier.
Ziegler, P. A., 1994a. Hydrocarbon habitat in rift basins. In Roure, F., Elluz, N., Shein, V. S., and Skvortsov, I. (eds.), *Geodynamic Evolution of Sedimentary Basins*. International Symposium, Moscow, Paris, Éditions Technip, pp. 85–94.
Ziegler, P. A., 1994b. Geodynamic processes governing development of rift basins. In Roure, F., Elluz, N., Shein, V. S., and Skvortsov, I. (eds.), *Geodynamic Evolution of Sedimentary Basins*. International Symposium, Moscow, Paris, Éditions Technip, pp. 19–67.

Cross-references

Earth, Density Distribution
Earthquake, Focal Mechanism
Earthquake, Location Techniques
Earthquakes and Crustal Deformation
Geodynamics
Geoid
Geothermal Heat Pumps
Isostasy
Isostasy, Thermal
Lithosphere, Continental
Lithosphere, Mechanical Properties
Mantle Convection
Mantle Plumes
Plate Motions in Time: Inferences on Driving and Resisting Forces
Plates and Paleoreconstructions
Radiogenic Heat Production of Rocks
Seafloor Spreading
Sedimentary Basins
Seismicity, Intraplate

CORE DYNAMO

Ulrich R. Christensen
Max-Planck Institut für Sonnensystemforschung, Katlenburg-Lindau, Germany

Synonyms

Geodynamo

Definition

Dynamo. Process for generating electrical current and magnetic field by electromagnetic induction in a moving conducting medium.
Geodynamo. Dynamo process in the fluid outer core that generates Earth's main magnetic field.

Introduction

It has been firmly established that the geomagnetic field must be generated by a magnetohydrodynamic dynamo operating in the Earth's outer core. Thermal and compositional buoyancy forces drive a convective circulation of the liquid iron alloy. Assuming that a magnetic field is present, electrical currents are induced in the moving fluid. When the magnetic field associated with these currents has the strength and geometry that is suitable for the induction process and no external source for the field is required, this is called a self-sustained dynamo. The first approximation of the Earth's core is a sphere with uniform electrical conductivity, in contrast to technical dynamos, where the currents are guided by a highly inhomogeneous distribution of electrical conductors. In the former case, we speak of a homogeneous dynamo. From a theoretical point of view, homogeneous dynamos are more difficult to understand.

Simple motions, such as differential rotation (as in an electrical generator), are unable to drive a homogeneous dynamo, and flow patterns of a certain complexity are required. Until late into the twentieth century, dynamo theory has been concerned mainly with the conceptual understanding of how, in principle, a magnetic field can be generated in such an environment. Starting with models by Glatzmaier and Roberts (1995), Kageyama and Sato (1995) and Kuang and Bloxham (1997), realistic self-consistent numerical simulations of the geodynamo became available and have been successful in reproducing many of the observed properties of the geomagnetic field. The more fundamental aspects of the geodynamo are discussed elsewhere (see *Geomagnetic Field, Theory*). Here, the progress in understanding the geodynamo based on numerical modeling and comparing its results with specific properties of the geomagnetic field is addressed.

Dynamo model concept and equations

Model setup

In contrast to earlier kinematic dynamo models, where the flow is prescribed, modern geodynamo models aim at a fully self-consistent treatment of fluid flow and magnetic field generation in the Earth's outer core. There are some basic requirements for a realistic model: (1) The mechanism for driving flow by thermal or compositional buoyancy must be part of the model. (2) Because an axisymmetric field cannot be generated by a dynamo (Cowling's theorem), the model must be fully three-dimensional. (3) The model must be rotating because Coriolis forces are important to generate a flow pattern that is conducive for the dynamo process. The basic setup of geodynamo models is that of a rotating spherical shell of outer radius r_o and inner radius r_i, filled with a fluid of uniform conductivity, which represents Earth's outer core (Figure 1). For this system, the coupled equations for convection-driven flow and electromagnetic induction are solved. A detailed account on fundamental aspects of convection in rotating spheres is given in Jones (2007), and modeling aspects and the commonly employed numerical schemes are discussed in Christensen and Wicht (2007).

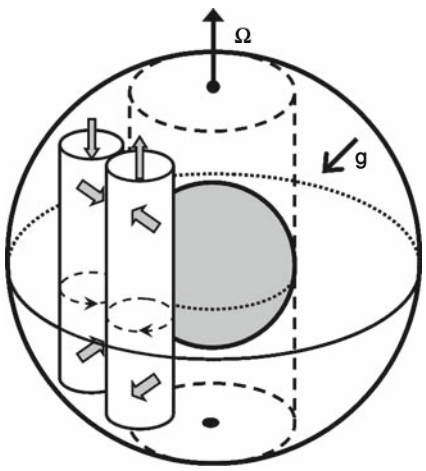

Core Dynamo, Figure 1 Columnar convection in a rotating spherical shell. The inner core tangent cylinder is shown by broken lines. Under Earth's core conditions, the columns would be thinner and more numerous. (From Christensen, 2010b, Copyright: Cambridge University Press.)

Dynamo equations

The relevant magnetohydrodynamic equations are usually written in non-dimensional form. A possible scheme for scaling the equations is to use the shell thickness $D = r_o - r_i$ as length scale, the viscous diffusion time D^2/ν as timescale (ν is kinematic viscosity), $(\rho\Omega/\sigma)^{1/2}$ for the scale of the magnetic field $\mathbf{B}$ and the imposed temperature contrast ΔT between inner and outer boundary for temperature T (ρ is density, σ electrical conductivity and Ω rotation rate). The Navier–Stokes equation for the velocity $\mathbf{u}$, augmented by rotational and electromagnetic forces, is

$$E\left(\frac{\partial \mathbf{u}}{\partial t} + \mathbf{u}\cdot\nabla\mathbf{u}\right) + 2\hat{\mathbf{z}}\times\mathbf{u} + \nabla\Pi = E\nabla^2\mathbf{u} + \frac{Ra\,E}{Pr}\frac{\mathbf{r}}{r_o}T + \frac{1}{Pm}(\nabla\times\mathbf{B})\times\mathbf{B}. \quad (1)$$

The terms on the left-hand side describe in order the inertial force, the Coriolis force (with $\hat{\mathbf{z}}$ the unit vector parallel to the rotation axis) and the gradient of the non-hydrostatic pressure Π. The terms on the right-hand side stand for viscous friction, thermal buoyancy forces and the Lorentz force.

The magnetic induction equation, obtained from Maxwell's equations and Ohm's law for a moving incompressible conductor, is

$$\frac{\partial \mathbf{B}}{\partial t} + (\mathbf{u}\cdot\nabla)\mathbf{B} = (\mathbf{B}\cdot\nabla)\mathbf{u} + \frac{1}{Pm}\nabla^2\mathbf{B}, \quad (2)$$

where the second term on the LHS describes magnetic field advection and the terms on the RHS magnetic field generation and diffusion, respectively. Magnetic diffusion is a consequence of the ohmic resistance that damps the electrical currents associated with the magnetic field.

The advection–diffusion equation for temperature is

$$\frac{\partial T}{\partial t} + \mathbf{u}\cdot\nabla T = \frac{1}{Pr}\nabla^2 T + \varepsilon, \quad (3)$$

with a heat source term ε on the RHS. For compositional convection, an equivalent equation holds where the concentration of light components replaces temperature. The set of equations is completed by the condition of incompressibility, which seems to be justified for Earth's core where density differences are moderate, and the condition that $\mathbf{B}$ is solenoidal:

$$\nabla\cdot\mathbf{u} = 0, \quad \nabla\cdot\mathbf{B} = 0. \quad (4)$$

The equations are complemented by boundary conditions for the velocity, usually $\mathbf{u} = 0$, fixed temperature or fixed heat flux at r_o and r_i, and a continuity condition for the magnetic field at r_o that links the field in the dynamo with an external potential field that decays with radius. Simple models assume the inner core to be insulating, but in many cases it is taken as an electrical conductor with the same conductivity as in the outer core. It has been suggested that the finite conductivity of the inner core plays an important role for preventing frequent dipole reversals of the geodynamo, because a dipole reversal can only be completed successfully if the new polarity persists for the timescale of diffusive dipole decay in the inner core, $r_i^2/(\pi^2\lambda)$, which is several thousand years. However, this is contested by dynamo models that show little differences between simulations with a conducting or an insulating inner core.

Parameters

The four non-dimensional control parameters in these equations are defined in Table 1. In dynamo models, the values of most of these parameters fall short of their extreme values in the Earth's core. For practical reasons, it is not possible to resolve the very small spatial structures that occur at realistic parameter values. The *Rayleigh number Ra* describes the ratio between buoyancy driving convection and retarding effects. In the core, it is much larger than the critical value for the onset of convection, Ra_c, while models are more moderately supercritical (Table 1). The discrepancy is by ten orders of magnitude for the *Ekman number E*, the ratio of viscous forces to Coriolis forces. The very small core value of E indicates that viscous forces are negligible, except in very thin Ekman layers at the boundaries to the solid mantle and inner core. The *magnetic Prandtl number Pm*, the ratio of viscosity to magnetic diffusivity, is very small for liquid metals, but must be set to a value of order one to obtain a self-sustained dynamo in present models. Only the (hydrodynamic) *Prandtl number Pr*, the ratio of viscosity to thermal diffusivity, is of order one in the core and in dynamo models. In terms of physical parameters, the viscosity and the thermal diffusivity are far too large in the models and, in most cases, the rotation rate is too small.

Several dimensionless diagnostic numbers can be formed with the characteristic flow velocity U and magnetic field strength B in the dynamo (Table 1). The velocity in Earth's core can be estimated from the geomagnetic secular variation under the assumption that the magnetic flux at the core surface is approximately frozen into the moving fluid (Alfvén's theorem), which is the case when the diffusion term in Equation 2 can be neglected. In this case, the variation of the radial magnetic field component B_r at the core-mantle boundary can be written

$$\partial B_r/\partial t + \nabla_h \cdot (\mathbf{u} B_r) = 0. \tag{5}$$

where the suffix h indicates the horizontal part of the divergence operator. Additional assumptions are needed to infer the velocity at the top of the core (below the Ekman layer) from the observed B_r and its time derivative, but the flow pattern obtained from these inversions are broadly similar and the characteristic velocity is approximately 0.5 mm/s (Holme, 2007). The characteristic field strength inside Earth's core is probably in the range 1–4 mT, as will be discussed further below.

The most important diagnostic number is the *magnetic Reynolds number Rm*, which describes the ratio of magnetic advection and induction to magnetic diffusion. In order for induction effects in a dynamo to overcome the diffusive dissipation of magnetic field, it is expected that *Rm* must be larger than one. Practically, it turns out that self-sustained magnetic field generation occurs in geodynamo models when *Rm* exceeds approximately 40. Using $U \approx 0.5$ mm/s, the magnetic Reynolds number is of order 1,000, safely above the critical limit. Also, $Rm \gg 1$ is a condition for Equation 5 to apply. Still, the value of *Rm* in the Earth's core is moderate and can be handled in direct numerical simulations. This contrasts with the much larger values of *Rm* in other cosmic dynamos, which requires that magnetic induction and diffusion

Core Dynamo, Table 1 Dynamo parameters. α thermal expansivity, g_o gravity at core surface, ΔT superadiabatic temperature contrast across core, κ thermal diffusivity, ν kinematic viscosity, Ω rotation rate, D outer core thickness, $\lambda = 1/(\mu_o\sigma)$ magnetic diffusivity, U characteristic flow velocity, B characteristic magnetic field strength, μ_o magnetic permeability, ρ density

	Control parameters			
	Rayleigh number	Ekman number	Magn. Prandtl number	Prandtl number
Definition	$Ra = \alpha g_o \Delta T D^3/(\kappa\nu)$	$E = \nu/(\Omega D^2)$	$Pm = \nu/\lambda$	$Pr = \nu/\kappa$
Core	$10^4 Ra_c$	10^{-15}–10^{-14}	10^{-6}–10^{-5}	0.1–1
Models	(1–100) Ra_c	10^{-6}–10^{-2}	0.1–10	1
	Diagnostic numbers			
	Magn. Reynolds no.	Reynolds no.	Rossby no.	Elsasser no.
Definition	$Rm = UD/\lambda$	$Re = UD/\nu$	$Ro = U/(\Omega D)$	$\Lambda = B^2/(2\mu_o\lambda\rho\Omega)$
Core	10^3	10^9	10^{-7}	0.1–10
Models	40–2,000	<2,000	10^{-2}–10^{-4}	1–100

effects at small unresolved scales are parameterized by applying concepts of the mean-field dynamo theory. The ability to solve for magnetic induction and diffusion in Earth's core directly without parameterizations is probably the main reason for the success of geodynamo models.

The (hydrodynamic) *Reynolds number Re* is much smaller in the models than it is in the core where it is of the order 10^9, indicating a highly turbulent regime. Consequently, dynamo models miss the small eddies that are expected to exist in the core. Viscosity kicks in only at length scales of some meters to suppress even smaller structures in the flow. However, the small eddies are unimportant for the magnetic induction process, because the magnetic diffusivity, which is $Pm^{-1} = 10^6$ times larger than the kinematic viscosity, homogenizes the magnetic field at scales of less than several tens of kilometers.

The *Elsasser number* Λ describes the ratio of Lorentz forces to Coriolis forces. In the Earth's core, both forces are assumed to be of leading order. A balance in Equation 1 that is dominated by these two forces (plus the pressure gradient force) is called a magnetostrophic balance. The magnetostrophic state is often associated with an Elsasser number of order one. Many present dynamo models match this value of Λ.

The *Rossby number Ro* describes the ratio of inertial forces to the Coriolis force and is very small in the core. In models, it is less than one, although larger than the core value. Instead of forming the Rossby number with the global length scale D, a more appropriate measure for the ratio of the two forces is obtained by using the characteristic length scale ℓ of the flow (local Rossby number Ro_ℓ). The value of Ro_ℓ is difficult to estimate for the core, but model values and the Earth value may be in better agreement than they are for *Ro*.

Energetics of the geodynamo

Although the decay of radioactive isotopes in the core may contribute to some degree to the core heat flux, most of the buoyancy that drives convection in the outer core is associated with secular cooling. The sluggish convection in the mantle controls the heat flux through the core-mantle boundary in terms of its magnitude and its spatial distribution, which is expected to be rather heterogeneous. Recent estimates put the heat flow at the core-mantle boundary into the range of 5–15 TW (Lay et al., 2008). For thermal convection to occur, the temperature gradient must reach or exceed the adiabatic gradient. Because iron is a comparatively good conductor, 3–8 TW can be transported by thermal conduction along an adiabatic gradient. This fraction of the heat flux is lost for driving the dynamo. For values of the heat flux near the low end of estimates and of the potential conductive flux near the upper end, a stable thermal stratification at the top of the core could exist. A consequence of core cooling is the slow growth of the solid inner core by freezing iron on its outer boundary. The associated latent heat release balances roughly one half of the heat loss from the core and renders the deep fluid core thermally unstable even if the top layer is not. The relative depletion of light alloying elements in the solid core is balanced by an enrichment in the residual fluid above the growing inner core, which drives compositional convection. Estimates for the work done by thermal and compositional buoyancy forces are of the order $W \approx 1$ TW (Nimmo, 2007). Compositional buoyancy contributes roughly two thirds to it. This energy flux is available to generate magnetic field and balance the associated ohmic dissipation. Viscous dissipation is usually assumed to play a minor role in the core.

Flow pattern and dynamo mechanism

The pattern of flow is strongly controlled by the Coriolis force. It is different for the regions inside and outside the *inner core tangent cylinder*. This is an imaginary cylinder aligned with the rotation axis and touching the inner core at the equator, which is shown by broken lines in Figure 1.

Flow outside tangent cylinder

Outside the tangent cylinder, the flow is organized in convection columns aligned with the vector of rotation, with the flow encircling the column axis (Figure 1). Superimposed is a circulation along the column axis that is directed towards the equatorial plane in columns with a cyclonic sense of rotation and away from the equator in anticyclonic columns. This results in helical flow, in which particles move on corkscrew-like trajectories. The helicity, $H = \mathbf{u} \cdot (\nabla \times \mathbf{u})$, is coherently negative in the northern hemisphere and positive in the southern hemisphere. Such helical flow is the basis for the α-effect, which can convert an axisymmetric toroidal field into an axisymmetric poloidal field, or vice versa, through intermediate steps involving non-axisymmetric small-scale fields (Moffatt, 1978). Because purely axisymmetric fields cannot be maintained by a dynamo, this mechanism plays an important role in the understanding of the dynamo process. The α-effect has been introduced in the context of mean-field dynamo theory, where it describes the induction effects of small unresolved flow scales. In geodynamo models and probably to some extent in the Earth's core, it is due to fairly large-scale convection columns (Busse, 1975). The models suggest that the axisymmetric toroidal field in the Earth's core (which is invisible from the outside) consists of a torus of westward-directed field north of the equatorial plane and eastward field south of the equatorial plane. The helical columnar flow converts this to a dipolar poloidal field whose field lines can leave the core (Figure 2). In some dynamo models, the toroidal magnetic field is regenerated by the same 'macroscopic α-effect from the poloidal magnetic field (α^2 dynamo, Olson et al., 1999). In other geodynamo models, the shearing of poloidal field lines by differential rotation, the Ω-effect, has been found to play an important role for toroidal field generation ($\alpha\Omega$-dynamo), but essentially all models confirm that the helical columnar convection produces the dipolar poloidal field component.

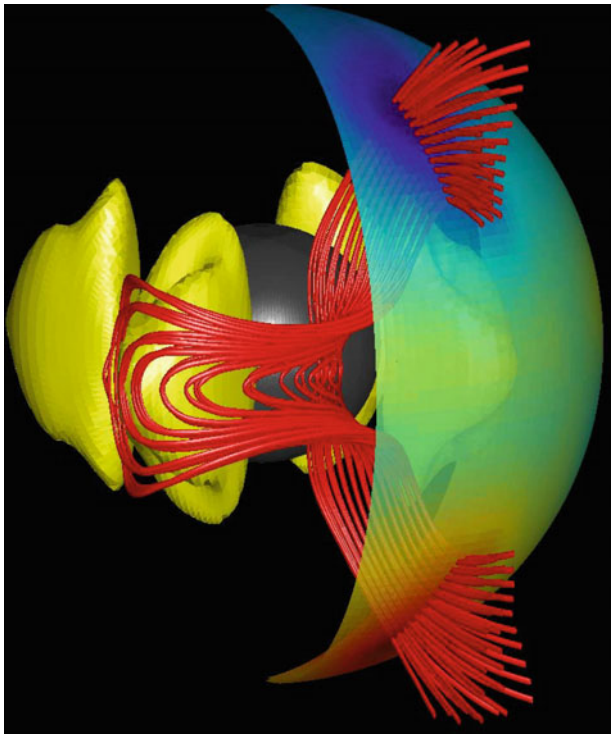

Core Dynamo, Figure 2 Bundle of magnetic field lines in a simple geodynamo model ($E = 10^{-3}$, Ra/Ra_c=1.8, Pm = 5, Pr = 1). The yellow blobs are anticyclonic vortices. Strong inward magnetic flux is shown in blue on the outer core boundary and outward flux in red. The NS-running part of the field lines represents poloidal magnetic field, and the EW-directed segments form the axisymmetric toroidal magnetic field, which consists of two bundles of opposite directions in the two hemispheres. The same field structure repeats periodically in longitude. (Courtesy of Julien Aubert.)

Although at low Ekman number and high Rayleigh number the simple columns give way to a more complex and turbulent pattern, the vortices are still elongated in the direction of the rotation axis and retain a coherent helicity in each hemisphere.

Strong concentrations of magnetic flux in the present geomagnetic field centered below North America and Sibera, which have counterparts at the same longitudes in the southern hemisphere, are interpreted as evidence for the presence of convection columns in the fluid core (Gubbins and Bloxham, 1987) (Figure 3a). The convergence at the core-mantle boundary associated with the equatorward flow in the axis of cyclonic columns (Figure 1) concentrates the poloidal magnetic field lines into these flux lobes, assuming that the frozen-flux assumption is approximately valid. In simple models, such as that in Figure 2, the fluxes lobes are associated with a single columnar vortex. Dynamo models at lower Ekman number and strongly supercritical Rayleigh number show similar high-latitude flux lobes in their magnetic fields when they are low-pass filtered to the resolution of the geomagnetic core field, roughly up to spherical harmonic degree 13 (e.g., Figure 3b). In this case, and probably in the Earth's core, the large-scale magnetic flux concentrations are due to the superposition of strong but complex and smaller-scale magnetic field structures, each associated with a separate convection column.

Flow inside tangent cylinder

In the polar regions inside the tangent cylinder, many dynamo models show an upwelling plume at or near the rotation axis. Because of the action of Coriolis forces, the plume is associated with an eastward vortex motion near the inner core and by a westward vortex motion near the core-mantle boundary, which is called a thermal wind circulation. A westward vortex motion in the polar cap region at the top of the core has also been inferred from the observed geomagnetic secular variation (Hulot et al., 2002). A polar plume is associated with flow that diverges away from the rotation axis below the core surface, which disperses poloidal magnetic field lines. This is seen in many geodynamo models (e.g., Figure 3b) and can explain the weak magnetic flux in the north polar region of the core (Figure 3a). It has been suggested that the solid inner core couples electromagnetically to the eastward vortex motion of the overlying fluid, which leads to a superrotation of the inner core with respect to the mantle and crust. While perfect coupling to the outer core flow would lead to superrotation rates in excess of a degree per year (Glatzmaier and Roberts, 1996), gravitational coupling between the inner core and the mantle can slow down the rate. Seismological evidence indicates a superrotation at a fraction of a degree per year.

Field properties

Field strength inside the core

How strong is the magnetic field inside Earth's core? Observations allow to constrain the strength of the poloidal field at the core-mantle boundary, which is presently 0.26 mT for the dipole field alone and 0.39 mT in spherical harmonic degrees from 1 to 13. It is not known how much the small unresolved length scale add to the field at the top of the core, but possibly they double this value. Inside the Earth's core, the poloidal field is expected to be stronger than at the outer boundary, and the toroidal component also contributes. Suggestions that the toroidal field, if generated by an intense Ω-effect, could be much stronger than the poloidal field are not supported by geodynamo simulations. In most of them, the magnetic energy is equipartitioned between the two field components. The dynamo models suggest that the characteristic field strength inside the dynamo is around 5–15 times the dipole field strength on the outer boundary, which puts it into the range of 1–4 mT.

The field strength inside Earth's core can be probed directly by the observation of torsional waves and oscillations. To the extent that viscous and inertial forces are negligible, the azimuthal Lorentz force integrated over the

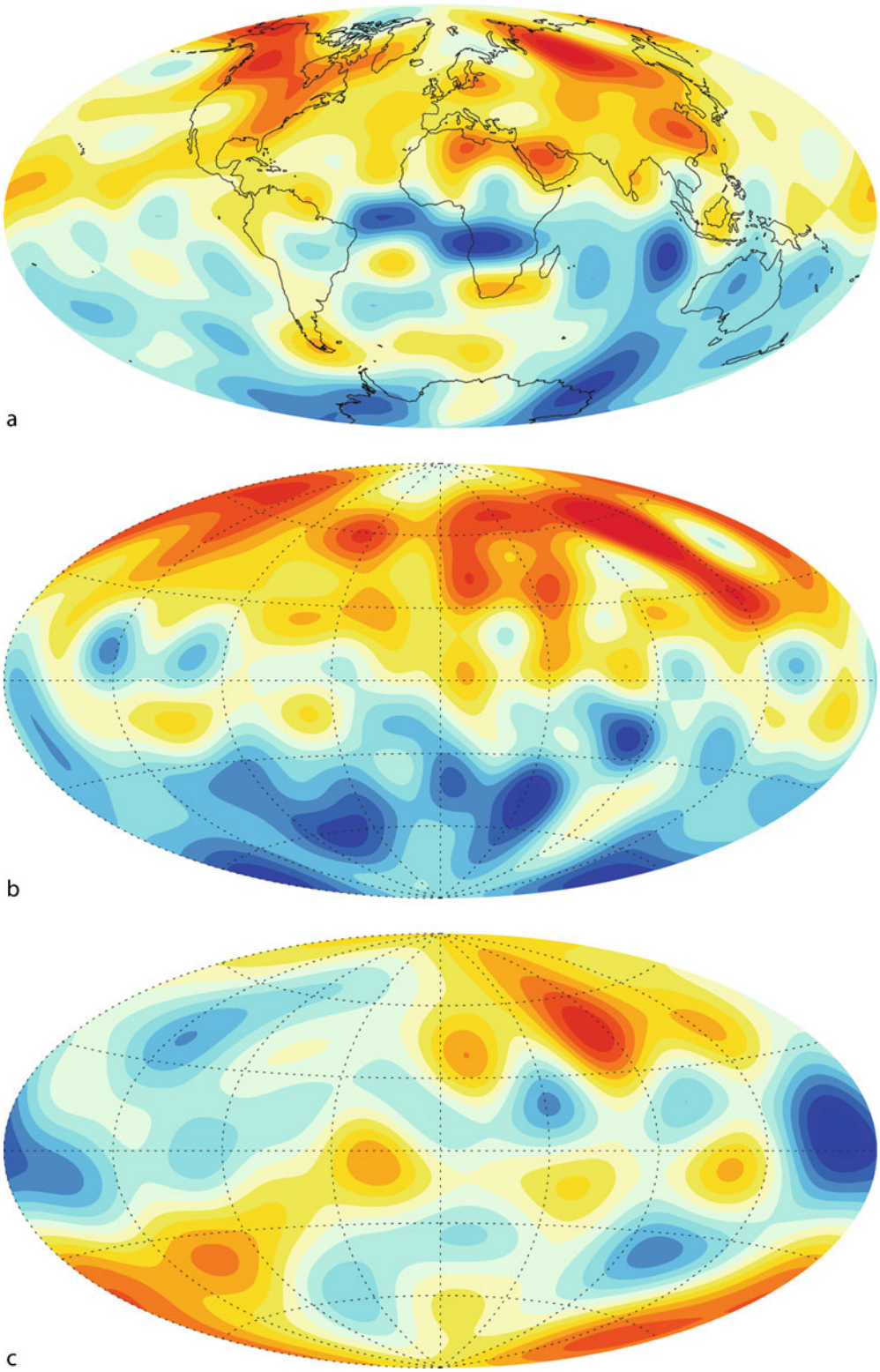

Core Dynamo, Figure 3 Radial magnetic field at the core-mantle boundary, *red* (*full lines*) inward and *blue* (*broken lines*) outward. (**a**) Geomagnetic field in 2010. (**b**) Dynamo model with dominant dipole contribution ($E = 10^{-5}$, $Pm = 0.8$, $Pr = 1$, $Ra/Ra_c = 114$). (**c**) Multipolar dynamo model ($E = 10^{-5}$, $Pm = 0.5$, $Pr = 1$, $Ra/Ra_c = 161$). The model magnetic fields are low-pass filtered to the resolution of the geomagnetic field.

surface of cylinders that are aligned with the rotation axis (geostrophic cylinders) must vanish in the so-called Taylor state. Perturbations of the Taylor state will results in torsional oscillations or torsional waves, consisting of an oscillatory differential rotation between the geostrophic cylinders. Magnetic field lines that permeate adjacent cylinders act like elastic strings and provide a restoring force when the cylinders are displaced relative to each other. The frequency of torsional eigenmodes and the wavespeed of traveling waves is directly related to the *rms* strength of the field component B_s in the cylindrically radial direction. The identification of torsional modes and waves in the secular variation data set is somewhat tentative, but is supported by a correlation between the inferred large-scale motion in the core and changes in the rotation rate of the solid part of the Earth (length-of-day changes) caused by angular momentum exchange between core and mantle (e.g., Holme, 2007). Torsional waves have led to estimates for the characteristic B_s-value ranging from 0.2 to 2 mT. Values near the upper end of this range for B_s agree with the dynamo model estimates for the total field assuming that the core field is statistically isotropic.

Scaling laws

An important question is what controls the magnetic field strength of the geodynamo and of planetary dynamos in general. It has been suggested that the magnitude of the internal core field is determined by a magnetostrophic force balance, meaning that the magnetic field inside Earth's core is driven towards a value that makes the Elsasser number (Table 1) to be of order one, i.e.,

$$B \propto (2\rho\Omega/\sigma)^{1/2}. \tag{6}$$

This results in $B \approx 2$ mT in good agreement with the above estimates. A different line of argument is based on the power available to balance ohmic dissipation. With some assumptions on how the length scale of the magnetic field in the core depends on the vigor of convection, this leads to

$$B \propto \mu_o^{1/2}\, \rho^{1/6}\, P^{1/3}, \tag{7}$$

where $P = W/(4\pi r_o^2)$ stands for the power per unit area of the core surface. With the current estimates for W Equation 7 results in a similar value of the field strength as the Elsasser number rule. However, the two scaling rules are radically different; in Equation 6, the field strength is independent of the energy flux, and in Equation 7, it does not depend on rotation rate or electrical conductivity. Sets of dynamo simulations that cover a substantial range in these properties, or their counterparts in terms of the non-dimensional control parameters, support the power-based scaling law (Equation 7). Furthermore, they show no significant dependence of the field strength on the viscosity. This may indicate that although current dynamo simulations are far too viscous (too high Ekman number), the viscosity is sufficiently low to not play a dominant role. However, testing this by further lowering the viscosity is desirable. The validity of the power-based scaling rule is also supported by the finding that it gives the right order of magnitude of the field strength for various convection-driven dynamos in rapidly rotating cosmic objects including Earth, Jupiter, and low-mass stars. A detailed discussion of dynamo scaling laws is given in Christensen (2010a).

Magnetic field geometry

While the rotation rate seems to have little influence on the field strength inside dynamo models, it probably controls the magnetic field morphology. In some geodynamo models, the magnetic field on the outer boundary resembles the Earth's field at the core-mantle boundary (Figure 3a and b) in terms of a dominant axial dipole and also of structures associated with multipole contributions. In other dynamo models, the dipole contribution is weak. In some cases, the field is dominated by the axial quadrupole or is restricted to one hemisphere, but in most cases it is irregular with contributions from a broad spectrum of multipole components without a pronounced dominance of a particular mode (Figure 3c). The selection of the field geometry was found to depend on the (local) Rossby number. At low values (rapid rotation and moderate flow velocities), dynamos are dipolar, whereas for high values (slower rotation and fast flow), they tend to be multipolar. In addition, boundary conditions and the mode of driving convection, i.e., either by secular cooling of the fluid core or by the latent heat and light element flux from the growing solid inner core, can play a role. The driving mode has changed over geological time. Before the Earth's inner core nucleated, which is estimated to have occurred about 0.5–1.5 Gyr ago (Nimmo, 2007), the dynamo has been driven by secular cooling alone, whereas thereafter the buoyancy source is mainly located at the inner core boundary. However, dynamo simulations for the different scenarios (Aubert et al., 2009) suggest that neither the geometry of the magnetic field nor its strength has changed very strongly. This is in accord with the lack of paleomagnetic evidence for drastic changes in the geomagnetic field since the Archean.

Secular variation

Timescales

The characteristic timescale of secular variation can be defined by the square root of the power of the magnetic field over the power in the time derivative of the field. This can be done separately for each harmonic degree n. The timescales decrease with increasing n. Aside from this scale dependence, the secular variation time has been found in dynamo models to vary with the inverse of the magnetic Reynolds number Rm, as would be expected if most of the secular variation is caused by the frozen-flux advection of magnetic field. Using the observed secular variation timescales to estimate the magnetic Reynolds number (or flow velocity) in the core gives essentially the same result, $Rm \approx 1,000$, as the more complex inversion of the secular variation for the core flow.

Advection versus diffusion of field

The westward drift of magnetic field structures is a long-standing issue. Some dynamo models show a persistent and global westward drift, whereas others do not. Over the past 400 years, magnetic field structures have systematically migrated westward in the Atlantic hemisphere, but not in the Pacific hemisphere, where the amplitude of secular variation is generally weaker. Dynamo models support the notion that such hemispherical dichotomy can be caused by coupling between the mantle and the core, in particular by the heterogeneity of the core heat flow caused by lower mantle thermal structure.

While much of the geomagnetic secular variation can be attributed to frozen-flux advection in a large-scale circulation, magnetic diffusion must play some role, in particular diffusion in the radial direction. It has been suggested that intense flux spots of both polarities, which are found in the geomagnetic field at low latitudes under Africa and the Atlantic (Figure 3a), have been formed by the expulsion of toroidal magnetic flux bundles through the core surface Bloxham (1986), somewhat analogous to the formation of sunspots. Because the toroidal field is confined to the core, the emergence of such spots necessarily involves diffusion, whereas their migration can be caused by frozen-flux advection. Some geodynamo simulations support such origin of equatorial flux spots. In these simulations, the columnar convection acts on a pair of toroidal flux bundles with opposite polarities and produces (anti) symmetric pairs of spots north and south of the equator. However, the geomagnetic low-latitude field pattern conforms at best marginally with this picture. An alternative explanation to the concept of field expulsion by convective columns and migration due to a large-scale westward flow is that, propagating hydromagnetic waves in the core create a periodic pattern of upwelling and downwelling that produces the belt of wave-train-like magnetic field structures in the low-latitude Atlantic hemisphere.

Magnetic field reversals

Several dynamo simulations show stochastic dipole reversals. Often the details resemble remarkably well what is known from the paleomagnetic record about geomagnetic reversals (e.g., Wicht et al., 2009). They are rather short events that interrupt long periods of stable polarity; both complete reversals and aborted reversals (excursions) occur; during a reversal the magnetic field is weak and not dipole dominated (Figure 4). Most model studies of reversal behavior have been performed with simple dynamo models at rather high values of the Ekman number, because long simulation times are needed to capture a fair number of these events. Reversing dipolar dynamos are typically found in a parameter regime between that of stable dipolar dynamos and of multipolar dynamos. Driving convection more strongly for otherwise identical conditions leads to very frequent and erratic dipole reversals that have little significance because the dipole is hardly ever dominating the magnetic field. Lowering the Prandtl number has the same effect, suggesting that strengthening the nonlinear inertial forces relative to the Coriolis force favors non-dipolar dynamo. Reducing the convective driving or increasing the Prandtl number results in strong dipolar fields that rarely or never reverse. In addition, boundary conditions

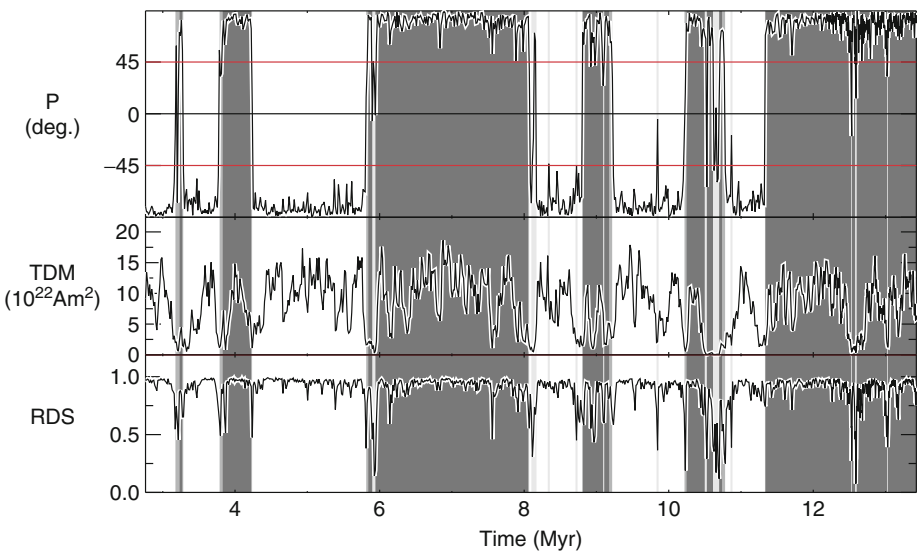

Core Dynamo, Figure 4 Time series of dipole tilt, true dipole moment (TRM) and relative dipole strength (RDS) from a numerical dynamo simulation. (Wicht, 2005, Copyright Blackwell.)

affect the reversal frequency. In particular, it has been shown that the pattern of heat flux at the core-mantle boundary, which is controlled by the thermal state of the lowermost mantle and varies on the long timescale of mantle convection, has a strong influence on the occurrence of reversals. This supports the assumption that the drastic secular change in the reversal rate over the past 200 Myr, which is observed in the paleomagnetic record, is caused by changes in the amplitude and pattern of core heat flow associated with a reorganization of mantle convection, such as formation and fading of superplumes. Although model studies have led to a number of suggestions concerning the cause for individual reversals, for example by the formation of strong new plumes in the core, so far no generally accepted concept for the reversal mechanism has emerged.

Summary

Helical convection columns outside the inner core tangent cylinder region play an essential role for our present understanding of the geodynamo. Theory and numerical simulations suggest that they are a fundamental element of the circulation in the outer core, and that they play a key role for the generation the Earth's dipole-dominated magnetic field. Certain details of the magnetic field structure at the core-mantle boundary are explained by such columns. Somewhat less certain, but supported by several lines of evidence, is the notion of rising plumes in the tangent cylinder near the rotation axis that are associated with weak magnetic field and westward vortex flow in the polar regions at the core-mantle boundary. However, much of our current understanding is based on numerical dynamo models that are far too viscous compared to the core. Although there is some evidence suggesting that this does not affect basic properties of the magnetic field, lowering the viscosity in dynamo models is important to test the robustness of our present results, even if models that use actual core values of the viscosity are out of reach. Modeling supports the notion that the magnetic field strength is controlled by the available power that drives the dynamo, not necessarily by a balance of Lorentz and Coriolis forces, as has been often assumed. Several dynamo models show dipole reversals that resemble, in many respects, geomagnetic reversals, but a full understanding of what causes reversals or controls the frequency of geomagnetic reversals is missing.

Bibliography

Aubert, J., Labrosse, S., and Poitou, C., 2009. Modelling the paleo-evolution of the geodynamo. *Geophysical Journal International*, **179**, 1414–1429.

Bloxham, J., 1986. The expulsion of magnetic flux from the Earth's core. *Philosophical Transactions of the Royal Society of London*, **87**, 669–678.

Busse, F. H., 1975. A model of the geodynamo. *Geophysical Journal of the Royal Astronomical Society*, **42**, 437–459.

Christensen, U. R., 2010a. Dynamo scaling laws: applications to the planets. *Space Science Reviews*, **152**, 565–590.

Christensen, U. R., 2010b. Planetary fields and dynamos. In Schrijver, C. J., and Siscoe, G. L. (eds.), *Heliophysics: Evolving Solar Activity and the Climates of Earth and Space*. Cambridge: Cambridge University Press.

Christensen, U. R., and Tilgner, A., 2004. Power requirement of the geodynamo from Ohmic losses in numerical and laboratory dynamos. *Nature*, **429**, 169–171.

Christensen, U. R., and Wicht, J., 2007. Numerical dynamo simulations. In Schubert, G. (ed.), *Treatise on Geophysics, Core Dynamics*. Amsterdam: Elsevier, Vol. 8, pp. 245–282.

Glatzmaier, G. A., and Roberts, P. H., 1995. A three-dimensional self-consistent computer simulation of a geomagnetic field reversal. *Nature*, **337**, 203–209.

Glatzmaier, G. A., and Roberts, P. H., 1996. Rotation and magnetism of Earth's inner core. *Science*, **274**, 1887–1891.

Gubbins, D., and Bloxham, J., 1987. Morphology of the geomagnetic field and implications for the geodynamo. *Nature*, **325**, 509–511.

Holme, R., 2007. Large-scale flow in the core. In Schubert, G. (ed.), *Treatise on Geophysics, Core Dynamics*. Amsterdam: Elsevier, Vol. 8, pp. 107–130.

Hulot, G., Eymin, C., Langlais, B., Mandea, M., and Olson, N., 2002. Small-scale structure of the geodynamo inferred From Oersted and Magsat Satellite data. *Nature*, **416**, 620–623.

Jones, C. A., 2007. Thermal and compositional convection in the outer core. In Schubert, G. (ed.), *Treatise on Geophysics, Core Dynamics*. Amsterdam: Elsevier, Vol. 8, pp. 131–185.

Kageyama, A., and Sato, T., 1995. Computer simulation of a magnetohydrodynamic dynamo II. *Physics of Plasmas*, **2**, 1421–1431.

Kuang, W., and Bloxham, J., 1997. An earth-like numerical dynamo model. *Nature*, **389**, 371–374.

Lay, T., Hernlund, J., and Buffett, B. A., 2008. Core mantle boundary heat flow. *Nature Geoscience*, **1**, 25–32.

Moffatt, H. K., 1978. *Magnetic Field Generation in Electrically Conducting Fluids*. Cambridge: Cambridge University Press.

Nimmo, F., 2007. Energetics of the core. In Schubert, G. (ed.), *Treatise on Geophysics, Core Dynamics*. Amsterdam: Elsevier, Vol. 8, pp. 31–65.

Olson, P., Christensen, U. R., and Glatzmaier, G. A., 1999. Numerical modeling of the geodynamo: mechanism of field generation and equilibration. *Journal of Geophysical Research*, **104**, 10383–10404.

Wicht, J., 2005. Palaeomagnetic interpretation of dynamo simulations. *Geophysical Journal International*, **162**, 371–380.

Wicht, J., Stellmach, S., and Harder, H., 2009. Numerical models of the geodynamo: from fundamental cartesian models to 3D simulations of field reversals. In Glassmeier, K. H., Soffel, H., and Negendank, J. F. W. (eds.), *Geomagnetic Field Variations*. Berlin: Springer, pp. 107–158.

Cross-references

Core-Mantle Coupling
Differential Rotation of the Earth's Inner Core
Earth's Structure, Core
Energy Budget of the Earth
Geomagnetic Excursions
Geomagnetic Field, Global Pattern
Geomagnetic Field, Polarity Reversals
Geomagnetic Field, Secular Variation
Geomagnetic Field, Theory
Paleomagnetic Field Intensity
Radioactivity in Earth's Core

CORE-MANTLE COUPLING

Paul H. Roberts[1], Jonathan M. Aurnou[2]
[1]Institute of Geophysics and Planetary Physics, University of California, Los Angeles, CA, USA
[2]Department of Earth and Space Sciences, University of California, Los Angeles, CA, USA

Definition, scope, and aims

The Earth is not a perfect timekeeper, and the spectrum of the variations in the mantle's angular velocity $\widehat{\mathbf{\Omega}}$ spans a wide range of frequencies. Of particular interest here are the comparatively large amplitude decadal and semi-decadal variations in which changes in length of day, P, of up to 2 ms occur. These would not be explained even if the global circulations of the atmosphere and oceans could be reversed. This is confirmed by a more detailed argument given in our recent review (Roberts and Aurnou, 2012), which will be referred to here as "RA12."

The origin of these length of day (LOD) variations must be sought in the Earth's core, and Figure 1 suggests that the task is not an easy one. Figure 1b shows dP/dt, derived by differentiating smoothed LOD data from the last half century, with atmospheric, oceanic, and tidal signals removed; semi-decadal time variations are clearly seen with a period τ_{LOD} of about 6 years (e.g., Abarca del Rio et al., 2000). Figure 1c shows the implied $\widehat{\Gamma}_z$ as a function of time t, where $\widehat{\Gamma}_z$ is the component parallel to the polar axis O_z of the torque $\widehat{\mathbf{\Gamma}}$ exerted by the core on the mantle. This shows that $\widehat{\Gamma}_z$ of nearly 10^{18} Nm is generated. We shall call this the "target torque" and seek its origin.

In addition, to the semi-decadal oscillations, larger variations seem to exist having longer periods, one of which is estimated to have a roughly 60 year period (e.g., Roberts et al., 2007). This time scale is reminiscent of the geomagnetic secular variation, and it is natural to seek

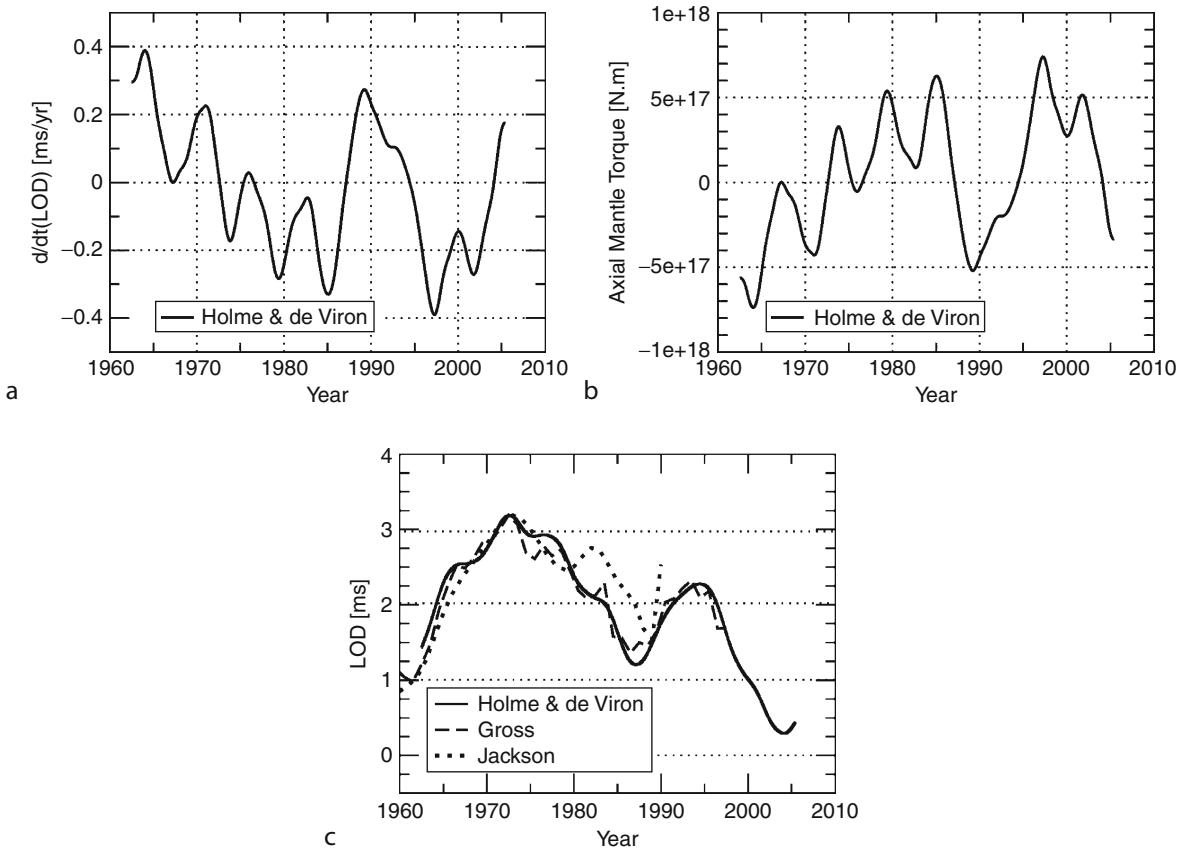

Core-Mantle Coupling, Figure 1 (**a**) LOD time series data from Holme and de Viron (2005) and Gross (2001) compared with LOD model from the "smooth" core flow inversion of Jackson (1997). The time series include the variation due to lunar tidal drag. (**b**) Temporal derivative, dP/dt, of the smoothed time series data of Holme and de Viron (2005), where P is the length of day. (**c**) The implied axial torque, $\widehat{\Gamma}_z = -(2\pi\widehat{C}/P^2)\mathrm{d}P/\mathrm{d}t$, on the mantle, where $\widehat{C}$ is the axial moment of inertia of the mantle. The LOD in panel (**a**) is arbitrary to within an additive constant, chosen here to obtain agreement at 1972.5 with Gross (2001).

a connection between them (e.g., Braginsky, 1970; Gillet et al., 2010). Figure 1c supports this quest. It shows the LOD data (Gross, 2001; Holme and de Viron, 2005) plotted against the estimated LOD variations inferred from the core flow models of Jackson (1997) that are based on inversion of geomagnetic secular variation data. The qualitative agreement implies that the variations in LOD are due to core-mantle angular momentum exchange associated with magnetohydrodynamic (MHD) processes in the core.

This review will focus on variations in LOD, i.e., changes in $\Omega_z(\approx \Omega)$. Precession and nutation of the Earth's axis, which describe variations in Ω_x and Ω_y, are also phenomena that cannot be satisfactorily explained without invoking core-mantle torques, but they are beyond the scope of this review. It will become clear that torques on the Solid Inner Core (SIC) are also of interest. Variables in the SIC will be distinguished by a tilde ($\widetilde{\ }$) and those in the mantle by a hat ($\widehat{\ }$). Except when making general statements, unadorned letters will refer to variables in the Fluid Outer Core (FOC).

The four coupling processes

The torque on the mantle about the geocenter O is

$$\widehat{\mathbf{\Gamma}} = \oint_{\widehat{\mathrm{S}}} \mathbf{r} \times \widehat{\mathbf{T}}\, \mathrm{dA}, \quad \text{where} \quad \widehat{T}_i = -\widehat{S}_{ij} n_j, \tag{1a,b}$$

sometimes called the "surface traction," is the stress associated with the normal and $\widehat{S}_{ij}$ is the total stress tensor; $\mathbf{r} = r\mathbf{1}_r$ is the radius vector from O, $r = |\mathbf{r}|$. The minus sign in Equation 1b arises because our unit normal, $\mathbf{n}$, to $\widehat{\mathrm{S}}$, the Core Mantle Boundary (CMB), points into the mantle. The axial torque, i.e., the component of $\widehat{\mathbf{\Gamma}}$ along the rotation axis Oz, is

$$\widehat{\Gamma}_z = -\oint_{\widehat{\mathrm{S}}} s\widehat{S}_{\phi n}\, \mathrm{dA}, \tag{1c}$$

where s is distance from the z-axis. For the torque on the SIC, we have similarly

$$\widetilde{\mathbf{\Gamma}} = \oint_{\widetilde{\mathrm{S}}} \mathbf{r} \times \widetilde{\mathbf{T}}\, \mathrm{dA}, \qquad \widetilde{T}_i = \widetilde{S}_{ij} n_j,$$
$$\widetilde{\Gamma}_z = \oint_{\widetilde{\mathrm{S}}} s\widetilde{S}_{\phi n}\, \mathrm{dA}; \tag{1d,e,f}$$

there is no minus sign in Equations 1e, f because our unit normal, $\mathbf{n}$, to the Inner Core Boundary (ICB) points out of the SIC.

Equation 1a tacitly assumes that the core alone exerts a torque on the mantle; sources of torque from outside the Earth are ignored, and therefore

$$\mathbf{\Gamma} + \widehat{\mathbf{\Gamma}} + \widetilde{\mathbf{\Gamma}} = \mathbf{0},$$
$$\mathbf{M} + \widehat{\mathbf{M}} + \widetilde{\mathbf{M}} = \text{constant}, \tag{1g,h}$$

where $\mathbf{\Gamma}$ is the torque on the FOC; $\mathbf{M}$, $\widehat{\mathbf{M}}$ and $\widetilde{\mathbf{M}}$ are the corresponding angular momenta. Equation 1g implies that, if one of the three torques changes, so do one or two of the others, in the opposite sense. The system is, in this respect, self-regulating. We shall treat the mantle and SIC as rigid bodies below.

Stress is exerted on the CMB in four ways: through viscosity, topography, gravity, and magnetic field, and there are correspondingly four parts to each of S_{ij}, $\mathbf{T}$ and $\mathbf{\Gamma}$, e.g., $\widehat{\mathbf{\Gamma}} = \widehat{\mathbf{\Gamma}}^V + \widehat{\mathbf{\Gamma}}^T + \widehat{\mathbf{\Gamma}}^G + \widehat{\mathbf{\Gamma}}^M$. The topographic and gravitational torques depend on the non-sphericity of $\widehat{\mathrm{S}}$ and $\widetilde{\mathrm{S}}$. For the others, negligible error is made by replacing the CMB and ICB by spheres, $\widehat{\mathrm{S}}_\bullet$ and $\widetilde{\mathrm{S}}_\bullet$, of radii r_o and r_i. The torques will be estimated below.

The viscous torque

Assuming uniform fluid density, ρ, and kinematic viscosity, ν, the part of the viscous stress tensor, $\widehat{S}^V_{ij}$, responsible for $\widehat{T}^V_i$ is $\rho\nu\nabla_j V_i$, i.e., $\widehat{\mathbf{T}}^V = -\rho\nu(\mathbf{n}\cdot\nabla)\mathbf{V} \approx -\rho\nu\partial_r\mathbf{V}$ so that, by Equations 1a, c,

$$\widehat{\mathbf{\Gamma}}^V = -\rho\nu \oint_{\widehat{\mathrm{S}}} \mathbf{r} \times \partial_r \mathbf{V}\, \mathrm{dA},$$
$$\widehat{\Gamma}^V_z = -\rho\nu \oint_{\widehat{\mathrm{S}}} s\partial_r V_\phi\, \mathrm{dA}. \tag{2a,b}$$

These torques involve only the radial gradient of the fluid velocity, $\mathbf{V}$. This tends to drag the mantle in the direction of the subsurface flow.

The viscosity of core fluid is hard to estimate. First principles calculations (de Wijs et al., 1998; Dobson et al., 2000; Vočadlo et al., 2000) suggest that ν at the CMB is within a factor of 3 of 10^{-6} m^2 s^{-1}. Suppose the viscous stress transfers momentum between the core and mantle over a length scale $d_\nu = E^{1/2} r_o \sim 0.2$ m, which is the thickness of the laminar Ekman boundary layer. Here

$$E = \nu/\Omega\mathcal{L}^2 \tag{2c}$$

is the Ekman number ($\approx 3 \times 10^{-15}$), which quantifies the ratio of the viscous and Coriolis forces; $\mathcal{L}$ is a characteristic scale of motion outside the boundary layer, for which we take $\mathcal{L} = r_o$. Assuming velocities of order $\mathcal{V} \approx 10^{-4}$ m s^{-1} (e.g., Jackson, 1997), the surface traction, $\widehat{T}^V \approx \rho\nu\mathcal{V}/d_\nu$, is about 10^{-5} N m^{-2}, implying that $\widehat{\Gamma}^V \approx 5 \times 10^{14}$ Nm.

In a highly turbulent medium such as the FOC, small scale motions transport macroscale quantities, such as angular momentum, far more effectively than molecular diffusion. When these scales are too small to be resolved by numerical computations, they are termed "sub-grid scales." Their effect must then be included in some other way. Appeal is often made to an analogy with molecular diffusion. Molecular transport depends on the molecular mean-free-path, ℓ, and the rms molecular speed, u. Simple

dynamical arguments show that the molecular diffusivity, ν, for momentum is of order $u\ell$. The analogy pictures small scale eddies replacing molecules as the transporters of macroscale momentum. The correlation length, $l_{\rm cor}$, of the turbulence replaces ℓ and the rms turbulent velocity, υ, replaces u. The transport of macroscale momentum is then governed by a kinematic "turbulent viscosity" $\nu_T \approx \upsilon l_{\rm cor}$, which greatly exceeds ν. We use $\upsilon = 10^{-4}$ m s^{-1} for the velocity scale. The length scale is harder to estimate. Here we take $l_{\rm cor} \sim E^{1/3} r_o \approx 100$ m, which is based upon the characteristic length scale for finite amplitude rapidly rotating convection (e.g., Stellmach and Hansen, 2004; Sprague et al., 2006). This gives $\nu_T \approx 10^{-2}$ m^2 s^{-1}. Though it is strictly inconsistent to use υ and $l_{\rm cor}$ when estimating the shear on the resolved scales, an upper bound on the turbulent traction follows from doing so: $\widehat{T}^V \approx \rho \nu_T \upsilon / l_{\rm cor} \approx \rho(\upsilon l_{\rm cor})\upsilon / l_{\rm cor} \approx 10^{-4}$ N m^{-2}, implying $\widehat{\Gamma}^V_z \lessapprox 5 \times 10^{15}$ Nm.

This may overestimate $\widehat{\Gamma}^V_z$. A stable layer may exist at the top of the FOC; see, e.g., Loper (2007), Buffett (2010). Braginsky (1999) pointed out that the light material released during the freezing of the SIC may preferentially congregate near the ICB, and that this may answer unresolved questions about the geomagnetic secular variation (Braginsky, 1984). Turbulent motions in a buoyantly stable layer tend to be damped preferentially in the direction of stratification, and this reduces the macroscale momentum transport across the layer (e.g., Gargett, 1984; Davidson, 2004). Waves in such a layer may increase what ν alone can do in transporting macroscale momentum (e.g., Rogers and Glatzmaier, 2006). But it is doubtful if they can transport it as effectively as ν_T for fully convective turbulence far from boundaries.

Though these and similar arguments lack rigor, the above estimates of $\widehat{\Gamma}^V$ are less than the target torque, but not vastly so (cf. Kuang and Bloxham, 1997; Brito et al., 2004; Deleplace and Cardin, 2006; Buffett and Christensen, 2007).

The topographic torque

The likelihood that there are inverted mountains and valleys on the CMB, and that these might create topographic torques large enough to explain the observed changes in LOD, was first suggested by Hide (1969). These irregularities are often collectively called "bumps," and their study was jokingly christened "geophrenology" by the late Keith Runcorn. Hide's idea generated much interest and literature, e.g., Anufriev and Braginsky (1975; 1977a; b), Jault and Le Mouël (1989), Kuang and Bloxham (1993, 1997), Buffett (1998) and Kuang and Chao (2001). Seismic studies infer the bump height, $\mathcal{H}$, is of order 1 km (e.g., Tanaka, 2010). See *Earth's Structure, Lower Mantle*.

Topographic coupling between the FOC and its boundaries depends on deviations from sphericity in the shapes of the CMB and ICB. The fluid pressure, p, creates surface tractions, $\widehat{\mathbf{T}}^T = p\mathbf{n}$ and $\widetilde{\mathbf{T}}^T = -p\mathbf{n}$, that are not purely radial. The resulting topographic torques on the CMB and ICB are

$$\widehat{\mathbf{\Gamma}}^T = \oint_{\widehat{\rm S}} p\mathbf{r} \times \mathbf{n}\, {\rm dA}, \qquad \widetilde{\mathbf{\Gamma}}^T = -\oint_{\widetilde{\rm S}} p\mathbf{r} \times \mathbf{n}\, {\rm dA}. \tag{3a,b}$$

Equal but opposite torques act on the FOC, so that (cf. Equation 1g)

$$\mathbf{\Gamma}^T = -\widehat{\mathbf{\Gamma}}^T - \widetilde{\mathbf{\Gamma}}^T = -\int_{\rm V} \mathbf{r} \times \boldsymbol{\nabla} p\, {\rm dV}. \tag{3c}$$

We define the CMB and ICB by

$$r = r_o + \widehat{h}(\theta, \phi), \quad r = r_i + \widetilde{h}(\theta, \phi), \tag{4a,b}$$

where $(r,\ \theta,\ \phi)$ are spherical coordinates. Equations 3a, b can be simplified if it is assumed that $\left|\widehat{h}\right|/r_o \ll 1$, $\left|\widetilde{h}\right|/r_i \ll 1$, $\left|\boldsymbol{\nabla}\widehat{h}\right| \ll 1$ and $\left|\boldsymbol{\nabla}\widetilde{h}\right| \ll 1$; see RA12. The projection of Equations 3a, b onto the spheres $\widehat{\rm S}_\bullet$ and $\widetilde{\rm S}_\bullet$ are then

$$\widehat{\mathbf{\Gamma}}^T = \oint_{\widehat{\rm S}_\bullet} \widehat{h}\mathbf{r} \times \boldsymbol{\nabla} p\, {\rm dA}_\bullet, \qquad \widetilde{\mathbf{\Gamma}}^T = -\oint_{\widetilde{\rm S}_\bullet} \widetilde{h}\mathbf{r} \times \boldsymbol{\nabla} p\, {\rm dA}_\bullet. \tag{4c,d}$$

The torques $\widehat{\mathbf{\Gamma}}^T$ and $\widetilde{\mathbf{\Gamma}}^T$ obviously depend on variations in p in the FOC, and we consider next the causes and magnitudes of these. This necessitates a considerable digression. The first step is to develop a reference state.

Convection mixes the FOC so well that, except in thin boundary layers at the CMB and ICB, it is chemically and thermodynamically homogeneous. It is therefore isentropic, i.e., its specific entropy, S, is uniform. The core is an unknown mixture of all elements, but the basics can be understood by assuming that it is a binary alloy of Fe and a lighter element, X, whose mass fraction is X. It is usually supposed that X is mostly Si or S, but it is unnecessary to be specific here. Except in boundary layers,

$$S = S_a = \text{Constant}, \qquad X = X_a = \text{Constant, in the FOC}, \tag{5a,b}$$

where the suffix $_a$ stands for "adiabatic".

Although fast enough to mix the core thoroughly, core flows are slow compared with the speed of sound, u_s ($\approx 10^4$ m s^{-1}). The primary dynamical balance is therefore hydrostatic and, allowing for centrifugal forces, it is governed by

$$\boldsymbol{\nabla} p_a = \rho_a(\mathbf{g}_a - \mathbf{\Omega} \times (\mathbf{\Omega} \times \mathbf{r})) = \rho_a\left(\mathbf{g}_a + \frac{1}{2}\nabla(\mathbf{\Omega} \times \mathbf{r})^2\right), \tag{5c}$$

where $\mathbf{\Omega} = \Omega \mathbf{1}_z$ is the angular velocity of the Earth and $\mathbf{g}$ is the gravitational acceleration. Newtonian gravitation theory requires that

$$\boldsymbol{\nabla} \times \mathbf{g} = \mathbf{0}, \quad \boldsymbol{\nabla} \cdot \mathbf{g} = -4\pi G\rho, \tag{5d,e}$$

where G is the constant of gravitation. It follows that

$$\boldsymbol{\nabla} p_a = \rho_a \mathbf{g}_e = -\rho_a \boldsymbol{\nabla} \Phi_e, \quad \text{where} \quad \mathbf{g}_e = -\boldsymbol{\nabla}\Phi_e \tag{5f,g}$$

is the effective gravitational field and $\Phi_e = \Phi_a - \frac{1}{2}(\mathbf{\Omega} \times \mathbf{r})^2$ is the "effective gravitational potential." Equation 5d shows that p_a, ρ_a, ... are constant on equipotential surfaces:

$$p_a = p(\Phi_e, S_a, X_a),$$
$$\rho_a = \rho(\Phi_e, S_a, X_a) = -\partial p(\Phi_e, S_a, X_a)/\partial \Phi_e, \ldots \tag{5h,i}$$

The effect of the centrifugal forces is quantified by $\varepsilon_\Omega = \Omega^2 r/g$. This is small, varying from 1.7×10^{-3} at the CMB to 1.5×10^{-3} at the ICB. The deviation of the equipotential surfaces from spheres is therefore small, as are deviations caused by the gravitational field produced by density anomalies in the mantle and SIC, quantified below. It is therefore helpful to refer to departures from a "reference state" that is spherically symmetric: $\Phi = \Phi^s(r)$, $p = p^s(r)$, $\rho = p^s(r)$, $T = T^s(r)$, etc., where T is temperature. There are large departures from adiabaticity in boundary layers and smaller departures throughout the FOC that are of two main types:

(a) *Deviations from Φ^s due to rotation and density anomalies in the mantle and SIC.* These will be denoted by a prime, e.g., $p'_a = p_a - p^s$. Rotation produces the larger deviation but, as will be seen below, this is less relevant to LOD variations than the anomaly created by the mantle, which in the FOC is dominantly

$$\Phi'_a = A'(r/r_o)^2 \sin^2\theta \cos\ 2\phi, \quad (A' > 0) \tag{6}$$

Wahr and deVries (1989), Forte et al. (1994). The value of the constant A' is about 1,300 $m^2\ s^{-2}$, according to Defraigne et al. (1996) and about 2,300 $m^2\ s^{-2}$ according to Forte et al. (1994); our compromise will be A' =1,800 $m^2\ s^{-2}$. By Equation 5i, $p'_a \approx -\rho^s_a \Phi'_a$. Therefore $\varepsilon_a = p'_a/p^s_a$ is 10^{-4} on the CMB equator and 10^{-5} at the ICB equator.

(b) *Deviations created by convection.* We use the notation

$$\rho = \rho_a + \rho_c, \tag{7a}$$

and similarly for other variables. The Earth radiates energy into space at a rate estimated to exceed 43 TW (e.g., §4.1.5 of Schubert et al., 2001). We take an extreme position by supposing the entire 43 TW emerges from the core. The outward heat flux in the FOC is the sum of the convective heat flux q_c and the adiabatic heat flux $q_a = -KdT^s/dr$, where K is thermal conductivity. Though the latter may be as much as 5 TW, we ignore it. Then q_c = 0.28 W m^{-2} at the CMB. We take

$$q_c = \rho c_p \overline{T_c V_r}, \tag{7b}$$

where c_p (≈800 J kg^{-1} K^{-1}) is the specific heat at constant pressure, p. The overline denotes a horizontal average over the flow, which is undoubtedly highly turbulent. For $V_r = 10^{-4}$ m s^{-1}, it follows that $T_c = 3.5 \times 10^{-4}$ K. As $T_a \approx 4,000$ K (e.g., Kawai and Tsuchiya, 2009), $\varepsilon_c = T_c/T_a$ is less than 10^{-7}, which is 3–4 orders of magnitude smaller than ε_a. Even this is an overestimate; it has never been suggested that Q_c is larger than 15 TW. The smallness of ε_Ω, ε_a, and ε_c means that all these effects can be treated as perturbations of the reference state.

As $p'_a(r,\ \theta,\ \phi) \gg p_c(r,\ \theta,\ \phi)$, it is sensible to consider first the effect of p'_a by introducing the "adiabatic topographic torques" on the mantle, ICB, and FOC:

$$\widehat{\mathbf{\Gamma}}^T_a = \oint_{\widehat{S}} p_a\, \mathbf{r} \times \mathbf{n}\, dA,$$
$$\widetilde{\mathbf{\Gamma}}^T_a = -\oint_{\widetilde{S}} p_a\, \mathbf{r} \times \mathbf{n}\, dA, \tag{8a,b,c}$$
$$\mathbf{\Gamma}^T_a = -\int_V \mathbf{r} \times \boldsymbol{\nabla} p_a\, dV.$$

If the CMB (ICB) were an equipotential or if it were spherical, $\widehat{\mathbf{\Gamma}}^T_a \left(\widetilde{\mathbf{\Gamma}}^T_a\right)$ would vanish according to Equation 8a, b, but generally these torques are nonzero. They can be evaluated only if $\widehat{p}$ ($\widetilde{p}$) is known on the CMB (ICB). It will be shown in the next section that $\widehat{\mathbf{\Gamma}}^T_a$ and $\widetilde{\mathbf{\Gamma}}^T_a$ are intimately related to what we shall call "adiabatic gravitational torques." We therefore postpone further discussion and estimation of adiabatic topographic torques.

Consider the torque $\widehat{\mathbf{\Gamma}}^T_c$ associated with the convective motions in the FOC:

$$\widehat{\mathbf{\Gamma}}^T_c = \oint_{\widehat{S}_\bullet} \widehat{h}\mathbf{r} \times \boldsymbol{\nabla} p_c\, dA_\bullet,$$
$$\widehat{\Gamma}^T_{c,z} = \oint_{\widehat{S}_\bullet} \widehat{h}\partial_\phi p_c\, dA_\bullet. \tag{9a,b}$$

Reasons will be given in the section on the "Magnetic Torque" why core flow may be well described by the magnetostrophic approximation Equation 20a, and why, deep in the core, Coriolis and Lorentz forces are comparable, implying a magnetic field strength $\mathcal{B}$ there of about 2 mT, or about four times greater than the typical field strength $\mathcal{B}_o$ on the CMB. The Lorentz force is therefore 16 times less on the CMB than in the bulk of the core. Also, as g_ϕ, is small, $\partial_\phi p_c \approx -2\Omega\rho_0 r_o V_\theta \cos\theta \sin\theta$ should be a good approximation to the ϕ-component of Equation 20a on the CMB. Therefore (Hide et al., 1993)

$$\widehat{\Gamma}^T_{c,z} = -2\Omega\rho_0 r_o \oint_{\widehat{S}_\bullet} \widehat{h}(\theta,\phi) V_\theta(r_o,\theta,\phi)\cos\theta\sin\theta\,\mathrm{dA}_\bullet. \tag{9c}$$

In principle, $\widehat{\Gamma}^T_{c,z}$ can be estimated by extracting $\widehat{h}$ from seismological analysis, and by using the V_θ (r_o, θ, ϕ) inferred from the core surface motion. In practice, this is difficult and has generated controversy. Equation 9c suggests that

$$\widehat{\Gamma}^T_{c,z} = \mathrm{O}\left(2\Omega\rho\mathcal{V}\mathcal{H}r_o^3\right), \tag{9d}$$

which is 10^{18} Nm for a bump height of $\mathcal{H}$ = 100 m. Such a bump height is well within the bounds set by recent seismic investigations (e.g., Tanaka, 2010). Equation 9b indicates, however, that Equation 9d may be a serious overestimate because p_c is a single-valued function and $\partial_\phi p_c$ is as often positive as negative in the integrand of Equation 9b. Though $\pm 2\Omega\rho\mathcal{V}r_o$ is a reasonable estimate of $\partial_\phi p_c$ at most points on the CMB, considerable cancellation is likely when evaluating the integral in Equation 9b. There is even an outside chance that the cancellation might be complete; see Anufriev and Braginsky (1978b).

Reliable estimation of the convective topographic torque must probably await careful experiments and allied theory. No argument has so far convincingly demonstrated that topography can create torques of the target magnitude of 10^{18} Nm but, equally, none have shown that it cannot.

The gravitational torque

The gravitational torque on a body V of density $\rho(\mathbf{x})$ in a gravitational field $\mathbf{g}(\mathbf{x})$ is

$$\mathbf{\Gamma}^G = \int_V \rho\,\mathbf{r}\times\mathbf{g}\,\mathrm{dV}. \tag{10a}$$

This volume integral can be usefully transformed into a surface integral by drawing on the analogy between the theories governing Newtonian gravitation and electrostatics, the only difference between these theories being one of sign: like charges repel but all bodies attract gravitationally. It can be shown that

$$\rho g_i = \nabla_j S^G_{ij}, \quad \text{where} \quad S^G_{ij} = -\frac{1}{4\pi G}\left(g_i g_j - \frac{1}{2}g^2\delta_{ij}\right) \tag{10b,c}$$

is the gravitational stress tensor, the gravitational pressure $-g^2/8\pi G$ being also the gravitational energy density. Equations 10b, c enable Equation 10a to be written as a surface integral:

$$\mathbf{\Gamma}^G = -\frac{1}{4\pi G}\oint_S \mathbf{r}\times\left[(\mathbf{n}\cdot\mathbf{g})\mathbf{g} - \frac{1}{2}g^2\mathbf{n}\right]\mathrm{dA}, \tag{10d}$$

where $\mathbf{n}$ points out of V. See RA12 and Appendix B of Braginsky and Roberts (1995) for derivations of these results. When they are applied below, $\mathbf{n}$ on the CMB and SIC will, as previously defined, be oriented approximately parallel to $\mathbf{r}$.

By Equation 10a, the gravitational torque on the FOC due to the mantle and SIC is

$$\mathbf{\Gamma}^G = \int_V (\rho_a+\rho_c)\mathbf{r}\times(\mathbf{g}_a+\mathbf{g}_c)\mathrm{dV} = \mathbf{\Gamma}^G_a + \mathbf{\Gamma}^G_c, \tag{11a}$$

where $\mathbf{\Gamma}^G_a$ and $\mathbf{\Gamma}^G_c$ are the adiabatic and convective parts of $\mathbf{\Gamma}^G$:

$$\mathbf{\Gamma}^G_a = \int_V \rho_a\mathbf{r}\times\mathbf{g}_a\,\mathrm{dV}, \qquad \mathbf{\Gamma}^G_c = \int_V \mathbf{r}\times(\rho_c\mathbf{g}_a + \rho_a\mathbf{g}_c + \rho_c\mathbf{g}_c)\mathrm{dV}. \tag{11b,c}$$

It was pointed out earlier that $\rho_c = \mathrm{O}(10^{-4}\rho'_a)$, $g_c = \mathrm{O}(10^{-4}g'_a)$, etc. Apparently therefore $\Gamma^G_c = \mathrm{O}(10^{-4}\Gamma^G_a)$, making it sensible to focus first on the adiabatic torque.

Consistent with hydrostatic balance in the FOC (see Equation 5f), Equations 8c and 11b, give

$$\mathbf{\Gamma}^{G+T}_a = \mathbf{\Gamma}^G_a + \mathbf{\Gamma}^T_a = \int_V \mathbf{r}\times(\rho_a g_a - \boldsymbol{\nabla}p_a)\mathrm{dV} = \mathbf{0}. \tag{12a}$$

By Equations 8a, b and 10d and the continuity of $\mathbf{g}$ and p, we also have

$$\widehat{\mathbf{\Gamma}}^{G+T}_a = \oint_{\widehat{S}} \mathbf{r}\times\left\{p_a\mathbf{n} + (4\pi G)^{-1}\left[(\mathbf{n}\cdot\mathbf{g}_a)g_a - \frac{1}{2}g_a^2\mathbf{n}\right]\right\}\mathrm{dA}, \tag{12b}$$

$$\widetilde{\mathbf{\Gamma}}^{G+T}_a = -\oint_{\widetilde{S}} \mathbf{r}\times\left\{p_a\mathbf{n} + (4\pi G)^{-1}\left[(\mathbf{n}\cdot\mathbf{g}_a)g_a - \frac{1}{2}g_a^2\mathbf{n}\right]\right\}\mathrm{dA}, \tag{12c}$$

from which, in agreement with Equation 12a,

$$\widehat{\mathbf{\Gamma}}^{G+T}_a + \widetilde{\mathbf{\Gamma}}^{G+T}_a = \mathbf{0}. \tag{12d}$$

If the torques $\widehat{\mathbf{\Gamma}}^{G+T}_a$ and $\widetilde{\mathbf{\Gamma}}^{G+T}_a$ are nonzero, $\widehat{\mathbf{\Omega}}$ and $\widetilde{\mathbf{\Omega}}$ evolve. The consequent change in the relative orientation of the mantle and SIC modifies $\mathbf{g}_a$ and p_a in Equation 12b, c so that the system evolves toward a configuration of minimum energy E. In this configuration

$$\widehat{\mathbf{\Gamma}}^{G+T}_a = \mathbf{0}, \qquad \widetilde{\mathbf{\Gamma}}^{G+T}_a = \mathbf{0}. \tag{13a,b}$$

If this minimum energy, torque-free state is perturbed, the restoring GT-torques (as we shall call them) set up a "gravitational oscillation" of the SIC relative to the mantle.

To give a simple example, suppose that the gravitational anomaly defined by Equation 6 is created by sources entirely within the mantle, the CMB having no

bumps, so that $\widehat{\Gamma}^{G+T}_{a,z} = \widehat{\Gamma}^{G}_{a,z}$. Similarly, suppose the SIC is spherical but has internal sources that above the ICB produce the gravitational anomaly

$$\Phi''_a = A''(r_i/r)^3 \sin^2\theta \cos 2(\phi - \varphi), \quad (A'' > 0), \tag{14a}$$

where φ is the angular displacement of the system from the stable state, $\varphi = 0$, in which Equations 13a, b hold. Equations 12b, c show that

$$\widehat{\Gamma}^{G}_{a,z} = -\widetilde{\Gamma}^{G}_{a,z} = \Gamma^{G}_{0} \sin 2\varphi, \quad \text{where} \quad \Gamma^{G}_{0} = 8A'A''r_i^3/3Gr_o^2 (> 0). \tag{14b,c}$$

These torques vanish for the stable minimum energy states $\varphi = 0, \pi$ (and also for the unstable $\varphi = \pm\frac{1}{2}\pi$). Small departures from a stable state satisfy

$$\widehat{C} d_t^2 \widehat{\varphi} = 2\Gamma^{G}_{0}(\widetilde{\varphi} - \widehat{\varphi}), \quad \widetilde{C} d_t^2 \widetilde{\varphi} = 2\Gamma^{G}_{0}(\widetilde{\varphi} - \widehat{\varphi}), \tag{14d,e}$$

where $\widehat{C}$ (= 7.12×10^{37} kg m^2) and $\widetilde{C}$(= 5.86×10^{34} kg m^2) are the polar moments of inertia of mantle and SIC, respectively. The frequency, ω^G, of the oscillation is

$$\omega^G = [2(\widehat{C} + \widetilde{C})\Gamma^{G}_{0}/\widehat{C}\widetilde{C}]^{1/2} \approx [2\Gamma^{G}_{0}/\widetilde{C}]^{1/2}. \tag{14f}$$

Although an anomaly of the form of Equation 14a could be produced by density variations within the SIC, it is more plausibly created by SIC topography for the following reasons. It is generally believed that the SIC is the result of freezing of the FOC, an ongoing process even today (Jacobs, 1953). An alloy generally changes its composition when it changes phase. The rather large density jump at the ICB, $\widetilde{\Delta} = \widetilde{\rho}(r_i) - \rho(r_i) \approx 600$ kg m^{-3}, is hard to attribute to contraction on freezing but can be readily explained as a small reduction in X on freezing. Phase equilibrium at the ICB implies $T^s_a(\Phi_a, S_a, X_a) = T_m(p_a, X_a)$, where T_m is the melting temperature. This implies that the ICB is an equipotential surface. Since $\Phi = \Phi^s_a(r) + \Phi'_a(r,\theta,\phi)$ where $|\Phi'_a/\Phi^s_a| \ll 1$, Taylor expansion, using Equation 4b, shows that $\Phi^s_a(r_i) + \widetilde{g}\widetilde{h}(\theta,\phi) + \Phi'_a(r_i,\theta,\phi)$ is approximately constant, where $\widetilde{g} = -g^s_{a,r}(r_i) = \partial_r \Phi^s_a(r_i) (> 0)$ is gravity at the ICB. It follows that

$$\widetilde{h} = -\Phi'_a(r_i,\theta,\phi)/\widetilde{g} = \widetilde{\varepsilon} \sin^2\theta \cos 2\phi, \quad \widetilde{\varepsilon} = -A'(r_i/r_o)^2/\widetilde{g}. \tag{14g,h}$$

This shows how the gravitational anomaly in the mantle imposes its $n = m = 2$ preference on the SIC. It makes the otherwise ad hoc assumption of Equation 14a seem perfectly reasonable. The condition that $\widetilde{h}$ creates Equation 14a, for $\varphi = 0$ and $r - r_i \gg \widetilde{h}$ is

$$A''/A' = 4\pi G r_i^3 \widetilde{\Delta}/5r_o^2\widetilde{g} \approx 0.0034. \tag{14i}$$

The maximum bump height on the ICB is $|\widetilde{\varepsilon}| \approx 50$ m. Nonzero φ corresponds to a rotated SIC. Such a rotation is to be expected; core turbulence continually subjects the SIC to (topographic) torques that continuously change its orientation. Two relaxation processes act to restore the ICB to its equipotential: (i) flow within the SIC, (ii) new freezing/melting on the ICB. If either were instantaneous, there would be no torque between the mantle and SIC, but both appear to act on much longer time scales than core turbulence, so that SIC topography is almost "frozen" to the SIC as it turns.

Concerning (i), the viscosity of the SIC is plausibly much less than the viscosity of the mantle. According to Schubert et al. (2001) $\widehat{\nu} \approx 5 \times 10^{19}$m^2 s^{-1} in the deep mantle but, according to Mound and Buffett (2006), $\widetilde{\nu} \gtrsim 10^{13}$m^2 s^{-1}. Whereas mantle anomalies are essentially "frozen in," slow motions within the SIC created by stresses exerted by the FOC on the ICB can gradually restore equilibrium (Yoshida et al., 1996; Buffett, 1997). Concerning (ii), the thermodynamic disequilibrium created by the misalignment of the ICB from its equipotential surface is slowly removed by new freezing of the FOC or new melting of the SIC. This processes has not been fully explored (but see Fearn et al., 1981; Morse, 1986). The possible significance of melting/freezing processes on SIC structure has been recently investigated by Alboussière et al. (2010) and Monnereau et al. (2010).

Interest in gravitational torques and oscillations was sparked by Buffett (1996). We follow him but by a different method, making use of Equations 14c, i:

$$\Gamma^{G}_{0} = 32\pi r_i^6 \widetilde{\Delta} A'^2/15 r_o^4 \widetilde{g} \approx 6.7 \times 10^{19}\,\text{Nm} \tag{15a}$$

By Equation 14f, the frequency of the oscillation is $\omega^G \approx 4.8 \times 10^{-8}$ s^{-1}, with a period of

$$\tau^G = 2\pi/\omega^G \approx 4.1 \text{ years}. \tag{15b}$$

According to Buffett et al. (2009), gravitational oscillations are mainly responsible for the LOD variations shown in Figure 1. Mound and Buffett (2006) obtain $\Gamma^{G}_{0} \approx 1.5 \times 10^{20}$ Nm.

Equations 14d, e imply, for some t_0,

$$\widehat{\Omega} = \widehat{\Omega}_0 + d_t\widehat{\phi} = \widehat{\Omega}_0 + (2\Gamma^{G}_{0}/\widehat{C}\omega^G)(\widetilde{\phi} - \widehat{\phi})_{\max} \sin\omega^G(t - t_0). \tag{15c}$$

The amplitude of the gravitational oscillation is therefore related to that of the variation, ΔP, in LOD by

$$\left(\widetilde{\phi} - \widehat{\phi}\right)_{\max} = \pi\widehat{C}\omega^G \Delta P/\Gamma^{G}_{0} P_0^2 \approx 1.2^\circ, \tag{15d}$$

for $\Delta P = 1$ ms. This gives a maximum angular velocity difference of $\omega^G\left(\widetilde{\phi} - \widehat{\phi}\right)_{\max} \approx 2^\circ$ year^{-1}. Furthermore the peak-to-peak variation in the radial gravitational acceleration at the Earth's surface, $r = r_E$, is

$$\Delta g_r''(r_E) = \frac{12A''}{r_i}\left(\frac{r_i}{r_E}\right)^4 (\widehat{\phi} - \widetilde{\phi})^2_{\max} \simeq 4\,\text{nGal}. \qquad (15e)$$

This value is too small by roughly a factor of 5 to be detectable by the GRACE satellite system (e.g., Wahr et al., 2006).

One limitation of this analysis is the neglect of electromagnetic stresses at the boundaries when they are in motion relative to the core fluid. It has been implicitly assumed that the SIC is completely decoupled from the fluid within the tangent cylinder (TC), the imaginary cylinder that touches the ICB at its equator. This is particularly significant because the fluid dynamics inside and outside the TC are quite dissimilar. See Hide and James (1983), Heimpel and Aurnou (2007), and the next section. Because the SIC is as good an electrical conductor as the FOC (or better), it may be tightly coupled magnetically to $\mathcal{C}^N$ and $\mathcal{C}^S$, as suggested by Braginsky (1970); see the next section. To examine the effect of this coupling, we make the extreme assumption that all the fluid in the TC is completely locked to the SIC. Because the mantle is a poor electrical conductor, this fluid is not well coupled to the mantle, so that the entire fluid column within the TC can co-rotate about O_z almost freely with the SIC. This suggests that, instead of Equations 1g, h, a more useful division of the total angular momentum of the Earth might be based on

$$\widehat{\mathbf{\Gamma}} + \mathbf{\Gamma}^{\text{TC}} + \mathbf{\Gamma}^{\text{XTC}} = \mathbf{0}, \qquad \widehat{\mathbf{M}} + \mathbf{M}^{\text{TC}} + \mathbf{M}^{\text{XTC}} = \text{constant}, \qquad (16a,b)$$

where $^{\text{TC}}$ refers to the TC and SIC locked together, and $^{\text{XTC}}$ refers to the part of the FOC exterior to the TC. The moment of inertia of the fluid within the TC is 2.12×10^{35} kg m^2 which, when added to $\widetilde{C}$, gives $C^{\text{TC}} = 2.71 \times 10^{35}$ kg m^2. Using this instead of $\widetilde{C}$ in Equation 14f, τ^{G} is lengthened from 4.1 years to

$$\tau^G_{\text{TC}} = 2\pi/\omega^G_{\text{TC}} \approx 8.9 \text{ years}, \qquad \text{where } \omega^G_{\text{TC}} = [2(\widehat{C} + C^{\text{TC}})\Gamma^G_0/\widehat{C}C^{\text{TC}}]^{1/2}. \qquad (16c,d)$$

See also Mound and Buffett (2006).

Even though ρ_c/ρ_a, p_c/p_a, etc., are of order 10^{-4}, this does not mean that $\Gamma_c^{G+T}/\Gamma_a^{G+T}$ is as small as that. In fact, Equation 13a shows that $\mathbf{\Gamma}_a^{G+T} = \mathbf{0}$ in the minimum energy state. The adiabatic GT-torques dominate the convective torques only if φ is sufficiently large. Stated another way, a convective torque can be nullified by a small departure from the minimum energy state. Earlier, the torque on the SIC created by core turbulence was held responsible for causing φ to deviate from zero. This torque is essentially (magneto-)convective, and is nullified by the GT-torque for a tiny change in φ. Another way of estimating how tiny this φ is equates the magnitudes of the GT-torque, taken as $1.3 \times 10^{20}\,\varphi$ Nm (see Equations 14b, c and 15d), and the convective torque, taken to have its target value of 10^{18} Nm. This gives $\varphi \approx 0.5°$. Within this angle, the mantle and SIC are gravitationally locked together, over short time scales compared with those of the relaxation processes in the SIC described above. See Buffett and Glatzmaier (2000).

The magnetic torque

This section assumes that readers are familiar with pre-Maxwell EM theory and the fundamentals of MHD, including the frozen flux theorem and Alfvén waves. Davidson (2001) contains the necessary background.

It may be useful to remind readers that the magnetic torque about O on a body V carrying a current of density $\mathbf{J}$ is the integrated moment of the Lorentz force, $\mathbf{J} \times \mathbf{B}$:

$$\mathbf{\Gamma}^M = \int_{\text{V}} \mathbf{r} \times (\mathbf{J} \times \mathbf{B})\,\text{dV} = \int_{\text{V}} r[B_r\mathbf{J} - J_r\mathbf{B}]\,\text{dV}. \qquad (17a)$$

The Lorentz force can be expressed as a divergence:

$$(\mathbf{J} \times \mathbf{B})_i = \nabla_j S^M_{ij}, \qquad \text{where } S^M_{ij} = \mu_0^{-1}\left(B_iB_j - \frac{1}{2}B^2\delta_{ij}\right) \qquad (17b,c)$$

is the magnetic stress tensor. An alternative form of Equation 17a is therefore

$$\mathbf{\Gamma}^M = \mu_0^{-1}\oint_{\text{S}} \mathbf{r} \times \left[(\mathbf{n}\cdot\mathbf{B})\mathbf{B} - \frac{1}{2}B^2\mathbf{n}\right]\text{dA}, \qquad (17d)$$

where the unit normal $\mathbf{n}$ to S points out of V. Therefore

$$\widehat{\Gamma}^M_z = -\mu_0^{-1}\oint_{\widehat{\text{S}}} s\widehat{B}_r\widehat{B}_\phi\,\text{dA}, \quad \widetilde{\Gamma}^M_z = \mu_0^{-1}\oint_{\widehat{\text{S}}} s\widetilde{B}_r\widetilde{B}_\phi\,\text{dA}. \qquad (17e,f)$$

These results can be used as they stand to assess the magnetic coupling between the inferred core surface flow and the mantle. See Stix and Roberts (1984), Love and Bloxham (1994), Holme (1998). Here, however, we are more interested in forging a link between the observed changes in LOD and torsional waves. To explain what the latter are, it is necessary to consider some dynamical issues.

Most studies of core MHD are based on the Boussinesq approximation; see, e.g., Braginsky and Roberts (2007). This assumes constant density, $\rho_0 (\approx 10^4 \text{kg m}^{-3})$, and expresses conservation of mass and momentum as

$$\nabla\cdot\mathbf{V} = 0, \quad \partial_t\mathbf{V} + \mathbf{V}\cdot\nabla\mathbf{V} + 2\mathbf{\Omega}\times\mathbf{V} = -\nabla(p_c/\rho_0) + \mathcal{C}\mathbf{g}_e + \mathbf{J}\times\mathbf{B}/\rho_0 + \nu_T\nabla^2\mathbf{V}. \qquad (18a,b)$$

The accelerations in Equation 18b are from inertia ($\partial_t\mathbf{V}$ and $\mathbf{V}\cdot\nabla\mathbf{V}$), rotation ($2\mathbf{\Omega}\times\mathbf{V}$), pressure ($p_c$), buoyancy ($C\mathbf{g}_e$), magnetic field ($\mathbf{J}\times\mathbf{B}/\rho_0$), and viscosity ($\nu_T\nabla^2\mathbf{V}$). Thermal and compositional buoyancy, combined in the

codensity C (Braginsky and Roberts, 1995), maintains the flow and the magnetic field; see *Core Dynamo*.

The Coriolis force is generally more significant than the inertial and viscous forces. This is indicated by the smallness of the Ekman and Rossby numbers:

$$Ro = \mathcal{V}/\Omega\mathcal{L}. \tag{19}$$

See Equation 2c for the definition of E. From $\mathcal{V} = 10^{-4}$ m s^{-1}, $\mathcal{L} = r_o$ and $\nu_T = 10^{-2}$ m^2 s^{-1} follow $Ro \approx 10^{-6}$ and $E \approx 10^{-11}$. This suggests that the inertial and viscous terms can be safely omitted from Equation 18b, except on small length scales.

If the inertial and viscous forces are ejected from Equation 18b, it becomes

$$2\rho_0\mathbf{\Omega} \times \mathbf{V}^{\mathrm{N}} = -\nabla p_c + \rho_0 \mathcal{C}\mathbf{g}_{\mathrm{e}} + \mathbf{J} \times \mathbf{B}, \tag{20a}$$

where $^{\mathrm{N}}$ stands for "non-geostrophic," and "geostrophic" is defined below. Equations 18a and 20a define the "magnetostrophic approximation," often used to describe the quasi-steady macroscales of core MHD. As the viscous term has been ejected, the only boundary condition that $\mathbf{V}^{\mathrm{N}}$ must obey is

$$\mathbf{n} \cdot \mathbf{V}^{\mathrm{N}} = 0, \quad \text{on the CMB and ICB.} \tag{20b}$$

The full boundary conditions of continuous $\mathbf{B}$ and $\mathbf{n} \times \mathbf{E}$ still apply. Because $\partial_t \mathbf{V}$ has been ejected from Equation 20a, there are no Alfvén waves. Instead, the system evolves on the much longer ageostrophic time scale,

$$\tau^{\mathrm{N}} = 2\Omega\mathcal{L}^2/V_{\mathrm{A}}^2 = \tau_\eta/\Lambda, \quad \text{where } \tau_\eta = \mathcal{L}^2/\eta \approx 10^5 \text{ years} \tag{20c,d}$$

is the free decay time for magnetic fields of scale $\mathcal{L}$, and Λ is the "Elsasser number":

$$\Lambda = V_{\mathrm{A}}^2/2\Omega\eta, \quad \text{where} \quad V_{\mathrm{A}} = \mathcal{B}/\sqrt{(\mu_0\rho_0)} \tag{20e,f}$$

is the Alfvén velocity. Elsasser (1946) suggested that $\mathcal{B}$ is determined by a balance of Lorentz and Coriolis forces. Taking $\mathcal{J} \approx \sigma\mathcal{V}\mathcal{B}$, this implies $\Lambda = 1$, $\mathcal{B} \approx 2$ mT, and $V_{\mathrm{A}} \approx 2$ cm s^{-1}. It also gives $\tau^{\mathrm{N}} \approx \tau_\eta \approx 2 \times 10^5$ years for $\mathcal{L} = r_o$.

In cylindrical coordinates (s, ϕ, z), the ϕ-component of Equation 20a is

$$2\Omega\rho_0 V_s^{\mathrm{N}} = -\partial_\phi p_c + (\mathbf{J} \times \mathbf{B})_\phi. \tag{21a}$$

Integrate this over the surface, $\mathcal{C}(s)$, of the circular cylinder of radius s ($> r_i$) coaxial with Oz. The left-hand-side vanishes by mass conservation, as can be verified by integrating Equation 18a over the interior, $\mathcal{I}(s)$, of $\mathcal{C}(s)$ and applying Equation 20b to $\mathcal{N}(s)$ and $\mathcal{S}(s)$, the spherical caps of $\mathcal{C}(s)$ on the CMB that complete the boundary of $\mathcal{I}(s)$. It follows that

$$\int_{\mathcal{C}(s)} (\mathbf{J} \times \mathbf{B})_\phi \, \mathrm{dA} = 0. \tag{21b}$$

If $s < r_i$, there are two cylinders, $\mathcal{C}^N(s)$ and $\mathcal{C}^S(s)$, of radius s to the north and south of the SIC for which

$$\int_{\mathcal{C}^N(s)} (\mathbf{J} \times \mathbf{B})_\phi \, \mathrm{dA} = 0, \quad \int_{\mathcal{C}^S(s)} (\mathbf{J} \times \mathbf{B})_\phi \, \mathrm{dA} = 0. \tag{21c,d}$$

Equations 20b–d are examples of "Taylor's constraint" (Taylor, 1963). The cylinders $\mathcal{C}(s)$ are termed "Taylor cylinders." Of these, $\mathcal{C}(r_i)$ is the tangent cylinder (TC).

It is obviously possible to assign a $\mathbf{J}$ which creates a $\mathbf{B}$ that contradicts Equations 21b–d, at least initially. This shows that Equation 20a is an oversimplification. That approximation rested on discarding the inertial force in comparison with the Coriolis force. Consider however the class of "geostrophic flows":

$$\mathbf{v} = \upsilon(s,\ t)\, \mathbf{1}_\phi. \tag{22a}$$

The corresponding Coriolis acceleration is

$$2\rho_0\mathbf{\Omega} \times \mathbf{v} = -\nabla\mathcal{X}, \quad \text{where} \quad \mathcal{X} = 2\Omega\rho_0 \int \upsilon(s,t)\, \mathrm{d}s \tag{22b,c}$$

can be absorbed into p_c. Coriolis forces are therefore totally ineffective when they act on geostrophic flows. Other forces previously abandoned in comparison with Coriolis forces become influential, especially the inertial forces, which must be restored when analyzing the geostrophic part of core flow. This recovers the Alfvén wave, or something very like it, called the "torsional wave." They share a common time scale:

$$\tau_{\mathrm{A}} = r_o/V_{\mathrm{A}} \approx 6 \text{ years}. \tag{22d}$$

That this is also the time scale $\mathrm{t_{LOD}}$ of the semi-decadal variations of in Figures 1a, b may not be a coincidence, as argued by Gillet et al. (2010).

The geostrophic part $\mathbf{v}$ of $\mathbf{V}$ can be extracted from $\mathbf{V}$ by taking the "geostrophic average," $\langle V_\phi \rangle$, of V_ϕ: for $s > r_i$, this average is defined by

$$\upsilon = \langle V_\phi \rangle \equiv \frac{1}{\widehat{A}(s)} \int_{\mathcal{C}(s)} V_\phi \, \mathrm{dA}, \quad \text{so that} \quad \mathbf{V}^{\mathrm{N}} = \mathbf{V} - \upsilon\mathbf{1}_\phi, \tag{22e}$$

where $\widehat{A}(s) = 4\pi s z_1$ is the area of $\mathcal{C}(s)$, and $z_1(s) = \sqrt{(r_o^2 - s^2)}$ is the semi-length of its sides. The axial angular momentum of the FOC is carried by υ. Therefore, insofar as the rotation of the SIC is locked to that of the fluid in the TC, the angular momentum, $M_z + \widetilde{M}_z$, of the entire core can be derived from the zonal part of the inferred core surface flow. The LOD record provides $\widetilde{M}_z$. Therefore Equation 1h can be tested: $\widehat{M}_z = -(M_z + \widetilde{M}_z)$, Results have been gratifying; see Jault et al. (1988), Jackson (1997) and Figure 1c above. The previous section indicates however that the mantle and SIC are not locked together but take part in

a gravitational oscillation having a period (4–9 years) similar to the torsional wave period $\tau_A \approx 6$ years. The implied convolvement of gravitational and magnetic coupling complicates the task of extracting information about either; see Buffett et al. (2009).

In a torsional wave, the geostrophic cylinders are in relative angular motion about their common (polar) axis; see Figure 2a. The response **b** of **B** to the motion **v** can, as for an Alfvén wave, be visualized using the frozen flux theorem, the field lines behaving like elastic strings threading the cylinders together and opposing their relative motion; see Figure 2b. The resulting torque on a cylinder supplies the restoring force for a wave, the mass of the cylinders providing the inertia. Whenever **J** and **B** contradict Equations 21b–d, a torsional wave is launched that travels in the $\pm s$-indirections.

The canonical torsional wave equation is

$$\frac{\partial^2 \zeta}{\partial t^2} = \frac{1}{s^2 \widehat{A}(s)} \frac{\partial}{\partial s}\left[s^2 \widehat{A}(s) V_A^2(s) \frac{\partial \zeta}{\partial s}\right], \tag{23}$$

where $\zeta(s, t) = \upsilon/s$ is the angular velocity of $\mathcal{C}(s)$ and $V_A(s) = \mathcal{B}_s(s)/(\mu_0 \rho_0)^{1/2}$ is the Alfvén velocity based on the mean $\left(B_s^N\right)^2$ over $\mathcal{C}(s)$: $\mathcal{B}_s^2(s) = \left\langle \left(B_s^N\right)^2 \right\rangle$. Equation 23 is called canonical because it displays the essential nature of torsional waves clearly. It is however not only incomplete but also ignores magnetic coupling to the mantle and SIC. Equation 23 presupposes that the field, $\mathbf{B}^N$, on which the waves ride is axisymmetric. In this case, Equation 23 has a severe singularity at $s = 0$ which excludes physically acceptable solutions. This difficulty can be evaded by supposing that the TC rotates as a solid body, as suggested by Braginsky (1970), and by applying Equation 23 only in XTC. For general, non-axisymmetric $\mathbf{B}^N$, the regular singularity at $s = 0$ is harmless, but unfortunately Equation 23 is then incomplete. The terms missing from Equation 23 represent the transmission of torque from one Taylor cylinder to another by the potential field outside the core. As the terms are troublesome if retained, they are usually abandoned, with an unsubstantiated claim that they are too small to be worth keeping. Whether they are retained or abandoned, the wave equation admits normal mode solutions, i.e., solutions in which ζ is proportional to $\exp(-\imath\omega t)$, where every ω is real, as shown in RA12. When magnetic coupling to the mantle is included, ω acquires a negative imaginary part, representing the ohmic losses in the mantle. The inclusion of magnetic coupling is highly relevant to our focus here, but it clearly adds another layer of complexity.

In view of these theoretical obstacles, the reader may wonder whether computer simulation would not provide a simpler approach. It is however difficult to extract evidence of torsional waves from geodynamo simulations. This is because it is not yet possible to attain geophysically realistic magnetic Prandtl numbers, Pm, in numerical integrations. The importance of viscous damping of torsional waves can be assessed by the ratio of the torsional wave time scale, $\tau_A = r_o/V_A$, to the spin-up time scale, $\tau_{SU} = \sqrt{\left(r_o^2/2\Omega\nu\right)}$, which is their viscous decay time; see Roberts and Soward (1972). This ratio,

$$\tau_A/\tau_{SU} = (2\Omega\nu)^{1/2}/V_A = \sqrt{(Pm/\Lambda)}, \tag{24}$$

is small for the Earth ($\sim 10^{-3}$) but inconveniently large in simulations ($\gtrsim 0.1$). See Wicht and Christensen (2010) for recent simulations of torsional waves.

Space limitations do not permit the mathematical theory of torsional waves to be presented here; see Braginsky (1970), Roberts and Soward (1972), Jault (2003), Dumberry (2007) and RA12. The principal aim in what follows is to outline the underlying physics, that has been employed in theoretical studies, and that will have to be incorporated in numerical models in the future, when computer technology has advanced far enough to permit core MHD to be modeled more faithfully. Our discussion here sidesteps interesting and as yet incompletely answered questions, the first of which is whether torsional waves are involved in any essential way with the semi-

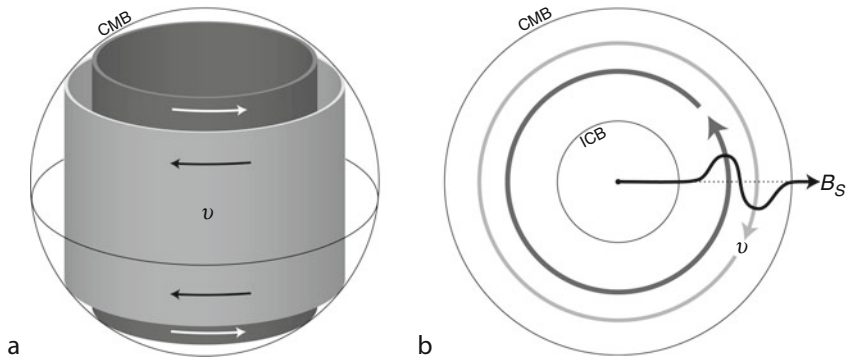

Core-Mantle Coupling, Figure 2 Schematics showing (**a**) geostrophic flows in the core, V^g, and (**b**) plan view of an initially cylindrical magnetic field (*dashed line*) distorted by *v*. The restoring Lorentz torques on the distorted magnetic field, B_s (*solid line*), lead to the cylindrical propagation of torsional waves (Adapted from Dumberry, 2007).

decadal LOD periodicity; might not the gravitational oscillation described in the last section be mainly responsible? The answer is unclear but core field strengths of 2 mT suggest that torsional waves very effectively link together geostrophic motions throughout the core, and that torsional waves therefore necessarily accompany gravitational oscillations. This obviously does not imply that torsional waves couple well to the mantle; if the mantle were an electrical insulator, there would be no magnetic coupling of core and mantle at all. The waves would then be detectable only through the inferred core surface motion. Strong magnetic coupling of the waves to the mantle raises difficult questions about both the excitation and dissipation of the waves. As shown below, the waves are mainly and heavily damped by ohmic dissipation in the mantle. What maintains the waves against this energy loss? No definitive answer has been given to this very significant question. Core turbulence may be directly responsible, or indirectly through the Reynolds magneto-stresses it exerts on the SIC or on the TC. Buffett et al. (2009) find evidence for wave generation at the TC. Core turbulence would presumably excite many damped normal modes. This might help to explain some of the recently discovered short time scales of core surface motions (Olsen and Mandea, 2008; Finlay et al., 2010). It has not been established unequivocally that the 6 year period is the fundamental mode. Though often questioned, evidence of a 60 periodicity exists, This longer period signal might be representative of the fundamental mode but would require current estimates of $\mathcal{B}_s(s)$ to be revised downward.

These matters are beyond the scope of this review. We shall merely sketch, mostly in a qualitative way, the approximate theory that is currently the most complete. We also aim to expose its strengths and weaknesses.

Underlying the entire theory is the idea that core flow can be neatly separated into geostrophic motions of short time scale, τ_A, and non-geostrophic motions of long time scale τ^{N}obeying Equation 20a. In other words, the theory focusses on the large length scales of core flow, in the belief that this includes the fundamental torsional wave mode of greatest interest. The torsional wave therefore rides on a flow satisfying Taylor's constraints Equations 21a–c. Because the Lehnert number, $\lambda = \tau_A/\tau^{\mathrm{N}} = V_A/2\Omega r_o = \omega_A/2\Omega \approx 3 \times 10^{-5}$, is small, the time dependence of $\mathbf{B}^{\mathrm{N}}$ can be ignored in torsional wave theory.

It was pointed out earlier that torsional waves are geostrophic motions in which the inertial force is crucial. The first step in deriving the torsional wave equation is therefore to restore the time-dependent inertial force to Equation 21a, obtaining

$$\rho_0 s\partial_t V_\phi + 2\Omega\rho_0 s V_s = -\partial_\phi p_c + s(\mathbf{J}\times\mathbf{B})_\phi, \qquad (25a)$$

from which $\partial_t\zeta$ is extracted, by taking the geostrophic average; see Equation 22e.

The evaluation of $\langle \mathbf{J}\times\mathbf{B}\rangle_\phi$ is simplified because E is small and the Lundquist number, $Lu = \tau_\eta/\tau_{\mathrm{A}} = V_{\mathrm{A}} r_o/\eta \approx 3\times 10^4$, of the waves is large. In a first approximation, $E = Lu^{-1} = 0$. Then viscous and ohmic diffusion and the associated boundary conditions are discarded. In particular, the electric field created in the FOC by the waves simplifies to

$$\mathbf{e} = -\mathbf{v}\times\mathbf{B}^{\mathrm{N}} - \mathbf{V}^{\mathrm{N}}\times\mathbf{b} - \mathbf{v}\times\mathbf{b}, \qquad (25b)$$

where $\mathbf{b}$ is the magnetic field of the waves. The term $-\mathbf{V}^{\mathrm{N}}\times\mathbf{B}^{\mathrm{N}}$ does not appear because it already acts on the Taylor state. The last term in Equation 25b is also ignored because the wave amplitude is assumed to be small. The ratio of $-\mathbf{V}^{\mathrm{N}}\times\mathbf{b}$ to $-\mathbf{v}\times\mathbf{B}^{\mathrm{N}}$ is of order $A^{\mathrm{N}}[b/\upsilon\sqrt{(\mu_0\rho_0)}]^{-1}$, where $A = V/V_{\mathrm{A}}$ is the Alfvén number, which for the non-geostrophic flow is about 0.1 (see above). As in an Alfvén wave, $\upsilon = \mathrm{O}[b/\sqrt{(\mu_0\rho_0)}]$, so that $|\mathbf{V}^{\mathrm{N}}\times\mathbf{b}| \approx 0.1|\mathbf{v}\times\mathbf{B}^{\mathrm{N}}|$. This, combined with the fact that the inclusion of $-\mathbf{V}^{\mathrm{N}}\times\mathbf{b}$ in $\mathbf{e}$ adds severe complications, encourages the neglect of $-\mathbf{V}^{\mathrm{N}}\times\mathbf{b}$ in Equation 25b, leaving

$$\mathbf{e} = -\mathbf{v}\times\mathbf{B}^{\mathrm{N}}. \qquad (25c)$$

The mantle and core are linked across a boundary layer of Ekman-Hartmann type; e.g., see Dormy et al. (2007). Because $Pm \ll 1$, this has a double structure. Viscosity acts only in an Ekman layer of thickness $d_\nu = \sqrt{(\nu/2\Omega)} \approx 0.1$ m; magnetic diffusion acts in a layer whose thickness is comparable with the EM skin depth, $d_\eta = \left(\frac{1}{2}|\omega|\mu_0\sigma\right)^{-1/2} \approx 10\,\mathrm{km}$. We therefore call this a "magnetic diffusion layer" (MDL), even though Coriolis and Lorentz forces affect its structure too. In the MDL, Equation 25c is replaced by

$$\mathbf{e} = -\mathbf{v}\times\mathbf{B}^{\mathrm{N}} - \eta\boldsymbol{\nabla}\times\mathbf{b} \approx -\mathbf{v}\times\mathbf{B}^{\mathrm{N}} - \eta\mathbf{1}_r\times\partial_r\mathbf{b}. \qquad (26)$$

As $d_\eta/d_\nu \gg 1$, the Ekman layer is only a tiny part of the MDL. Ekman-Hartmann theory simplifies by discarding the Ekman part, setting $\nu = 0$ and abandoning the no-slip boundary conditions. The structure of the MDL still depends on rotation, and on the Elsasser number, Λ, defined in Equation 20e.

The boundary layers play a vital role in linking ζ in the main bulk of the FOC to $\widehat{\mathbf{b}}$ on the CMB and $\widetilde{\mathbf{b}}$ on the ICB. They are therefore essential in determining $\widehat{\mathbf{\Gamma}}^M$ and $\widetilde{\mathbf{\Gamma}}^M$. At the CMB, $\mathcal{B} \approx 0.5$ mT and $\Lambda \approx 0.07$. The prevailing magnetic field, $\mathbf{B}^{\mathrm{N}}$, therefore has very little effect on the boundary layer, which is controlled almost entirely by Coriolis forces and magnetic diffusion. At the ICB, where $\mathcal{B}$ may be even an order of magnitude greater than at the CMB, $\Lambda > 1$, and Lorentz forces are too significant to ignore in the boundary layer. Further details are given in RA12.

The torque exerted by the waves on the mantle is proportional to the electrical conductivity, $\widehat{\sigma}(v, \theta, \phi)$, of the mantle, which we assume is nonzero only in the layer

$r_o < r < r_1 = r_o + d$ at the base of the mantle. The conductance of this layer is

$$\widehat{\Sigma}(\theta,\phi) = \int_{r_o}^{r_1} \widehat{\sigma}\ (r,\theta,\phi)\, dr. \tag{27a}$$

It is commonly assumed that $10^7 S < \widehat{\Sigma} < 10^9$S; we take $\widehat{\Sigma} = 10^8$S below.

Electric currents, $\widehat{\mathbf{j}}$, flow in the mantle, $\widehat{\mathrm{V}}$, either by leaking from the core or by electromagnetic induction, through the time dependence of the EM field on the CMB. We shall be interested in the penetration of the fields **b** and **e** of the waves, at frequencies ω of order 5×10^{-8} s^{-1}. The resulting magnetic and electric fields, $\widehat{\mathbf{b}}$ and $\widehat{\mathbf{e}}$, in the mantle depend on ω and on L, the horizontal length scale imposed by **b** and **e** on the CMB. Associated with ω is the skin depth of the mantle:

$$\widehat{d}_\eta = \left(\frac{1}{2}|\omega|\mu_0\widehat{\sigma}_o\right)^{-1/2}. \tag{27b}$$

Starting with Glatzmaier and Roberts (1995), theoreticians have usually simplified EM theory in the mantle by adopting the "thin-layer approximation" (TLA). This originated from the modeling of laboratory MHD experiments (see, e.g., Müller and Bühler, 2001). It is easily applied and therefore popular, although the conditions for its validity are seldom mentioned or questioned. The TLA demands that $d \ll \widehat{d}_\eta\ (\ll L)$. The horizontal part, $\widehat{\mathbf{e}}_\mathrm{H}$, of the electric field $\widehat{\mathbf{e}}$ is then independent of r, so that

$$\widehat{\mathbf{j}}_\mathrm{H} = \widehat{\sigma}\,\widehat{\mathbf{e}}_\mathrm{H}, \quad \text{and} \quad \widehat{\mathcal{J}} = \widehat{\Sigma}\,\widehat{\mathbf{e}}_\mathrm{H}, \tag{27c,d}$$

where $\widehat{\mathcal{J}}$ is the total horizontal current carried by the layer.

It may be helpful to visualize the TLA as a mathematical limit, $d \to 0$, $\widehat{\sigma} \to \infty$ with $\widehat{\Sigma}$ held fixed. Then $\widehat{\mathcal{J}}$ is a surface current responsible for a discontinuity in the magnetic field. If $\check{\mathbf{b}}(= -\boldsymbol{\nabla}\check{\mathrm{w}})$ is the potential field above the conducting layer,

$$\begin{aligned}\check{\mathbf{b}}(r_o,\theta,\phi) - \widehat{\mathbf{b}}(r_o,\theta,\phi) &= \mu_0\widehat{\mathcal{J}}(\theta,\phi)\times\mathbf{1}_r \\ &= \mu_0\widehat{\Sigma}(\theta,\phi)\widehat{\mathbf{e}}_\mathrm{H}(r_o,\theta,\phi)\times\mathbf{1}_r.\end{aligned} \tag{27e}$$

The potential field does not affect the torque, $\boldsymbol{\Gamma}^M$, on the mantle, although it does contribute to the torque that each Taylor cylinder exerts on the others.

We contrast two proposed conductivity distributions. Buffett et al. (2002) inferred from their studies of nutational resonances that d is only 200 m and that $\widehat{\sigma} = 3 \times 10^5$ S m^{-1}, which is comparable to the core conductivity σ, and gives $\widehat{d}_\eta = 10$ km. The TLA should therefore be excellent in most applications. In contrast, the laboratory experiments of Ohta et al. (2008) suggest $\widehat{\sigma} = 100$ S m^{-1} and $d = 3 \times 10^5$ m; see also Yoshino (2010). This gives $\widehat{d}_\eta = 2 \times 10^6$ m, so it is doubtful if the TLA can be validly applied. The similar conductances of the models ($\widehat{\Sigma} = 3/6 \times 10^7$ S) are insufficient to justify the use of the TLA.

This completes our critique of the basics of torsional wave coupling to the mantle. Some of its consequences are unexpected; but most are not. Even dimensional reasoning leads to

$$\begin{aligned}&\widehat{\Gamma}_z^M = \widehat{\Gamma}_0^M(\overline{\zeta} - \widehat{\zeta}), \\ &\text{where } \widehat{\Gamma}_0^M = O\left(r_o^4\widehat{\Sigma}\mathcal{B}_o^2\right) \approx 4 \times 10^{27}\,\mathrm{Nms},\end{aligned} \tag{28a,b}$$

for $\mathcal{B} = 0.5$mT . Here $\mathcal{B}_o^2$ is an average of $\left(B_r^N\right)^2$ over the CMB, and $\overline{\zeta}$ is defined by:

$$\overline{\zeta}(t) = \frac{1}{s^2\widehat{A}(s)}\int_0^{r_o} s^2\widehat{A}(s)\zeta(s,t)\mathrm{d}s \tag{28c}$$

Perhaps unexpectedly, the boundary layer on the CMB described above reduces $\widehat{\Gamma}_0^M$ by a factor of $\Sigma/(\Sigma + \widehat{\Sigma})$, where Σ is the conductance of the boundary layer, defined by

$$\Sigma = \frac{1}{2}(1 + \imath\varsigma)\sigma d_\eta = (1 + \imath\varsigma)(\sigma/2\mu_0|\omega|)^{1/2}, \tag{28d}$$

and $\varsigma = \mathrm{sgn}(\omega)$. This gives $|\Sigma| \approx 3 \times 10^9$ S, which is comparable with $\widehat{\Sigma}$. Ignoring this factor, the magnetic interaction of mantle and FOC is governed by

$$\widehat{C}d_t\widehat{\zeta} = \widehat{\Gamma}_0^M(\overline{\zeta} - \widehat{\zeta}), \qquad Cd_t\overline{\zeta} = -\widehat{\Gamma}_0^M\left(\overline{\zeta} - \widehat{\zeta}\right), \tag{28e,f}$$

where $C = 9.08 \times 10^{36}$ kg m^2 is the polar moment of inertia of the solidly rotating FOC. These equations provide an estimate of the e-folding time, $\widehat{\tau}_\eta$, taken by mantle conduction to kill ζ and $\widehat{\zeta}$: $\widehat{\tau}_\eta = C\widehat{C}/(C + \widehat{C})\widehat{\Gamma}_0^M \approx 64$ years. This is greater than the time taken by the waves to cross the core, which is $\tau_\mathrm{A} = r_o/V_\mathrm{A} \approx 5.6$ years, for $\mathcal{B} = 2$mT.

If we take $\delta\widehat{\zeta} \approx 3 \times 10^{-12}$s^{-1}, as indicated by the LOD data of the first section above, Equations 28e, f suggest that $\overline{\zeta} - \widehat{\zeta} \approx (\widehat{C} + C)\widehat{\zeta}/C$ is about 2×10^{-11} s^{-1}, so that $r_o(\overline{\zeta} - \widehat{\zeta}) \approx 7 \times 10^{-5}$ m s^{-1}, which is less than, but comparable with, the inferred core surface flow. It also gives $\widehat{\Gamma}_z^M \approx 8 \times 10^{16}$ Nm. This increases to the target torque if we take $\widehat{\Sigma} = 1.2 \times 10^9$ S, but that reduces $\widehat{\tau}_\eta$ to 5.3 years, which is less than τ_A.

This highlights a difficulty that might be called the "magnetic coupling paradox," and quantified by a quality factor:

$$\Pi = \widehat{\tau}_\eta/\tau_\mathrm{A} = (\mathcal{B}/\mathcal{B}_o)^2\left(\mu_0\widehat{\Sigma}V_\mathrm{A}\right)^{-1}. \tag{29}$$

There is a window for $\widehat{\Sigma}$, that may be narrow or nonexistent, in which $\widehat{\Gamma}_z^M$ is large enough to explain variations in LOD by torsional waves, but simultaneously is small enough to ensure that $\Pi > 1$ so that the waves are not over

damped by mantle conduction. According to the admittedly imprecise, order of magnitude estimates made here, the window is nonexistent. For the target torque to be reached or exceeded, $\widehat{\Gamma} \gtrsim 1.2 \times 10^9$ S, but $\Pi > 1$ requires $\widehat{\Gamma} \lesssim 1.1 \times 10^9$ S. See also Dumberry and Mound (2008).

So far the existence of the SIC has been ignored, almost totally. We have however recognized that, for $s < r_i$, two Taylor cylinders exist, $\mathcal{C}^N(s)$ and $\mathcal{C}^S(s)$, in which $\zeta^N(s)$ and $\zeta^S(s)$ may be expected to differ. For simplicity, we assume here that they are equal. To evaluate $\widetilde{\Gamma}_z$, it is necessary to link $\mathbf{b}$ to $\widetilde{\mathbf{b}}$ across a boundary layer strongly influenced by Λ. An analysis of the boundary layer leads to (see RA12)

$$\widetilde{b}_\phi = \mu_0 \widetilde{\sigma} \widetilde{d}_\eta s B_r^N (\overline{\zeta} - \widetilde{\zeta}) \quad \text{on} \quad r = r_i, \tag{30a}$$

where $\widetilde{\zeta}$ is the angular velocity of the SIC, and $\widetilde{d}_\eta = \left(\frac{1}{2}|\omega|\mu_0 \widetilde{\sigma}_i\right)^{-1/2} \approx d_\eta \approx 10$ km. This leads to an expression for $\widetilde{\Gamma}_z^M$, in which the main part that couples to the TC is

$$\widetilde{\Gamma}_z^M = \widetilde{\Gamma}_0^M (\overline{\zeta} - \widehat{\zeta}), \quad \text{where} \quad \widetilde{\Gamma}_0^M = \mathrm{O}\left(r_i^4 \widetilde{\sigma} \widetilde{d}_\eta \mathcal{B}_i^2\right); \tag{30b,c}$$

cf. Equations 28a, b. For $\mathcal{B}_i = 5$ mT, $\widetilde{\Gamma}_0^M \approx 2 \times 10^{29}$ Nms. This large torque acts on the SIC whose moment of inertia is less than $10^{-3}\widehat{C}$. The coupling time, $\widetilde{\tau}_\eta$, is therefore very much less than $\widehat{\tau}_\eta$. Equations analogous to Equation 28a, b give (for $\widetilde{\sigma} = \sigma$)

$$\widetilde{\tau}_\eta \approx \widetilde{C}/|\widetilde{\Gamma}_0^M| \approx 4 \text{ days}. \tag{30d}$$

This is the time taken for a mismatch between ζ and $\widetilde{\zeta}$ to be wiped out by magnetic torques. Clearly the coupling between TC and SIC is substantial at frequencies of order ω_A. This supports the opinion, advanced several times in this review, that on semi-decadal time scales, the TC is effectively locked to the SIC in its rotation about Oz.

Synthesis

In this review we have analyzed the various ways in which Earth's core is coupled to the mantle and have presented estimates of the amplitudes of these couplings in order to show which may plausibly explain the available LOD data. In our first section, we provide observational evidence for core-mantle coupling. We show that Earth's rotation rate has a roughly semi-decadal time variability, such that the LOD fluctuates at the ms level. To explain these LOD fluctuations, an internal coupling must exist between the mantle and the core that provides torques of order 10^{18} Nm, which we named "the target torque."

In the later text, we develop estimates of the strength of the viscous, topographic, gravitational, and electromagnetic torques. Only the viscous torque, Γ_z^V, appears to be too weak to explain the LOD signal. This is true even when we allow for the enhanced coupling that turbulence can provide.

The topographic torque on the mantle, $\widehat{\Gamma}_z^T$, is created by core flow interacting with bumps on the CMB. In analyzing $\widehat{\Gamma}_z^T$, it became clear that exchange of angular momentum with the SIC is significant. Order of magnitude arguments showed that potentially the largest part of $\widehat{\Gamma}_z^T$ is $\widehat{\Gamma}_{a,z}^T$, which is produced by the gravitational field of density anomalies in the mantle and possibly SIC, including bumps on their surfaces. This part of $\widehat{\Gamma}_z^T$ is therefore intimately related to the gravitational torque $\widehat{\Gamma}_z^G$. When the two are treated together as $\widehat{\Gamma}_{a,z}^{G+T}$, there is an equal but opposite torque, $\widetilde{\Gamma}_{a,z}^{G+T}$ on the SIC. Gravitational oscillations (Buffett, 1996) occur when the system is perturbed from a state of minimum gravitational energy in which $\widehat{\Gamma}_{a,z}^{G+T} = \widetilde{\Gamma}_{a,z}^{G+T} = 0$. An oscillation period of $\tau^{\mathrm{G}} = 4.1$ years was derived. If, as seems likely, strong magnetic coupling exists between the tangent cylinder (TC) and the SIC, the gravitational oscillation period increases to $\tau_{\mathrm{TC}}^G = 8.9$ years.

The remaining part of $\widehat{\Gamma}_z^T$ is $\widehat{\Gamma}_{c,z}^T$, and is produced by core convection. Its importance is uncertain. From what is known today, $\Gamma_{c,z}^T$ may be 0 Nm or may exceed the target torque (cf. Kuang and Bloxham, 1997; Hide, 1998; Jault and Le Mouël, 1999; Kuang and Chao, 2001).

A simple model of torsional waves traversing FOC can explain oscillations of period, $\tau \approx 6$ years, but there is a paradox: The target torque cannot be attained by magnetic coupling between the waves and the mantle unless a dimensionless "paradox parameter," Π, defined in Equation 29, is large enough. If this parameter is too large, however, the waves are damped out before they can cross the core. Whether the core can evade the paradox seems uncertain.

The topographic, gravitational and magnetic torques all have significant uncertainties in their amplitudes, but the target torque falls within these uncertainties, i.e., conceivable any of them could explain the semi-decadal LOD signals. The coupling processes may be convolved. The recent model of Buffett et al. (2009) allows for this, but argues that the gravitational torque dominates. In contrast, Gillet et al. (2010) infer that torsional oscillations in the FOC can explain the LOD observations without strong gravitational coupling. Improvements in data and modeling of Earth's rotation (e.g., Gross, 2009), the geomagnetic field (e.g., Hulot et al., 2002; Jackson, 2003), core seismology (e.g., Dai and Song, 2008), and the time-variations in the gravity field (e.g., Velicogna and Wahr, 2006; Dumberry, 2010) will all prove important in testing these core-mantle coupling arguments.

This review has focussed on explaining variations in LOD owing to internal coupling between the mantle and core. This coupling produces changes primarily in the axial angular rotation rate, Ω_z, on semi-decadal time scales. Detailed measurements now exist of variations in Earth's full rotation vector on many time scales (e.g., Gross, 2007), with the different directional components

providing information on different geophysical phenomena (e.g., Mathews et al., 2002). Furthermore, rotation vector and magnetic field measurements now exist for other planets (e.g., Margot et al., 2007; Uno et al., 2009), and will improve in quality in the coming decades. Such measurements will allow the development of models of deep interior structure and dynamics in planetary bodies throughout the solar system (e.g., Tyler, 2008; Noir et al., 2009; Goldreich and Mitchell, 2010).

Acknowledgments

We thank Richard Gross, Richard Holme, and Andrew Jackson for sharing their insights and their data. We are also grateful to Bruce Buffett and the referee (Mathieu Dumberry) for giving helpful advice.

Bibliography

Abarca del Rio, R., Gambis, R., and Salstein, D. A., 2000. Interannual signals in length of day and atmospheric angular momentum, *Annales Geophysicae*, **18**, 347–364.

Alboussière, T., Deguen, R., and Melzani, M., 2010. Melting induced stratification above the Earth's inner core due to convective translation. *Nature*, **466**, 744–747.

Anufriev, A. P., and Braginsky, S. I., 1975. Influence of irregularities of the boundary of the Earth's core on the velocity of the liquid and on the magnetic field. *Geomagnetism and Aeronomy*, **15**, 754–757.

Anufriev, A. P., and Braginsky, S. I., 1977a. Influence of irregularities of the boundary of the Earth's core on the fluid velocity and the magnetic field, II. *Geomagnetism and Aeronomy*, **17**, 78–82.

Anufriev, A. P., and Braginsky, S. I., 1977b. Influence of irregularities of the boundary of the Earth's core on the fluid velocity and the magnetic field, III. *Geomagnetism and Aeronomy*, **17**, 742–750.

Braginsky, S. I., 1970. Torsional magnetohydrodynamic vibrations in the Earth's core and variations in day length. *Geomagnetism and Aeronomy*, **10**, 1–8.

Braginsky, S. I., 1984. Short-period geomagnetic secular variation. *Geophysical and Astrophysical Fluid Dynamics*, **30**, 1–78.

Braginsky, S. I., 1999. Dynamics of the stably stratified ocean at the top of the core. *Physics of the Earth and Planetary Interiors*, **111**, 21–34.

Braginsky, S. I., and Roberts, P. H., 1995. Equations governing convection in Earth's core and the Geodynamo. *Geophysical and Astrophysical Fluid Dynamics*, **79**, 1–97.

Braginsky, S. I., and Roberts, P. H., 2007. Anelastic and Boussinesq approximations. In Gubbins, D., and Herrero-Bervera, E. (eds.), *Encyclopedia of Geomagnetism and Paleomagnetism*. Heidelberg: Springer, pp. 11–19.

Brito, D., Aurnou, J. M., and Cardin, P., 2004. Turbulent viscosity measurements relevant to planetary core-mantle dynamics. *Physics of the Earth and Planetary Interiors*, **141**, 3–8.

Buffett, B. A., 1996. Gravitational oscillations in the length of day. *Geophysical Research Letters*, **23**, 2279–2282.

Buffett, B. A., 1997. Geodynamic estimates of the viscosity of the Earth's inner core. *Nature*, **388**, 571–573.

Buffett, B. A., 1998. Free oscillations in the length of day: inferences on physical properties near the core-mantle boundary. *Geodynamics*, **28**, 153–165.

Buffett, B. A., 2010. Chemical stratification at the top of Earth's core: constraints from nutation observations. *Earth and Planetary Science Letters*, **296**, 367–372.

Buffett, B. A., and Christensen, U. R., 2007. Magnetic and viscous coupling at the core-mantle boundary; inferences from observations of the Earth's nutations. *Geophysical Journal International*, **171**, 145–152.

Buffett, B. A., and Glatzmaier, G. A., 2000. Gravitational braking of inner-core rotation in geo-dynamo simulations. *Geophysical Research Letters*, **27**, 3125–3128.

Buffett, B. A., Mathews, P. M., and Herring, T. A., 2002. Modeling of nutation and precession: effects of electromagnetic coupling. *Journal of Geophysical Research*, **107**, 2070, doi:10.1029/2000JB000056.

Buffett, B. A., Mound, J., and Jackson, A., 2009. Inversion of torsional oscillations for the structure and dynamics of Earth's core. *Geophysical Journal International*, **177**, 878–890.

Dai, W., and Song, X., 2008. Detection of motion and heterogeneity in Earth's liquid outer core. *Geophysical Research Letters*, **35**, L16311.

Davidson, P. A., 2001. *An Introduction to Magnetohydrodynamics*. Cambridge, UK: Cambridge University Press.

Davidson, P. A., 2004. *Turbulence*. Oxford, UK: Oxford University Press.

de Wijs, G. A., Kresse, G., Vočadlo, I., Dobson, D. P., Alfêe, D., Gillan, M. J., and Price, G. D., 1998. The viscosity of liquid iron at the physical conditions of Earth.s core. *Nature*, **392**, 805–807.

Defraigne, P., Dehant, V., and Wahr, J., 1996. Internal loading of an inhomogeneous compressible mantle with phase boundaries. *Geophysical Journal International*, **125**, 173–192.

Deleplace, B., and Cardin, P., 2006. Viscomagnetic torque at the core-mantle boundary. *Geophysical Journal International*, **167**, 557–566.

Dobson, D. P., Crichton, W. A., Vočadlo, I., Jones, A. P., Wang, Y., Uchida, T., Rivers, M., Sutton, S., and Brodhardt, J. P., 2000. In situ measurements of viscosity of liquids in the Fe-FeS system at high pressures and temperatures. *American Mineralogist*, **85**, 1838–1842.

Dormy, E., Roberts, P. H., and Soward, A. M., 2007. Core, boundary layers. In Gubbins, D., and Herrero Bervera, E. (eds.), *Encylopedia of Geomagnetism and Paleomagnetism*. Heidelberg: Springer, pp. 111–116.

Dumberry, M., 2007. Taylor's constraint and torsional oscillations. In Cardin, P., and Cugliandolo, L. F. (eds.), *Dynamos*. Amsterdam: Elsevier, pp. 383–401.

Dumberry, M., 2010. Gravity variations induced by core flows. *Geophysical Journal International*, **180**, 635–650.

Dumberry, M., and Mound, J., 2008. Constraints on core-mantle electromagnetic coupling from torsional oscillation normal modes. *Journal of Geophysical Research*, **113**, B03102, doi:10.1029/2007JB005135.

Elsasser, W. M., 1946. Induction effects in terrestrial magnetism, II. The secular variation. *Physical Review*, **70**, 202–212.

Fearn, D. R., Loper, D. E., and Roberts, P. H., 1981. Structure of the Earth's inner core. *Nature*, **292**, 232–233.

Finlay, C. C., Dumberry, M., Chulliat, A., and Pais, M. A., 2010. Short timescale core dynamics: theory and observations. *Space Science Reviews*, **155**, 177–218, doi:10.1007/s11214-010-9691-6.

Forte, A. M., Woodward, R. J., and Dziewonski, A. M., 1994. Joint inversion of seismic and geo-dynamic data for models of three-dimensional mantle heterogeneity. *Journal of Geophysical Research*, **99**, 21857–21877.

Gargett, A. E., 1984. Vertical eddy diffusivity in the ocean interior. *Journal of Marine Research*, **42**, 359–393.

Gillet, N., Jault, D., Canet, E., and Fournier, A., 2010. Fast torsional waves and strong magnetic field within the Earth's core. *Nature*, **465**(7294), 74–77, doi:10.1038/nature09010.

Glatzmaier, G. A., and Roberts, P. H., 1995. A three-dimensional convective dynamo solution with rotating and finitely

conducting inner core and mantle. *Physics of the Earth and Planetary Interiors*, **91**, 63–75.
Goldreich, P. M., and Mitchell, J. L., 2010. Elastic ice shells and synchronous moons: implications for cracks on Europa and non-synchronous rotation on Titan. *Icarus*, doi:10.1016-/j.icarus.2010.04.013.
Gross, R. S., 2001. A combined length-of-day series spanning 1832–1997: LUNAR97. *Physics of the Earth and Planetary Interiors*, **123**, 65–76.
Gross, R. S., 2007. Earth rotation variations – long period. In Herring, T. A. (ed.), *Physical Geodesy*. Oxford: Elsevier. Treatise on Geophysics, Vol. 3, pp. 239–294.
Gross, R. S., 2009. Ocean tidal effects on Earth rotation. *Journal of Geodynamics*, **48**, 219–225.
Heimpel, M. H., and Aurnou, J. M., 2007. Turbulent convection in rapidly rotating spherical shells: a model for equatorial and high latitude jets on Jupiter and Saturn. *Icarus*, **187**, 540–557.
Hide, R., 1969. Interaction between the earth's liquid core and solid mantle. *Nature*, **222**, 1055–1956.
Hide, R., 1998. A note on topographic core-mantle coupling. *Physics of the Earth and Planetary Interiors*, **109**, 91–92.
Hide, R., and James, I. N., 1983. Differential rotation produced by potential vorticity mixing in a rapidly rotating fluid. *Geophysical Journal of the Royal Astronomical Society*, **74**, 301–312.
Hide, R., Clayton, R. W., Hager, B. H., Speith, M. A., and Voorhies, C. V., 1993. Topographic core-mantle coupling and fluctuations in Earth's rotation. In Aki, K., and Dmowska, R. (eds.), *Relating Geophysical Structures and Processes: The Jeffreys Volume*. Washington, DC: AGU. Geophysical Monograph Series, Vol. 76, pp. 107–120.
Holme, R., 1998. Electromagnetic core-mantle coupling-I. Explaining decadal changes in the length of day. *Geophysical Journal International*, **132**, 167–180.
Holme, R., and de Viron, O., 2005. Geomagnetic jerks and a high-resolution length-of-day profile for core studies. *Geophysical Journal International*, **160**, 435–439.
Hulot, G., Eymin, C., Langlais, B., Mandea, M., and Olsen, N., 2002. Small-scale structure of the geodynamo inferred from Oersed and Magsat satellite data. *Nature*, **416**, 620–623.
Jackson, A., 1997. Time-dependency of tangentially geostrophic core surface motions. *Physics of the Earth and Planetary Interiors*, **103**, 293–311.
Jackson, A., 2003. Intense equatorial flux spots on the surface of Earth's core. *Nature*, **424**, 760–763.
Jacobs, J. A., 1953. The Earth's inner core. *Nature*, **172**, 297–298.
Jault, D., 2003. Electromagnetic and topographic coupling, and LOD variations. In Jones, C. A., Soward, A. M., and Zhang, K. (eds.), *Earth's Core and Lower Mantle*. London: Taylor and Francis, pp. 46–76.
Jault, D., and Le Mouël, J. L., 1989. The topographic torque associated with a tangentially geostrophic motion at the core surface and inferences on the flow inside the core. *Geophysical and Astrophysical Fluid Dynamics*, **48**, 273–296.
Jault, D., and Le Mouël, J. L., 1999. Comment on 'On the dynamics of topographic core-mantle coupling' by Weijia Kuang and Jeremy Bloxham. *Physics of the Earth and Planetary Interiors*, **114**, 211–215.
Jault, D., Gire, C., and LeMouel, J.-L., 1988. Westward drift, core motions and exchanges of angular momentum between core and mantle. *Nature*, **333**, 353–356.
Kawai, K., and Tsuchiya, T., 2009. Temperature profile in the lowermost mantle from seismological and mineral physics joint modeling. *Proceedings of the National Academy of Sciences of the United States of America*, doi:10.1073/pnas.0905920106.
Kuang, W.-J., and Bloxham, J., 1993. The effect of boundary topography on motions in the Earth's core. *Geophysical and Astrophysical Fluid Dynamics*, **72**, 161–195.
Kuang, W.-J., and Bloxham, J., 1997. On the dynamics of topographic core-mantle coupling. *Physics of the Earth and Planetary Interiors*, **99**, 289–294.
Kuang, W.-J., and Chao, B. F., 2001. Topographic core-mantle coupling in geodynamo modeling. *Geophysical Research Letters*, **28**, 1871–1874.
Loper, D. E., 2007. Turbulence and small-scale dynamics in the core. In Olson, P. L. (ed.), *Core Dynamics*. Amsterdam: Elsevier. Treatise on Geophysics, Vol. 8, pp. 187–206.
Love, J. J., and Bloxham, J., 1994. Electromagnetic coupling and the toroidal magnetic field at the core-mantle boundary. *Geophysical Journal International*, **117**, 235–256.
Margot, J. L., Peale, S. J., Jurgens, R. F., Slade, M. A., and Holin, I. V., 2007. Large longitude libration of Mercury reveals a molten core. *Science*, **316**, 710–714.
Mathews, P. M., Herring, T. A., and Buffett, B. A., 2002. Modeling of nutation and precession: new nutation series for nonrigid Earth and insights into the Earth's interior. *Journal of Geophysical Research*, **107**, 2068, doi:10.1029/2001JB000390.
Monnereau, M., Calvet, M., Margerin, L., and Souriau, A., 2010. Lopsided growth of Earth's inner core. *Science*, **328**, 1014–1017.
Morse, S. A., 1986. Adcumulus growth of the inner core. *Geophysical Research Letters*, **13**, 1466–1469.
Mound, J. E., and Buffett, B. A., 2003. Interannual oscillations in length of day: implications for the structure of the mantle and core. *Journal of Geophysical Research*, **108**, 2334, doi:10.1029/2002JB002054.
Mound, J. E., and Buffett, B. A., 2005. Mechanisms of core-mantle angular momentum exchange and the observed spectral properties of torsional oscillations. *Journal of Geophysical Research*, **110**, B08103, doi:10.1029/2004JB003555.
Mound, J., and Buffett, B., 2006. Detection of a gravitational oscillation in length-of-day. *Earth and Planetary Science Letters*, **243**, 383–389.
Müller, U., and Bühler, L., 2001. *Magnetofluiddynamics in Channels and Containers*. Heidelberg: Springer.
Noir, J., Hemmerlin, F., Wicht, J., Baca, S. M., and Aurnou, J. M., 2009. An experimental and numerical study of librationally driven flow in planetary cores and subsurface oceans. *Physics of the Earth and Planetary Interiors*, **173**, 141–152.
Ohta, K., Onada, S., Hirose, K., Sinmyo, R., Shimizu, K., Saya, N., Ohishi, Y., and Yasuhara, A., 2008. The electrical conductivity of post-perovskite in Earth's D″ layer. *Science*, **320**, 89–91.
Olsen, N., and Mandea, M., 2008. Rapidly changing flows in the Earth's core. *Nature Geoscience*, **1**, 390–394.
Roberts, P. H., and Aurnou, J. M., 2012. On the theory of core-mantle coupling. *Geophysical and Astrophysical Fluid Dynamics* (to appear).
Roberts, P. H., and Soward, A. M., 1972. Magnetohydrodynamics of the Earth's core. *Annual Review of Fluid Mechanics*, **4**, 117–154.
Roberts, P. H., Yu, Z. J., and Russell, C. T., 2007. On the 60-year signal from the core. *Geophysical and Astrophysical Fluid Dynamics*, **43**, 321–330.
Rogers, T. M., and Glatzmaier, G. A., 2006. Angular momentum transport by gravity waves in the solar interior. *Geophysical and Astrophysical Fluid Dynamics*, **653**, 756–764.
Schubert, G., Turcotte, D. L., and Olson, P., 2001. *Mantle Convection in the Earth and Planets*. Cambridge, UK: Cambridge University Press.
Sprague, M., Julien, K., Knobloch, E., and Werne, J., 2006. Numerical simulation of an asymptotically reduced system for rotationally constrained convection. *Journal of Fluid Mechanics*, **551**, 141–174.
Stellmach, S., and Hansen, U., 2004. Cartesian convection driven dynamos at low Ekman number. *Physical Review E*, **70**, 056312.

Stix, M., and Roberts, P. H., 1984. Time-dependent electromagnetic core-mantle coupling. *Physics of the Earth and Planetary Interiors*, **36**, 49–60.
Tanaka, S., 2010. Constraints on the core-mantle boundary topography from *P4KP-PcP* differential travel times. *Journal of Geophysical Research*, **115**, B04310, doi:10.1029/2009JB006563.
Taylor, J. B., 1963. The magnetohydrodynamics of a rotating fluid and the Earth's dynamo problem. *Proceedings. Royal Society of London*, **A274**, 274–283.
Tyler, R. H., 2008. Strong ocean tidal flow and heating on moons of the outer planets. *Nature*, **456**, 770–773.
Uno, H., Johnson, C. L., Anderson, B. J., Korth, H., and Solomon, S. C., 2009. Modeling Mercury's internal magnetic field with smooth inversions. *Earth and Planetary Science Letters*, **285**, 328–339.
Velicogna, I., and Wahr, J., 2006. Acceleration of Greenland ice mass loss in spring 2004. *Nature*, **443**, 329–331.
Vočadlo, I., Alfè, D., Price, G. D., and Gillan, M. J., 2000. First principles calculation of the diffusivity of FeS at experimentally accessible conditions. *Physics of the Earth and Planetary Interiors*, **120**, 145–152.
Wahr, J., and deVries, D., 1989. The possibility of lateral structure inside the core and its implications for nutation and Earth tide observations. *Geophysical Journal International*, **99**, 511–519.
Wahr, J., Swenson, S., and Velicogna, I., 2006. Accuracy of GRACE mass estimates. *Geophysical Research Letters*, **33**, L06401, doi:10.1029/2005GL025305.
Wicht, J., and Christensen, U. R., 2010. Torsional oscillations in dynamo simulations. *Geophysical Journal International*, **181**, 1367–1380.
Yoshida, S., Sumita, I., and Kumazawa, M., 1996. Growth model of the inner core coupled with outer core dynamics and the resulting elastic anisotropy. *Journal of Geophysical Research*, **101**, 28085–28103.
Yoshino, T., 2010. Laboratory electrical conductivity measurement of mantle minerals. *Surveys in Geophysics*, **31**, 163–206, doi:10.1007/s10712-009-9084-0.

Cross-references

Core Dynamo
Earth's Structure, Lower Mantle
Energy Budget of the Earth
Geomagnetic Field, Theory

CRUSTAL REFLECTIVITY (OCEANIC) AND MAGMA CHAMBER

Satish C. Singh
Laboratoire de Géoscience Marines, Institut de Physique du Globe de Paris, Paris, France

Synonyms

Melt lens; Spreading center and ridge

Definition

Axial magma chamber (*Melt lens*) is a thin melt lens observed at ocean spreading centers.
Layer 2A or *Lava* is the top layer of oceanic igneous crust.
Layer 2B is a dike sequence and lies above the axial melt lens.
Layer 3 (*gabbro*) forms the lower oceanic crust.
Moho is a boundary between the crust and mantle.
Pg is a seismic ray that travels through the crust.
PmP is a reflection from the crust–mantle boundary.
Pn is a ray that travels in the upper mantle.
Tomography is a technique to image the velocity structure of the earth.

Introduction

Over 70% of the earth's crust is formed by the cooling and crystallization of melt at ocean spreading centers, which represent over 55,000 km of chains of volcanoes in the middle of the oceans, called mid-ocean ridges. At ocean spreading centers, the oceanic plate separates causing the mantle to move upward, reducing the pressure and causing the melting of the mantle. Since the newly formed melt is lighter than the surrounding mantle material, it moves upward toward the surface of the earth. Part of the melt is erupted on the seafloor as lava, which cools very rapidly forming a cap of solid extrusive layer, also known as Layer 2A (Figure 1). As there is a significant amount of water present at mid-ocean ridges, the water circulates deep in the crust. Therefore, the melt stays mainly in the middle of the crust and erupts along thin dikes. When these dikes are cooled and crystallized, they form a thick intrusive layer or Layer 2B. Below the dikes, the melt could reside for a long period, forming a steady state melt lens, called axial melt lens or axial magma chamber (AMC). The magma cools and crystallizes in this melt lens, forming a crystalline lower crust. The melt lens forms the lower limit for further penetration of water, and therefore, partial melt is generally present beneath the melt lens down to the crust–mantle boundary. Sometimes hot melt ascending from the mantle may get injected in this partially molten region. Based on this basic process, the oceanic crust is divided into three layers, lava (extrusive), dikes (intrusive), and gabbroic crust. The relative

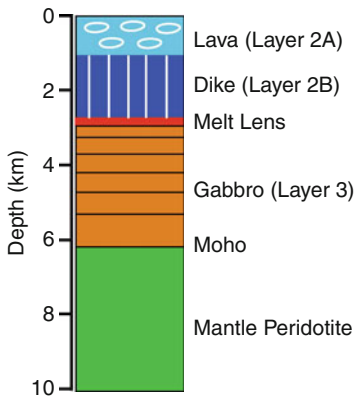

Crustal Reflectivity (Oceanic) and Magma Chamber, Figure 1 Classical model of the oceanic crust. Layers 2A and 2B form the upper crust whereas the gabbro layer corresponds to the lower crust.

thicknesses of these layers depend on the spreading rate, which can vary from a few millimeters up to 200 mm per year.

Based on the spreading rate, mid-ocean ridges are divided into four groups: fast, intermediate, slow, and ultraslow. East Pacific Rise (EPR) is a fast spreading center, where the spreading rate varies from 70 to 180 mm per year (Figure 2). Juan de Fuca Ridge and Valu Fa Ridge are intermediate spreading centers, where the spreading rate varies from 55 to 70 mm per year. Mid-Atlantic Ridge and Central Indian Ridge are slow spreading centers with spreading rates of 20–55 mm per year. South-West Indian Ridge and Gakkel Ridge are ultraslow spreading centers with spreading rates of less than 20 mm per year. The melt production depends on the spreading rate and, therefore, the crustal thickness also varies from 3.5 to 8 km, with an average thickness of 6 km.

Methods

There are two main methods to study the oceanic crustal structures: seismic refraction or tomography and reflection methods. In seismic refraction method, a set of ocean bottom seismometers (OBS) are placed on the seafloor and an array of air guns is used to generate acoustic energy that travels through water column into the crust and mantle and is recorded on OBS (Figure 3). There are three types of waves that arrive on an OBS: waves that travel in the crust (Pg) and the mantle (Pn) and waves reflected from the crust–mantle boundary, Moho (PmP). The travel times of arrivals of energy on these OBS are used to determine the velocity structure of the crust and upper mantle. Since OBS are small in numbers, they are placed 5–20 km apart on the seafloor, and hence provide a very large-scale (5–10 km) velocity structure of the crust. Since the compressional (P) waves travel fast, they arrive first on OBS, and hence mainly P-wave velocities are estimated using OBS data. However, sometimes secondary (S) arrivals, converted phases Ps, are recorded on these OBS and provide information on S-wave velocity.

Seismic reflection method is most commonly used to obtain crustal reflectivity. A streamer containing pressure sensors (hydrophones) is towed behind a vessel recording seismic energy generated by an array of air guns as the vessel moves at 4.5–5 knots (Figure 3). The length of the streamer varies from a few hundred meters up to 15 km (Singh et al., 2009), and hydrophones are generally spaced at 12.5 m. For crustal imaging the air gun shot spacing is ~50 m. Depending upon the target depth, the recording length varies from 10 to 20 s (20–60 km depth). This technique is routinely used for oil and gas exploration,

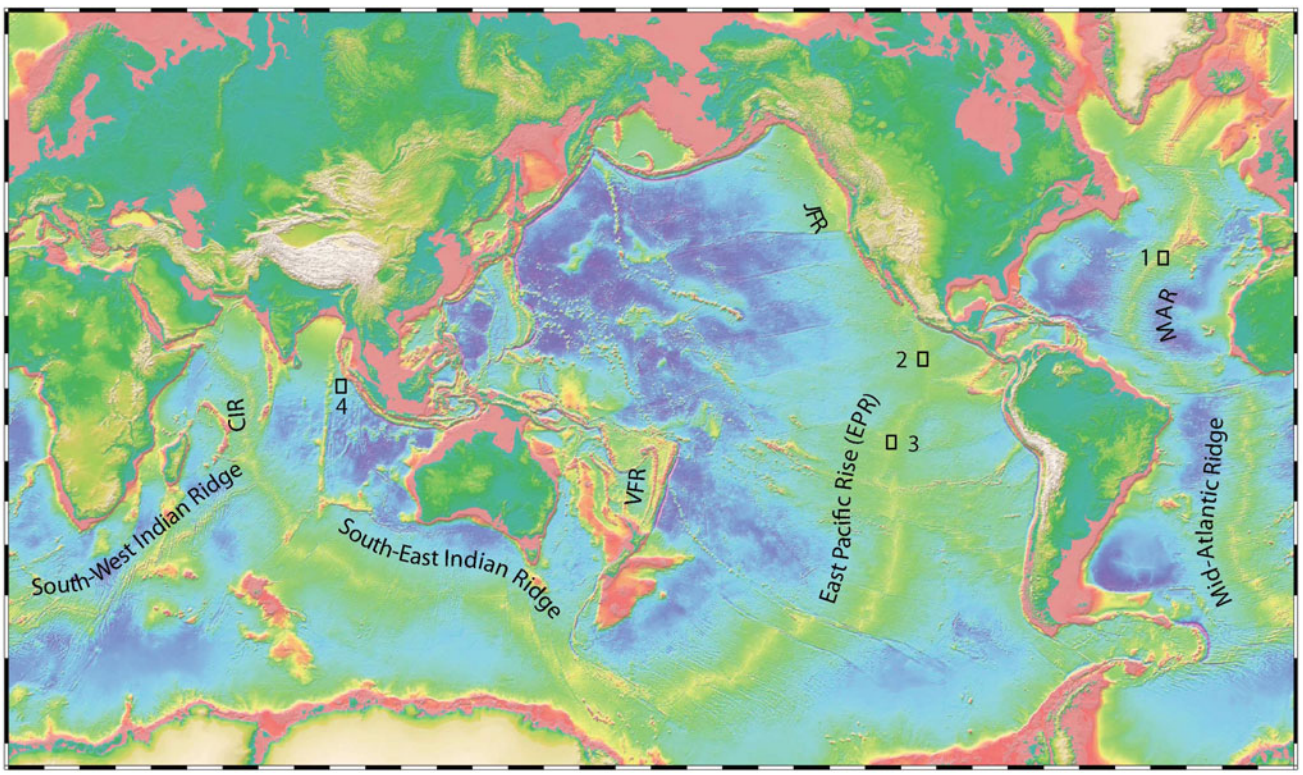

Crustal Reflectivity (Oceanic) and Magma Chamber, Figure 2 Major spreading centers on the earth. JFR – Juan de Fuca Ridge; VFR – Valu Fa Ridge; CIR – Central Indian Ridge. The *rectangles* indicate the positions of data/results shown in this entry: 1 – Lucky Strike Segment at Mid-Atlantic Ridge (Figures 5, 7, 9, and 12); 2 – 9° N East Pacific Rise (Figures 8, 11, and 14); 3 – 14° S East Pacific Rise (Figures 6, 10, and 13); and 4 – Wharton basin (Figures 15 and 16).

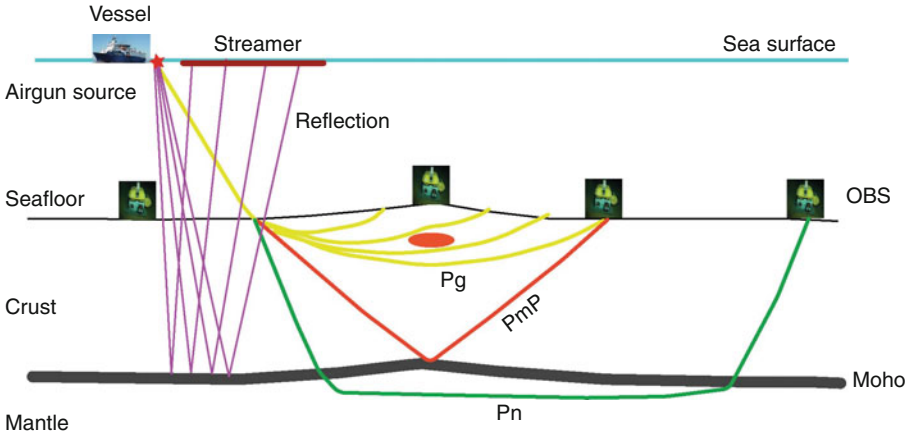

Crustal Reflectivity (Oceanic) and Magma Chamber, Figure 3 Schematic diagram showing the seismic reflection and refraction survey to study the oceanic crust. *Red star* indicates the air gun source. OBS – ocean bottom seismometers; Pg – crustal arrival; Pn – mantle arrival; and PmP – reflection from the crust–mantle boundary. *Red ellipse* indicates melt lens.

and has become a standard technique for crustal studies. There are standard tools to analyze these data. Since the source receiver distance is small as compared to the depth of the target, the data are initially presented as a function of time, and then are depth-converted using velocities obtained from the OBS study or from other sources.

Crustal structure at fast spreading centers

Based on seismic refraction and reflection studies at fast spreading centers and on ophiolites from Oman, the crust at fast spreading centers is considered as a layer cake and is divided into three distinct layers: Layer 2A (pillow lava), Layer 2B (dike sequence), and Layer 3 (gabbro) (Figure 4). The velocity in Layer 2A varies from 2.5 to 4.5 km/s, that in Layer 2B from 4.5 to 6 km/s, and in gabbro from 6 to 7 km/s. On the ridge axis, a magma chamber is generally present between the dike and the gabbro layer.

The structure of Layer 2A is inferred either using the velocity from OBS study or from the reflection method. The boundary between Layer 2A and 2B is not sharp but there is a high velocity gradient where the velocity increases from 2.5 to 4–4.5 km/s in a thin transition zone, which leads to three arrivals (triplication) from Layer 2A (Figure 5). However, since the first arrival tomography is performed on OBS data, spaced at 5–10 km distance, one can only get a smooth velocity of the crust. Therefore, a velocity contour of 4.5 km/s is generally used at the base of Layer 2A (Figure 4, *dashed curve*).

In seismic reflection data, the triplication from the Layer 2A/2B boundary lies in a narrow offset range at intermediate offsets, depending on the water depth and the thickness of Layer 2A (Figure 5) (Harding et al., 1993; Seher et al., 2010a). Since the cusp of triplication has strong amplitude, it can be used to image the base of Layer 2A, and leads to a very nice image of Layer 2A. Since the energy lies in a limited offset range, the two-way travel time for these images varies depending on the

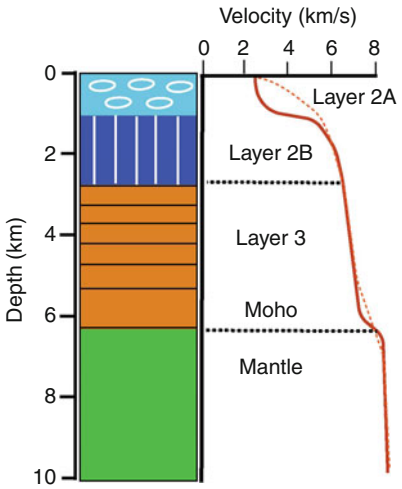

Crustal Reflectivity (Oceanic) and Magma Chamber, Figure 4 Average one-dimensional velocity of oceanic crustal layers and mantle (*solid brown line*). *Thin dashed line* indicates velocity determined using tomographic type techniques.

velocity used for stacking. This becomes particularly important when the thickness map needs to be prepared from 3D seismic reflection data or compared along long profiles. In order to objectively compare Layer 2A thickness, a constant velocity that provides the best image of Layer 2A is used to stack Layer 2A arrival and the two-way travel time is converted into depth using the tomographic velocity obtained using either OBS data or streamer tomography (Seher et al., 2010a).

Plot triplication

Figure 6 shows the image of Layer 2A obtained along the southern East Pacific Rise (Kent et al., 1994). The thickness of the layer varies from ~200 m on the ridge axis

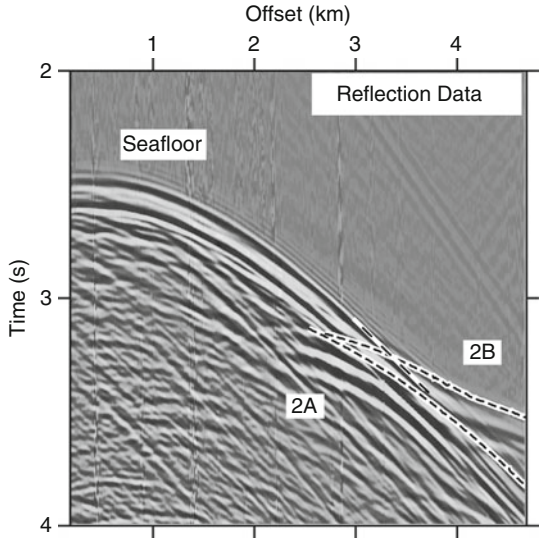

Crustal Reflectivity (Oceanic) and Magma Chamber, Figure 5 Seismic reflection from the Lucky Strike Segment of Mid-Atlantic Ridge showing triplication (*dashed curve*) from Layer 2A/2B boundary (modified from Seher et al., 2010a).

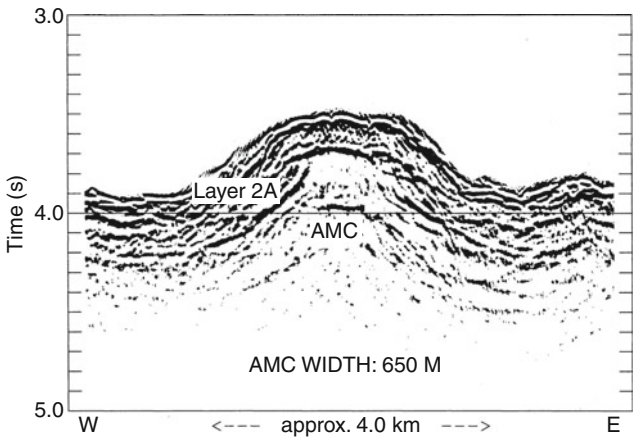

Crustal Reflectivity (Oceanic) and Magma Chamber, Figure 6 Seismic reflection image of Layer 2A and axial magma chamber at 14° S East Pacific Rise (Position 3 in Figure 2) (from Kent et al., 1994). The Layer 2A thickness varies from 200 m on the ridge axis to 400 m off-axis.

and increases to 600 m off-axis (Kent et al., 1994; Harding et al., 1993). The thickening of Layer 2A off-axis could be associated with the accumulation of lavas away from the ridge axis. On slow spreading ridges, Layer 2A could be up to 1 km thick (Singh et al., 2006a; Seher et al., 2010a). Instead of thickening of Layer 2A away from the spreading center, its thickness decreases, which could be due to thinning by stretching (faulting) of the crust (Figure 7). In fact, the thinnest (300 m) Layer 2A at the Lucky Strike segment is observed near the Median bounding faults (Seher et al., 2010a).

There is still debate about the causes of Layer 2A reflection: it could be due to pillow lava and dike boundary as shown in Figure 4 or due to alteration front associated with hydrothermal circulation or pressure collapse boundary (Christeson et al., 2007).

Below Layer 2A, the velocity increases from 4.5 up to 6 km/s, corresponding to dike sequence, below which a magma chamber reflection might be present. The thickness of the dike sequence is ~1.5 km on a fast spreading center (Vera et al., 1990) and up to 2 km on a slow spreading center (Seher et al., 2010b).

Axial magma chamber (melt lens)

On a fast spreading center, the axial magma chamber (AMC) reflector marks the boundary between the upper crust (lava and dikes) and the lower crust (gabbro). It is observed along a significant part of the fast spreading axis at 1.5–2 km below the seafloor. The width of the AMC varies from a few hundred meters to 4.5 km (Kent et al., 1993). The largest melt lens is observed beneath 9° N overlapping spreading center at the East Pacific Rise (Kent et al., 2000; Singh et al., 2006a) (Figure 8). Recently, Canales et al. (2009) have imaged an off-axis melt lens. A 3D seismic reflection study of the 9° N EPR suggests that there might be an extensive presence of melt sills off-axis (Carton et al., 2009).

The AMC have also been observed beneath intermediate spreading centers such as Juan de Fuca Ridge (Canales et al., 2006) and Valu Fa Ridge (Collier and Sinha, 1990). They are generally observed about 3 km below the seafloor. It has been difficult to image AMC reflection on slow spreading ridges, which has been due to strong scattering on the seafloor and complex 3D bathymetry. Using 3D seismic reflection technique, Singh et al. (2006b) discovered AMC beneath the Lucky Strike segment of the Mid-Atlantic Ridge (Figure 9). The AMC is about 3 km wide and 7 km long at ~3 km below the seafloor.

The thickness of the melt lens is difficult to determine. Forward modeling of seismic reflection data from 9° N at EPR suggests that it could be 50–100 m thick (Kent et al., 1993). Seismic full waveform inversion of data from two locations at the EPR suggests that it should be 50–60 m thick (Collier and Singh, 1997; Singh et al., 1998, 1999). Using full waveform of seismic reflection data from 14° S at EPR, Singh et al. (1999) found that a 60 m thick melt lens is overlain by a 60 m thick solid roof and underlain by a 200 m thick solid floor. Above the roof layer, they find a 200 km thick low velocity layer, which they associate with the presence of hydrothermal circulation (Singh et al., 1999) (Figure 10). The roof layer could be the transition zone between the hot melt (1,200°C) below and the hydrothermal layer (400°C) above.

The presence of a solid floor suggests that magma cools and crystallizes in the melt lens and forms the solid floor. Using 3D seismic reflection data, we can image the base of the melt lens. Here the melt lens is about 4.5 km wide and could be up to 250 m thick (as compared to

50–100 m observed elsewhere). This could be due to its very large size (4.5 km) and the presence of low velocity underneath it (Bazin et al., 2003). Singh et al. (2006a) suggest that up to 40% melt could be present between 1.5 and 6 km depth, making it the largest observed melt lens in the crust observed on the earth so far (Figure 11).

Using full waveform and partial stacking technique of seismic reflection data, Singh et al. (1998) show that the melt along 14° S EPR consists of 2–4 km long pure melt zones at 15–20 km interval along the ridge axis (Figure 10). They associate pure melt region where the shear wave velocity is nearly zero and partial melt zone where the shear wave velocity is nonzero (Taylor and Singh, 2002). They suggest that a pure melt region corresponds to fresh supply of magma from the mantle and a partial melt region corresponds to cooled and crystal-

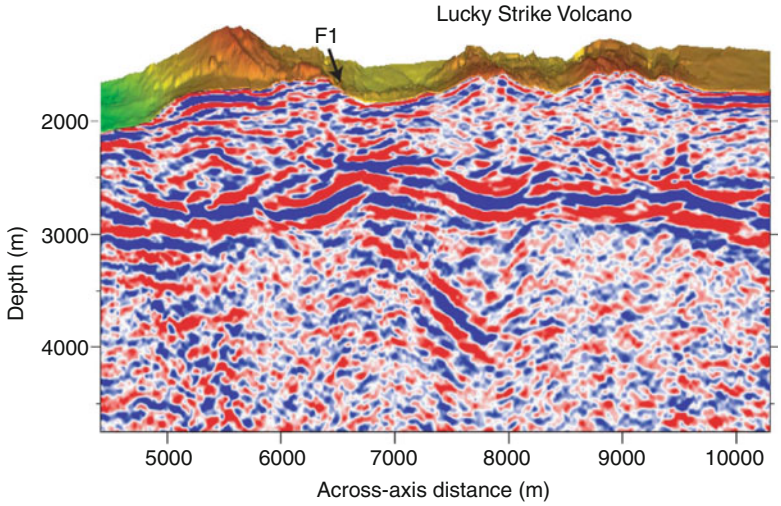

Crustal Reflectivity (Oceanic) and Magma Chamber, Figure 7 Seismic reflection of Layer 2A beneath the Lucky Strike volcano at slow spreading Mid-Atlantic Ridge (Position 1 in Figure 2). F1 indicates an active fault. Layer 2A is thick beneath the ridges and thin beneath the fault.

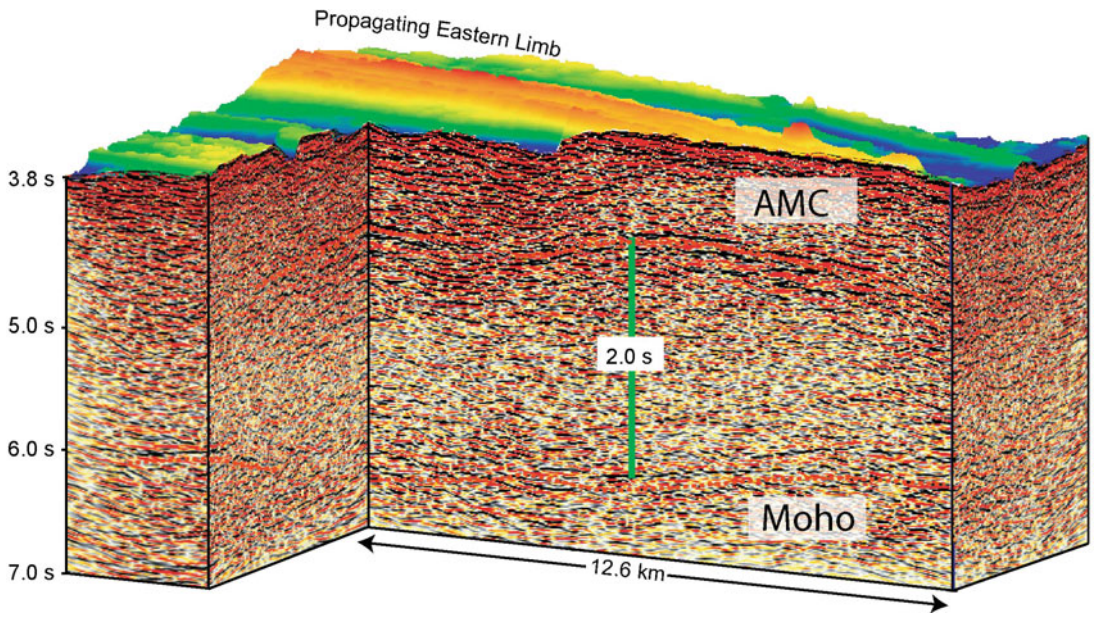

Crustal Reflectivity (Oceanic) and Magma Chamber, Figure 8 Seismic reflection image of axial magma chamber (AMC) and Moho reflection at 9° N overlapping spreading center at the East Pacific Rise (Position 2 in Figure 2) (modified from Singh et al., 2006a).

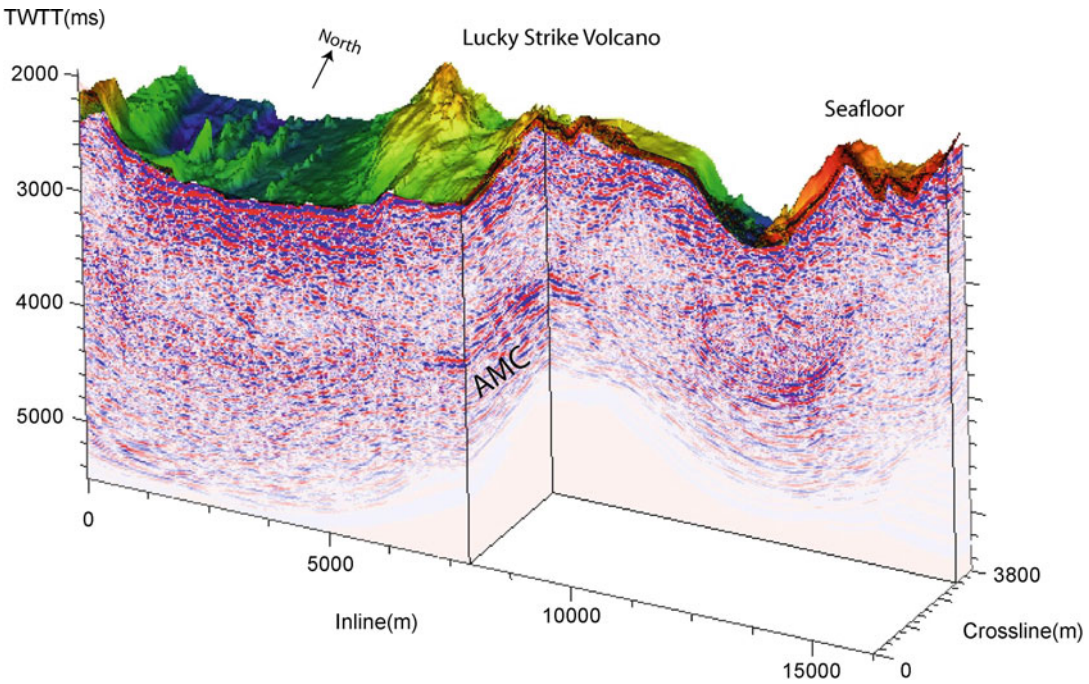

Crustal Reflectivity (Oceanic) and Magma Chamber, Figure 9 Axial magma chamber reflection image from the Lucky Strike Segment of the Mid-Atlantic Ridge (Position 1 in Figure 2).

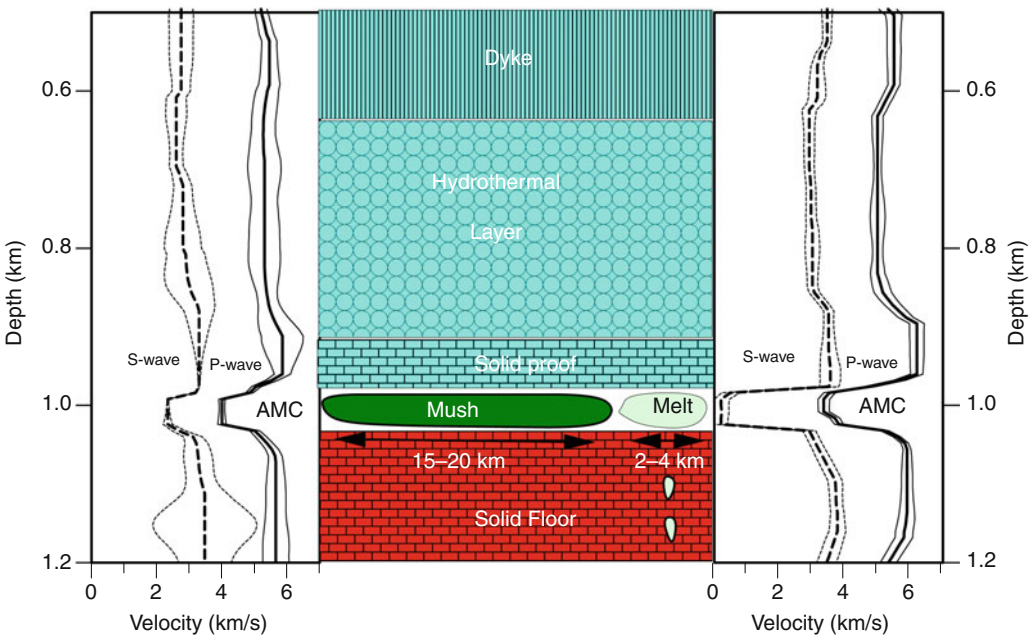

Crustal Reflectivity (Oceanic) and Magma Chamber, Figure 10 Full waveform inversion results at two different locations along the 14° S EPR (Position 3 in Figure 2). Inversion results show the presence of 60 m AMC, 60 m thick roof, and 200 m thick floor of the AMC. It also shows a hydrothermal layer above the roof of the AMC. The result on the *left panel* corresponds to a partial melt region (less than 50% of liquid melt) whereas that on the *right* corresponds to a pure melt (more than 80% of liquid) region. The depth is from the seafloor (modified from Singh et al., 1999).

lized state of melt lens. They also find that a pure melt region is associated with hydrothermal activities on the seafloor, linking the supply of magma from the mantle with hydrothermal circulation on the seafloor. In order for the melt lens to be in steady state, it would require a supply of magma from the mantle every 30 years as it will take 50 years to completely solidify a 50 m thick melt lens (Singh et al., 1999).

Lower crust

So far, no other crustal melt lenses have been observed beneath the axial melt lens. Therefore, only tomographic methods using OBS data are used to determine the velocity structure of the lower crust. Using two-ship expanding spread profile, Vera et al. (1990) and Harding et al. (1989) found that the velocity in the lower crust (5.5–6 km/s) on-axis was lower than that off-axis (6.8–7 km/s), which suggested the presence of partial melt in the lower crust. Using 3D tomography technique, Toomey et al. (1990) and Dunn et al. (2000) showed the presence of low velocity in the lower crust, suggesting the presence of partial melt. Singh et al. (2006b) found a large anomaly in two-way travel time between the Moho reflection and AMC and suggest that up to 40% of melt might be present in the lower crust (Figure 8). A low velocity anomaly has also been observed beneath the Lucky Strike segment of the Mid-Atlantic Ridge beneath the melt lens (Seher et al., 2010c; Singh et al., 2006b). These results suggest that partial melt is present in the lower crust beneath the melt lens (Figure 12).

Based on the study of Oman ophiolite, Kelemen et al. (1997) and Boudier et al. (1996) suggested that the lower crust is formed by injection of melt sills in the lower crust instead of cooling and crystallization of magma in the upper crustal melt sill. However, no melt lenses have been imaged in the lower crust so far, even using 3D seismic reflection technique (Singh et al., 2006a), which suggest that the melt in the lower crust must be in small pockets, not in large melt sills.

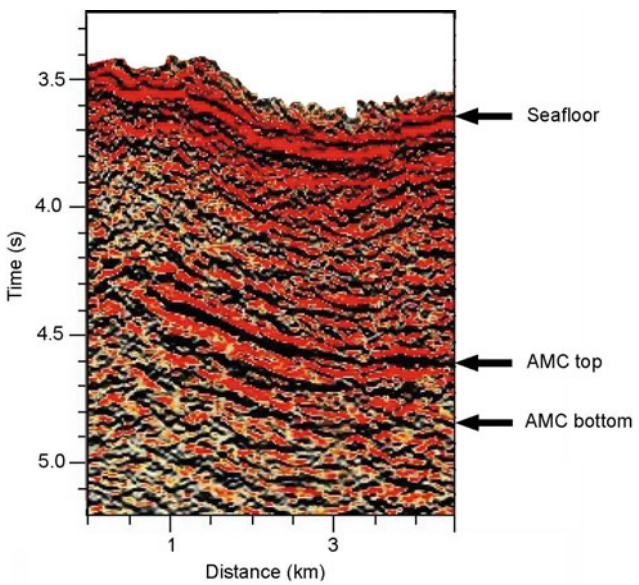

Crustal Reflectivity (Oceanic) and Magma Chamber, Figure 11 Seismic reflection image showing the top and bottom of the axial magma chamber at 9° N EPR (Position 2 in Figure 2).

Oceanic Moho

The Moho is a boundary between the crust and mantle, where the velocity changes from 6.8–7.0 km/s to 7.8–8.1 km/s. For a sharp boundary, a clear Moho reflection is observed. However, the Moho is not just a simple boundary. Kent et al. (1994) identified three types of Moho reflection: (1) Impulsive Moho where a clear single reflection is observed (Figure 13), (2) Diffuse Moho where reflection from Moho is patchy, and (3) Shingled Moho where reflection is shingled.

Moho reflections are generally observed away from the spreading center, not beneath the melt lens. This is because the upper crustal melt lens and associated lower crustal melt would attenuate seismic energy and hence, it would be difficult to image Moho using conventional seismic reflection techniques. Secondly, it was accepted that Moho is formed away from the ridge axis. However, using 3D seismic reflection technique, Singh et al. (2006a) have imaged Moho beneath the wide axial melt lens (Figure 14), suggesting the Moho is formed at zero age.

Moho reflections are observed ~2 s two-way travel time below the seafloor. The average crustal velocity is about 6 km/s, and hence the average crustal thickness is about 6 km. However, Singh et al. (2011) have observed Moho reflection 1.3 s below the seafloor offshore NW

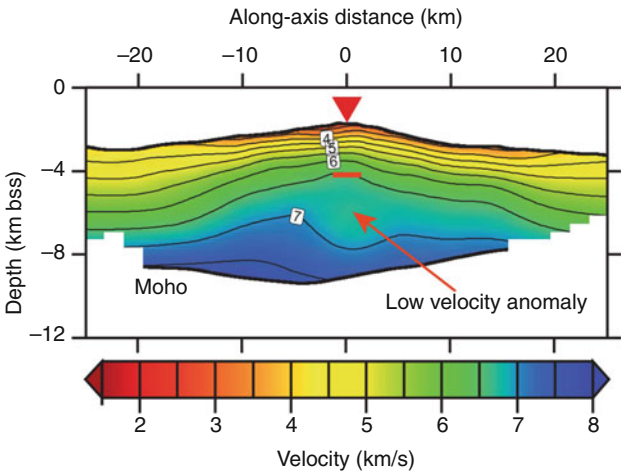

Crustal Reflectivity (Oceanic) and Magma Chamber, Figure 12 Tomographic results from the Lucky Strike Segment of the Mid-Atlantic Ridge (Position 1 in Figure 2) showing melt lens (*red line*), low velocity in the lower crust, and Moho across the ridge axis. The inverse triangle is the center of the ridge axis (modified from Seher et al., 2010c).

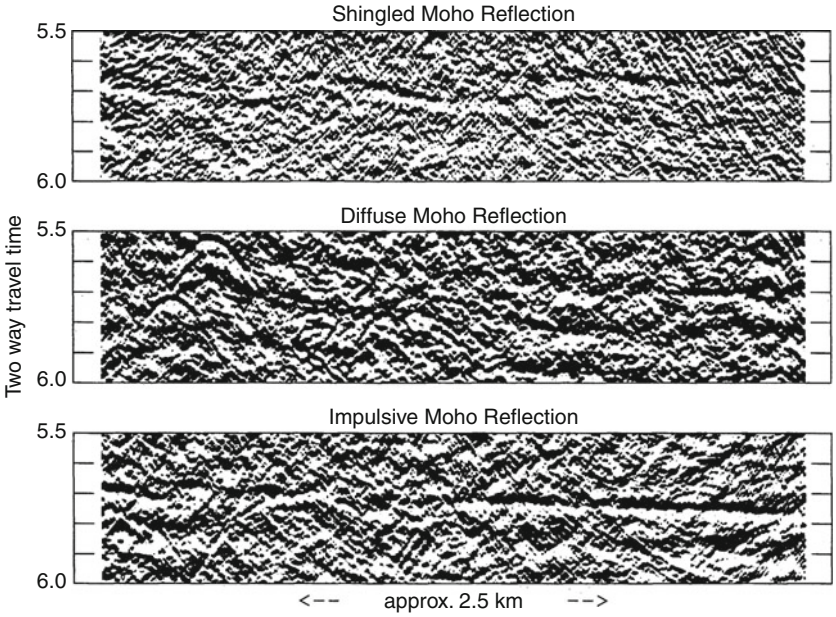

Crustal Reflectivity (Oceanic) and Magma Chamber, Figure 13 Different types of reflection for Moho boundary observed at Southern East Pacific Rise (Position 3 in Figure 2) (Kent et al., 1994). *Top*: Shingled Moho, *Middle*: Diffuse Moho, *Bottom*: Impulsive Moho.

Sumatra, where the crust was formed at the fast spreading Wharton ridge about 55 Ma ago. If we assume an average velocity of 6.0 km/s, which means at the crust there is only 3.5 km thick, it would be the thinnest crust ever observed in a fast spreading environment (Figure 15).

Since there is a positive velocity contrast at the crust–mantle boundary, large amplitude critical angle reflections (PmP) are generated that arrive at large offsets (15–30 km), and are recorded on OBS. These data are then used to map the Moho structure. However, there are two problems in using arrival times of PmP arrivals. The velocity gradient in the lower crust is very small or close to zero, and therefore rays that sample the lower crust do not turn in the lower crust making it difficult to estimate velocity in this zone. Since the arrival time of PmP arrival depends on the velocity in the crust, particularly the lower 3 km of the crust, it is difficult to estimate both the velocity in the lower crust and the Moho structure. Since the velocity in the lower crust can be approximated to a large extent ~6.8 km/s, these data provide a reasonable constrain on the Moho structure, and are routinely used. Secondly, the OBS spacing is generally 5–20 km and the lateral resolution of the Moho structure is very poor.

Crustal thickness

Once we determine the velocity in the crust and Moho structure, we can estimate the crustal thickness. So far, most of the crustal thickness estimations are based on wide-angle seismic studies, and there are significant uncertainties in crustal thickness estimations for the reason explained above. However, combined analyses of seismic reflection, refraction, and gravity data suggest that wide-angle estimation of the crustal thickness can be very reliable.

The crust formed at fast spreading centers is generally uniform and 6 km thick (White et al., 1992; Eittreim et al., 1994) but some variations (5–8 km) have been observed recently (Canales et al., 2003; Singh et al., 2006a; Barth and Mutter, 1996). There is no significant crustal thickness variation across the fracture zone in a fast spreading environment, where it is also 5.5–6 km thick (van Avendonk et al., 2001). The crust formed at slow spreading centers is generally thick at the center of the segment (6–7 km) and thin at segment ends (4–5 km) (Barclay et al., 1998; Seher et al., 2010b). The crust beneath fracture zones in a slow spreading environment is generally thin (3–4.5 km) (Detrick et al., 1993). The thinnest crust (3.5–4.5 km) is formed at ultraslow spreading centers (Jokat and Schmidt-Aursch, 2007). These observations suggest that the thickness of the crust depends on the spreading rate and melt distribution in the crust. On the other hand, thicker crusts are found beneath large igneous provinces, across hotspot tracks or at the interaction of plume and ridges, which are believed to be formed by higher mantle temperatures due to the presence of a plume (e.g., Parkin and White, 2008; Watts et al., 1985; Charvis et al., 1999; Grevemeyer et al., 2001). For example, the crust beneath Iceland could be up to 30 km thick, and beneath La Reunion Island it is 13 km (Charvis et al., 1999).

However, anomalously thin crust has been reported. A 5 km thick crust is observed near the South American

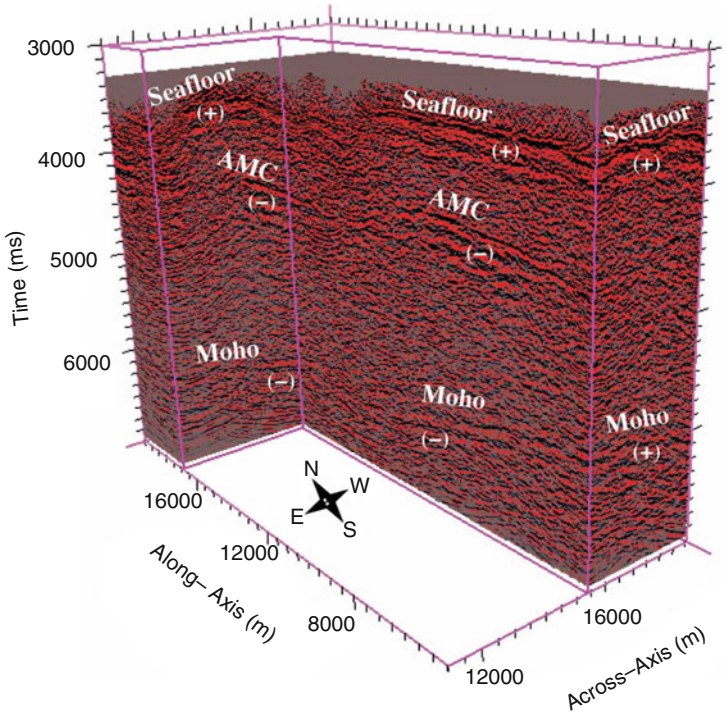

Crustal Reflectivity (Oceanic) and Magma Chamber, Figure 14 Seismic reflection image of Moho beneath the melt lens at the 9° N East Pacific Rise (Position 2 in Figure 2).

trench (Grevemeyer et al., 2007) and in the area of IODP Hole 1256 (Hallenborg et al., 2003) for crusts formed at the EPR about 20 Ma. Rodger et al. (2006) found an ultrathin crust (4 km) that was formed near the central MAR about 85 Ma ago, which they associate to be due to a reduction in the spreading rate from slow to ultraslow. The crustal study at ODP holes 504B also found thin crust (5 km), which Collins et al. (1989) associate to be due to depleted mantle. Singh et al. (2011) have observed ultrathin crust (3.5–4.5 km) in the Indian Ocean (Figure 15) that was formed at fast spreading Wharton center 55 Ma ago, which they associate to be due to the interaction of the Kerguelen plume with the Wharton Spreading center due to channeling of the cold lithosphere around a plume and its interaction with the spreading center.

Upper mantle

The velocity in the upper mantle is generally determined using rays that turn below the Moho, which are called Pn arrivals. The velocity in the mantle beneath ridge axis is ~7.6–7.8 km/s and is 8–8.1 km/s away from the ridge axis (Vera et al., 1990; Harding et al., 1989). An extensive 3D tomography and undershoot experiment were carried out at 9° N EPR. Using these data, Dunn et al. (2000, 2001) obtained a symmetric low velocity anomaly below the Moho in the mantle. Using the same data and some new data Toomey et al. (2007) found asymmetric low velocity anomaly at 10 km away from the ridge axis. There are serious problems with these results. First, the crustal thickness in this area varies from 6 to 8 km. Secondly, the velocity anomaly depends on the background velocity used during the inversion. Dunn et al. (2000) use a starting mantle velocity of 8.2 km/s whereas one year later Dunn et al. (2001) use 7.6 km/s. Although the crustal thickness is up to 8 km (Canales et al., 2003), Dunn et al. (2001) interpret velocity at 7 km below the seafloor; the part of the anomaly could be due to crustal variations. Toomey et al. (2007) show that the ray only penetrates down to 8 km below the seafloor but interpret the velocity at 9 km below the seafloor. These conflicting results and the inaccuracy in inversion led Singh and Macdonald (2009) to suggest that these results are not reliable. The only robust solution we have is that the velocity in the mantle is ~7.6–7.8 km/s below the ridge axis and 8–8.1 km/s away from the ridge axis (Vera et al., 1990; Harding et al., 1989). However, it is possible that melt sills get trapped in the mantle as shown by Nedimovic et al. (2005) and may lead to a low velocity anomaly in the mantle.

Faults in the oceanic crust and upper mantle

Along with magmatic process, tectonic processes also play an important role in shaping the oceanic crust. Singh et al. (2006b) have shown that median valley bounding faults could be imaged down to 3 km, close to the melt lens. They also found extensive faults above the melt lens. It is possible that some of these faults penetrate down to the crust–mantle boundary (Dusunur et al., 2009).

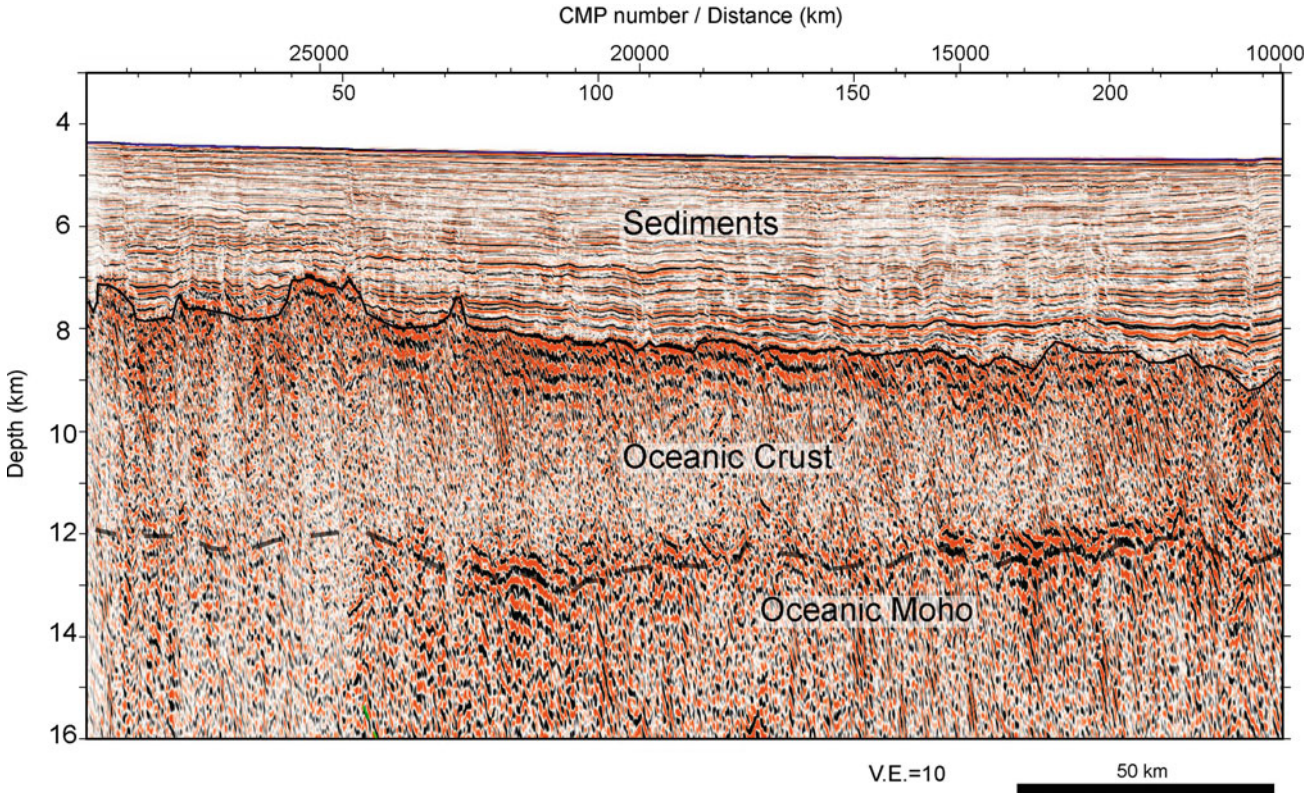

Crustal Reflectivity (Oceanic) and Magma Chamber, Figure 15 Seismic reflection image of extremely thin crust in the Indian Ocean (Position 4 in Figure 2) (modified from Singh et al., 2011).

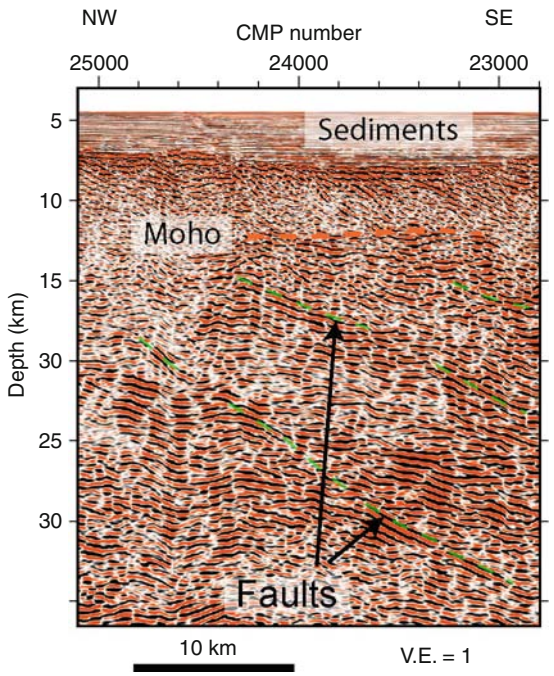

Crustal Reflectivity (Oceanic) and Magma Chamber, Figure 16 Seismic reflection of deep penetrating faults in the mantle in the Indian Ocean (Position 4 in Figure 2).

In a subduction zone environment, there are two forces that act on the incoming oceanic plate: plate bending leading to normal faulting and compressive forces leading to thrust faulting. Water can enter into the mantle leading to serpentinization of the oceanic mantle. Normal faulting down to 5–8 km below the Moho, related to bending of the subducting plate and the associated serpentinization, has been reported for the Central American trench (Ranero et al., 2003). Faults have also been imaged in the mantle offshore Sumatra down to 35 km depths (Figure 16) suggesting that a significant part of the oceanic lithosphere is involved during oceanic earthquakes.

Summary

The reflectivity of the oceanic crust and axial magma chambers at ocean spreading centers are described in detail using real seismic images. The oceanic crust consists of three distinct layers: Layer A is 200–1,000 m thick and consists mainly of pillow lavas. Layer B is 1–2 km thick and consists mainly of cooled basalts in dikes. Layer 3 is 2–3 km thick and is formed by the cooling and crystallization of magma in the melt lens. Axial melt lens has been imaged on fast and intermediate spreading centers and recently on a slow spreading center (Singh et al., 2006b). Melt lenses are 50–60 m and have a roof and a floor. Between the melt and Moho, lower crust,

partial melt is generally present. The oceanic crust is about 6 km thick, which could vary from 3.5 to 8 km. The P-wave velocity in the mantle lie between 7.6 and 8.1 km/s, but the detailed nature of the oceanic mantle is poorly constrained and requires further investigations. Faults due to earthquakes have been observed down to 35 km depth.

Bibliography

Barclay, A. H., Toomey, D. R., and Solomon, S. C., 1998. Seismic structure and crustal magmatism at the Mid-Atlantic Ridge, 35° N. *Journal of Geophysical Research*, **103**, 17827–17844.

Barth, G. A., and Mutter, J. C., 1996. Variability in oceanic crustal thickness and structure: multichannel seismic reflection results from the northern East Pacific Rise. *Journal of Geophysical Research*, **101**, 17951–17975.

Bazin, S., Harding, A. J., Kent, G. M., Orcutt, J. A., Singh, S. C., Tong, C. H., Pye, J. W., Barton, P. J., Sinha, M. C., White, R. S., Hobbs, R. W., and van Avendonk, H. J. A., 2003. A three-dimensional study of axial low velocity beneath the 9° 03′ N overlapping spreading center. *Geophysical Research Letters*, **30**, 1–4.

Boudier, F., Nicolas, A., and Ildefonse, B., 1996. Magma chambers in the Oman ophiolite: fed from the top and the bottom. *Earth and Planetary Science Letters*, **144**, 238–250.

Canales, J.-P., Detrick, R. S., Toomey, D. R., and Wilcock, W. S. D., 2003. Segment-scale variations in the crustal structure of 150–300 kyr old fast spreading oceanic crust (East Pacific Rise, 8° 15′ N–10° 5′ N) from wide-angle seismic refraction profiles. *Geophysical Journal International*, **152**, 766–794.

Canales, J.-P., Singh, S. C., Detrick, R. S., Carbotte, S. M., Harding, A. J., Kent, G. M., Diebold, J. B., Babcock, J., and Nedimovic, M. R., 2006. Seismic evidence for variations in axial magma chamber properties along the southern Juan de Fuca Ridge. *Earth and Planetary Science Letters*, **246**, 353–366.

Canales, J. P., Nedimovic, M. R., Kent, G. M., Carbotte, S. M., and Detrick, R. S., 2009. Seismic reflection images of a lear-axis melt sill within the lower crust at the Juan de Fuca Ridge. *Nature*, **460**, 89–94.

Carton, H. D., Carbotte, S. M., Mutter, J. C., Canales, J., Nedimovic, M. R., Marjanovic, M., Aghaei, O., Xu, M., Han, S., Stowe, L., 2009. Characteristics of the crustal magma body in the 2005–2006 eruption area at 9° 50′ N on the East Pacific Rise from 3D multi-channel seismic data. *AGU*, Fall meeting, Abstract OS11B-02.

Charvis, P., Laesanpura, A., Gallart, J., Hirn, A., Lepine, J., de Voogd, B., Minshull, T. A., Hello, Y., and Pontoise, B., 1999. Spatial distribution of hotspot material added to the lithosphere under La Reunion, from wide-angle seismic data. *Journal of Geophysical Research*, **104**, 2875–2893.

Christeson, G., McIntosh, K., and Karson, J., 2007. Inconsistency in correlation of layer 2A and lava layer thickness in oceanic crust. *Nature*, **445**, 418–421.

Collier, J. S., and Singh, S. C., 1997. Detailed structure of the top of the melt body beneath the East Pacific Rise at 9°40′ N from waveform inversion of seismic reflection data. *Journal of Geophysical Research*, **102**, 20287–20304.

Collier, J. S., and Sinha, M., 1990. Seismic images of a magma chamber beneath the Lau Basin back-arc spreading centre. *Nature*, **346**, 646–648.

Collins, J. A., Purdy, G. M., and Brocher, T. M., 1989. Seismic velocity structure at Deep Sea Drilling Site 504B, Panama Basin: evidence for thin oceanic crust. *Journal of Geophysical Research*, **94**, 9283–9302.

Detrick, R. S., Buhl, P., Vera, E., Mutter, J., Orcutt, J., Madsen, J., and Brocher, T., 1987. Multi-channel seismic imaging of a crustal magma chamber along the East Pacific Rise. *Nature*, **326**, 35–41.

Detrick, R. S., White, R. S., and Purdy, G. M., 1993. Crustal structure of North Atlantic Fracture Zone. *Reviews of Geophysics*, **31**, 439–458.

Dunn, R. A., Toomey, D. R., and Solomon, S. C., 2000. Three-dimensional seismic structure and physical properties of the crust and shallow mantle beneath the East Pacific Rise 9° 30′ N. *Journal of Geophysical Research*, **105**, 23537–23555.

Dunn, R. A., Toomey, D. R., Detrick, R. S., and Wilcock, W. S. D., 2001. Continuous mantle melt supply beneath an overlapping spreading centre on the East Pacific Rise. *Science*, **291**, 1955–1958.

Dusunur, D., Seher, T., Combier, V., Escartin, J., Crawford, W., Cannat, M., Singh, S. C., Matias, L. M., and Miranda, J. M., 2009. Seismological constraints on the thermal structure and interaction of tectonic and magmatic processes around the Lucky Strike magma chamber, slow spreading Mid-Atlantic Ridge. *Marine Geophysical Research*, **30**, 105–120.

Eittreim, S. L., Gnibidenko, H., Helsley, C. E., Sliter, R., Mann, D., and Ragozin, N., 1994. Oceanic crustal thickness and seismic character along a central Pacific transect. *Journal of Geophysical Research*, **99**, 3139–3145.

Grevemeyer, I., Flueh, E. R., Reichert, C., Bialas, J., Klaschen, D., and Kopp, C., 2001. Crustal architecture and deep structure of the Ninetyeast Ridge hotspot trail from active-source ocean bottom seismology. *Geophysical Journal International*, **144**, 414–431.

Grevemeyer, I., Ranero, C. R., Flueh, E. R., Klaschen, D., and Bialas, J., 2007. Passive and active seismological study of bending-related faulting and mantle serpentinisation at the Middle American trench. *Earth and Planetary Science Letters*, **258**, 528–542.

Hallenborg, E., Harding, A. J., and Kent, G. M., 2003. Seismic structure of 15 Ma oceanic crust formed at an ultra-fast spreading East Pacific Rise: evidence for kilometer-scale fracturing from dipping reflectors. *Journal of Geophysical Research*, **108**, 2532, doi:10.1029/2003JB002400.

Harding, A. J., Kappus, M. E., Orcutt, J. A., Vera, E. E., Buhl, P., Mutter, J. C., Detrick, R., and Brocher, T., 1989. The structure of young oceanic crust 13° N on the East Pacific Rise from expanding spread profiles. *Journal of Geophysical Research*, **94**, 12163–12196.

Harding, A. J., Kent, G. M., and Orcutt, A. J., 1993. A multichannel seismic investigation of upper crustal structure at 9° N on the East Pacific Rise: implications for crustal accretion. *Journal of Geophysical Research*, **98**, 13925–13944.

Jokat, W., and Schmidt-Aursch, M. C., 2007. Geophysical characteristics of the ultra-slow spreading Gakkel Ridge, Arctic Ocean. *Geophysical Journal International*, **168**, 983–998.

Kelemen, P. B., Koga, K., and Shimizu, N., 1997. Geochemistry of gabbro sills in the crust-mantle transition zone of the Oman ophiolite: implications for the origin of the oceanic lower crust. *Earth and Planetary Science Letters*, **146**, 475–488.

Kent, G. M., Harding, A. J., and Orcutt, J. A., 1993. Distribution of magma beneath the East Pacific Rise between the Clipperton Transform and the 9° 17′ N Deval from forward modelling of common depth point data. *Journal of Geophysical Research*, **98**, 13945–13969.

Kent, G. M., Harding, A. J., Orcutt, J. A., Detrick, R. S., Mutter, J. C., and Buhl, P., 1994. Uniform accretion of oceanic crust south of the Garrett transform at 14° 15′ S on the East Pacific Rise. *Journal of Geophysical Research*, **99**, 9097–9116.

Kent, G. M., Singh, S. C., Harding, A. J., Sinha, M. C., Tong, V., Barton, P. J., Hobbs, R., White, R., Bazin, S., and Pye, J.,

2000. Evidence from three-dimensional reflectivity images for enhanced melt supply beneath mid-ocean-ridge discontinuities. *Nature*, **406**, 614–618.
Nedimovic, M. R., Carbotte, S. M., Harding, A. J., Detrick, R. S., Canales, J. P., Diebold, J. B., Kent, G. M., Tischer, M., and Babcock, J. M., 2005. Frozen magma lenses below the oceanic crust. *Nature*, **436**, 1149–1152.
Parkin, C. J., and White, R. S., 2008. Influence of the Iceland mantle plume on the oceanic crustal generation in the North Atlantic. *Geophysical Journal International*, **173**, 168–188.
Ranero, C. R., Reston, T. J., Belykh, I., and Gnibidenko, H., 1997. Reflective oceanic crust formed at a fast spreading centre in the Pacific. *Geology*, **25**, 499–502.
Ranero, C. R., Phipps Morgan, J., McIntosh, K., and Reichert, C., 2003. Bending-related faulting and mantle serpentinization at the Middle America trench. *Nature*, **425**, 367–373.
Rodger, M., Watts, A. B., Greenroyd, C. J., Peirce, C., and Hobbs, R. W., 2006. Evidence for unusually thin oceanic crust and strong mantle beneath the Amazon Fan. *Geology*, **34**, 1081–1084.
Seher, T., Crawford, W., Singh, S. C., and Cannat, M., 2010a. Seismic layer 2A variations in the Lucky Strike segment at the Mid-Atlantic Ridge from reflection measurements. *Journal of Geophysical Research*, **115**, B07107, doi:10.1029/2009JB006783.
Seher, T., Singh, S. C., Crawford, W., and Escartin, J., 2010b. Upper crustal velocity structure beneath the central Lucky Strike Segment from seismic refraction measurements. *Geochemistry, Geophysics, Geosystems*, **11**, 5, doi:10.1029/2009GC002894.
Seher, T., Crawford, W., Singh, S. C., Cannat, M., Combier, V., Dusunur, D., and Canales, J.-P., 2010c. Crustal velocity structure of the Lucky Strike segment of the Mid-Atlantic Ridge (37°N) from seismic refraction measurements. *Journal of Geophysical Research*, **115**, B03103, doi:10.1029/2009JB006650.
Singh, S. C., and Macdonald, K., 2009. Mantle skewness and ridge segmentation. *Nature*, **458**, E11–E12.
Singh, S. C., Midenet, S., and Djajadihardja, Y., 2009. Sesimic evidence of the locked and unlocked Sumatra subdction zone. EOS, **90**, 471–472.
Singh, S. C., Kent, G. M., Collier, J. S., Harding, A. J., and Orcutt, J. A., 1998. Melt to mush variations in crustal magma properties along the ridge crest at the southern East Pacific Rise. *Nature*, **394**, 874–878.
Singh, S. C., Collier, J. S., Kent, G. M. J. S., Harding, A. J., and Orcutt, J. A., 1999. Seismic evidence for a hydrothermal layer above the solid roof of axial magma chamber at the southern East Pacific Rise. *Geology*, **27**, 219–222.
Singh, S. C., Harding, A., Kent, G., Sinha, M. C., Combier, V., Hobbs, R., Barton, P., White, R., Tong, V., Pye, J., and Orcutt, J. A., 2006a. Seismic reflection images of Moho underlying melt sills at the East Pacific Rise. *Nature*, **442**, 287–290.
Singh, S. C., Crawford, W., Carton, H., Seher, T., Combier, V., Cannat, M., Canales, J., Dusunur, D., Escartin, J., and Miranda, M., 2006b. Discovery of a magma chamber and faults beneath a hydrothermal field at the Mid-Atlantic Ridge. *Nature*, **442**, 1029–1033.
Singh, S. C., Carton, H., Chauhan, A., et al., 2011. Extremely thin crust in the Indian Ocean possibly resulting from Plume-Ridge interaction. *Geophysical Journal International*, doi:10.1111/j.1365-246X.2010.04823.x.
Taylor, M., and Singh, S. C., 2002. Composition and microstructure of magma bodies from effective medium theory. *Geophysical Journal International*, **149**, 15–21.
Toomey, D. R., Purdy, G. M., Solomon, S. C., and Wilcock, W. S. D., 1990. The three-dimensional seismic velocity structure of the East Pacific Rise near latitude 9°30′ N. *Nature*, **347**, 639–645.
Toomey, D. R., Jousselin, D., Dunn, R. A., Wilcock, W. S. D., and Detrick, R. S., 2007. Skew of mantle upwelling beneath the East Pacific Rise governs segmentation. *Nature*, **446**, 409–414.
Van Avendonk, H. J. A., Harding, A. J., Orcutt, J. A., and McClain, J. S., 2001. Contrast in crustal structure across the Clipperton transform fault from travel time tomography. *Journal of Geophysical Research*, **106**, 10961–10981.
Vera, E. E., Mutter, J. C., Buhl, P., Orcutt, J. A., Harding, A. J., Kappus, M. E., Detrick, R. S., and Brocher, T. M., 1990. The structure of 0 to 0.2 m.y. old oceanic crust at 9° N on the East Pacific Rise from expanding spread profiles. *Journal of Geophysical Research*, **95**, 15529–15556.
Watts, A. B., ten Brink, U. S., Buhl, P., and Brocher, T. M., 1985. A multi-channel seismic study of lithospheric flexure across the Hawaiian Emperor seamount chain. *Nature*, **315**, 105–111.
White, R. S., McKenzie, D., and O'Nions, R. K., 1992. Oceanic crustal thickness from seismic measurements and rare earth element inversions. *Journal of Geophysical Research*, **97**, 19683–19715.

Cross-references

Deep Seismic Reflection and Refraction Profiling
Earth's Structure, Continental Crust
Lithosphere, Oceanic
Ocean Bottom Seismics
Ocean, Spreading Centre
Seismic Data Acquisition and Processing
Seismic Structure at Mid-Ocean Ridges
Single and Multichannel Seismics

CURIE TEMPERATURE

Vincenzo Pasquale
Dipartimento per lo Studio del Territorio e delle sue Risorse, Settore di Geofisica, Università degli Studi di Genova, Genova, Italy

Synonyms

Curie point

The critical temperature above which any material loses its permanent magnetism.

A rock containing magnetic minerals loses its permanent magnetism when heated up to reach a critical temperature. This is the Curie temperature or Curie point, ϑ_c, above which the rock is paramagnetic. On the atomic level, below ϑ_c, the magnetic moments are aligned in their respective domains and even a weak external field results in a net magnetization. As the temperature increases to ϑ_c and above, however, fluctuations due to the increase in thermal energy destroy that alignment.

Strongly magnetic minerals are all of ferrimagnetic type, in which neighboring magnetic moments are aligned antiparallel, as in antiferromagnetism, but unequal numbers or strengths give a net magnetization. Among them, magnetite, one of the members of the titanomagnetite solid-solution series, is the most important magnetic mineral to geophysical studies of crustal rocks (Stacey, 1992). There are many other magnetic minerals, but they are rare

(iron sulfide), unstable (maghemite) or having a weak spontaneous magnetization due to the canting of its nearly equal and opposite atomic moments (canted antiferromagnetism), as hematite occurring in sedimentary rocks often in solid solution with ilmenite.

Variation of Curie temperature of titanomagnetite, $Fe_{3-x}Ti_xO_4$, is approximately given by $\vartheta_c = 580\,(1-1.26\,x)$, where magnetite (with chemical composition $x = 0$) and ulvöspinel ($x = 1$) are end members. In pure magnetite, ϑ_c is 580°C, but titaniferous inclusions can reduce ϑ_c, which approximates room temperature for $x = 0.77$ (Hunt et al., 1995). Saturation magnetization is thus a function of temperature, and it disappears above ϑ_c; at room temperature it decreases from 92 A m^2 kg^{-1} for $x = 0$ to about zero for $x = 0.8$. ϑ_c increases with pressure, but the change is quite small. At the crust–mantle boundary, it should not be more than a few degrees of the experimental values at normal pressure.

The crustal rocks lose their magnetization when they are at a depth where the temperature is greater than ϑ_c and their ability to generate detectable magnetic anomalies disappears. A comparison of the crustal temperature with ϑ_c may give information on the depth of compositional change where magnetic rocks are replaced with nonmagnetic material. Transforming regional magnetic anomalies data sets into the Fourier domain and analyzing their spectra allow to obtain information about deep magnetic discontinuities (Blakely, 1996). An example of deep magnetic discontinuities and their relation with Moho depth, temperature, and surface heat flux in central and southern Europe is given by Chiozzi et al. (2005) (Table 1).

The depth of the magnetic layer bottom corresponds to the Moho in the Variscan units and the expected temperature is close to ϑ_c of magnetite. Beneath the Alpine units, this depth is within the crust and its average temperature of 550°C indicates the presence of Ti content. In the Ligurian basin and the Tuscany-Latium geothermal area, the deep magnetic discontinuity sometimes lies a few kilometers below the Moho. This may indicate that the uppermost mantle also contributes to the geomagnetic field. The observed maximum temperature of 650°C, decidedly larger than ϑ_c of magnetite, is due to the fact that the local thermal anomalies are not discernible by the spectral analysis, which is a kind of low-pass filter depending on the window size of the magnetic data investigated.

Curie Temperature, Table 1 Crustal magnetic discontinuities with corresponding parameters

Area	Magnetic layer bottom depth (km)	Moho depth (km)	Temperature at magnetic layer bottom (°C)	Surface heat flux (mW m^{-2})
Variscan units (central Europe, Corsica–Sardinia block)	29–33	29–33	540–580	60–70
Alpine units (Alps, Apennines, Molasse and Po basins)	22–28	25–50	500–600	50–80
Ligurian basin, Tuscany–Latium geothermal area	17–28	17–20	500–650	80–120

Bibliography

Blakely, R. J., 1996. *Potential Theory in Gravity and Magnetic Applications*. Cambridge: Cambridge University Press.

Chiozzi, P., Matsushima, J., Okubo, Y., Pasquale, V., and Verdoya, M., 2005. Curie-point depth from spectral analysis of magnetic data in central-southern Europe. *Physics of the Earth and Planetary Interiors*, **152**, 267–276.

Hunt, C. P., Moskowitz, B. M., and Banerjee, S. K., 1995. Magnetic properties of rocks and minerals. In Ahens, T. J. (ed.), *Rock Physics and Phase Relations: A Handbook of Physical Constants*. Washington: American Geophysical Union, pp. 189–204.

Stacey, F. D., 1992. *Physics of the Earth*. Brisbane: Brookfield Press.

Cross-references

Earth's Structure, Continental Crust
Geomagnetic Field, Global Pattern
Geomagnetic Field, Theory
Heat Flow, Continental
Magnetic Domains
Remanent Magnetism

http://www.springer.com/978-90-481-8701-0

Encyclopedia of Solid Earth Geophysics
NGRI, D. (Ed.)
2011, LXXIV, 1539 p. In 2 volumes, not available separately., Hardcover
ISBN: 978-90-481-8701-0